STEREO DIGITAL PARTICLE IMAGE VELOCIMETRY INVESTIGATION OF A FREE SURFACE MIXING LAYER

Thesis by

Bradley S. Dooley

In Partial Fulfillment of the Requirements

for the Degree of

Doctor of Philosophy

California Institute of Technology

Pasadena, California

2005

(Defended May 26, 2005)

This work is dedicated to my wife, April. Her support, patience and humor during its long-awaited completion have made more of a difference than even she realizes.

Acknowledgements

I must extend my deepest gratitude to my thesis adviser, Dr. Mory Gharib, for a level of support far exceeding what I often felt I really deserved. I am humbled and inspired.

I must also thank Professors Ingersoll, Pullin, Ravichandran, and Shepherd, who in addition to Professor Gharib served as my thesis committee. Their input and great flexibility on a tight time schedule were invaluable.

The work presented in this thesis was generously supported by the Office of Naval Research under contract number N00014-98-1-0017, and I gratefully acknowledge their assistance.

The list of colleagues with whom I have had the chance to work and, in some cases, live during my time at Caltech has grown very long due to my somewhat extended stay; in this limited space I can only hope to do them all justice.

Amy Warncke Lang, Doug Shiels, and Ryan Mackey have been splendid lab partners, housemates, and friends.

Han Park has been a cheery companion and an invaluable resource for help in matters ranging from MATLAB programming to Stereo DPIV dewarping.

Patrice Maheo showed me by example how to get the most out of the Free Surface Shear Layer tunnel, and was enjoyable to work alongside.

Dana Dabiri has provided valuable expertise on all things PIV, and is usually good for a laugh, as well.

While not directly related to my work, Bill Bing deserves special mention for his tireless running of the Caltech-Occidental Concert Band, which gave me more of a musical outlet over the years than I had ever expected to find when I signed on here.

I'm quite grateful to Darius Modarress for giving me the opportunity to branch out into surface profilometry work, and for being so supportive in the process. In that same vein, Pavel Svitek has been perpetually helpful and approachable.

My Comrades-in-HALCIT, David Jeon and Michael OL, both deserve far more credit than I think they might realize for my enjoyment of my time as a grad student. Both have been inspirational, in their own very peculiar ways, both professionally and personally. Whether it was driving a big-block engine through the desert, searching greater LA for "buffeterias", or making sure the triangulation routine for SDPIV is really working right after all, these esteemed gentlemen have been and remain defining features of my time at Caltech.

John and Kathy Coyne, my wife's parents, have welcomed me into their extended family and provide a marvelous environment away from Caltech which I treasure.

A final proclamation of profound thanks must go out to my parents, Larry and Lana Dooley. I'm lost for words when trying to express the magnitude of their love and support.

Abstract

Shear flows in the vicinity of a free surface are a problem with numerous applications, perhaps the most obvious being the wakes of seagoing surface vessels. The flow behind a full-scale ship is extremely complex – so much so that it is frequently more instructive to consider simpler cases highlighting particular elements of the larger problem. To that end, an experimental investigation has been conducted to study the behavior of a turbulent plane mixing layer intersecting a free surface at low Froude number. The local Reynolds number, based on the velocity differential across the layer and the momentum thickness, was approximately 10,000.

The technique of Stereoscopic Digital Particle Image Velocimetry (SDPIV) was implemented to obtain instantaneous three-component velocity measurements within planar slices of the steady-state, spatially developing mixing layer flow. Guided by previous studies of the same flow conditions, specific depths were chosen at a single downstream station for investigation – specifically those in and around counter-rotating streamwise vortices known to exist in the mean flow very near the free surface. 3,000 consecutive SDPIV image pairs were recorded at a rate of 15 per second at each location, giving ample data for Reynolds decomposition and spectral analysis of the velocity fields.

The present study has found that the anisotropy known to exist in some other free surface flows, such as surface-parallel submerged jets, is also present in the case of the mixing layer. Power spectra of all three velocity components are shown to capture part of the inertial subrange; the isotropic energy cascade seen to be present away from the

free surface is also seen to disappear near the surface, as surface-normal velocity fluctuations are severely attenuated.

Additionally, a low-frequency spanwise oscillation is deduced from the velocity power spectra and cospectra in the immediate vicinity of the mean streamwise vortices. Not present at all at significant depth, the motions at this frequency are also observed to markedly decrease – in all components – at locations closer to the surface. These observations appear to have both parallels and key differences compared to previously observed meandering of model boat wakes, and the possibility that the oscillation stems from the vortex-pair instability is discussed.

Table of Contents

Table of Figures

Chapter 1 Introduction

1.01 Introduction

(a) Surface Ship Wakes

The wakes produced by sea-going surface vessels as they move across the ocean continue to be the subject of considerable attention for a number of reasons. Among them is the issue of observability. Relatively recent advances in remote sensing such as synthetic aperture radar (SAR) have made it possible to detect surface disturbances as long as several hours after a vessel's passage (Vesecky & Stewart, 1982; Shemdin, 1987; Milgram, 1988; Reed *et al.*, 1990; Ochadlick *et al.*, 1992). Visual observations have also been made, most notably by astronauts aboard the space shuttle (Scully-Power, 1986; Munk *et al.*, 1987), which noted similarly persistent but qualitatively different aspects of the wake.

Measurements by Peltzer *et al.* (1992) of surface tension profiles across ship wakes demonstrated that a central band of high surface tension (clean water) persisted, bordered by narrow bands of very low surface tension (high surfactant concentration). This alteration of the undisturbed surfactant concentration profile was shown to persist for considerable durations (hours), and to grow linearly with time/distance from the passed ship. The bands of high surfactant concentration damped out short-wavelength surface waves within them, which made these bands visible to both the naked eye and SAR. This phenomenon is of obvious military interest, and any systematic attempt to either make use of or defeat such observation techniques must begin with an understanding of the physics involved.

(b) Dealing with Ship Wake Complexity

Attempts to study ship wakes are presently hindered by a combination of the complexity of the flow and the relatively limited experimental techniques available. Reynolds numbers above 10^8 are common in full-scale wakes, and the actual flow is a complicated, high-Froude number process involving large surface waves, breaking waves, high concentrations of bubbles, and often unknown surface tension properties. A step-by-step approach has been adopted by much of the research community, as individual issues or simplified versions of wake flows highlighting particular aspects are studied.

A vortex pair approaching a boundary with either a no-slip (such as a wall) or free-slip (such as a free surface) has been extensively examined by a number of researchers. Sarpkaya & Henderson (1985) performed a seminal study on the topic, and subsequent work by Ohring & Lugt (1991), Willert (1992), and Dommermuth (1992) on vortex pairs significantly increased physical understanding of the problem. The work of Bernal & Kwon (1989) on the topic of vortex rings approaching a free surface proved illuminating, as well. In this study it was shown that a vortex ring nearing a free surface disconnects from itself, allowing the now free ends to attach to the free surface. Later work by Weigand & Gharib (1996) pointed out the mechanisms by which this takes place.

Turbulence in the absence of mean shear has been extensively examined near boundaries, as well. Hunt & Graham (1978) demonstrated that near a solid wall tangential velocity fluctuations are increased while a corresponding decrease is seen in surface-normal fluctuations. Brumley & Jirka (1987) and Walker, Leighton & Garza-

Rios (1996) obtained similar results in their respective experimental and numerical investigations.

Of flows involving the presence of mean shear, turbulent mixing layers have been studied in great detail for some time. Brown & Roshko (1974) identified the presence of coherent structures in the mixing layer and characterized their development. Winant & Browand (1974) investigate the pairing of these vortical structures downstream. Dimotakis & Brown (1976) expanded upon this work.

Mean shear flows near a free surface have recently gathered considerable attention. Swean *et al.* (1989), Liepmann (1990), and Anthony & Willmarth (1992) examined near-surface jets of various descriptions and all observed attenuation in vertical fluctuations near the surface. Anthony & Willmarth also observed an outward current at the free surface, away from the axis of a surface-parallel circular jet. Their conclusion was that this *surface current* consisted mainly of vortical structures which had been ejected from the jet flow. Interestingly, Walker & Johnson (1991) and Hoekstra (1991) had both observed similar surface currents in the wakes of model ships. Walker (1997) explained these surface currents in terms of Reynolds stress anisotropy.

Banerjee (1994) and Pan & Banerjee (1995) examined the behavior of turbulent upwellings impinging upon a free surface, again noting that a quasi-two-dimensional region exists in the immediate vicinity of the surface.

Logory *et al.* (1996) experimentally investigated a turbulent wake interacting with a free surface. Using laser Doppler anemometry they showed the presence of a shallow surface layer in which the wake's width roughly doubles, and confirmed the existence of surface-parallel structures using laser-induced fluorescence. These vortical structures, at

low Froude numbers, were explained in terms of their interaction with their images above the surface. These carried low-momentum fluid upwards and outwards near the surface, explaining the widening of the wake in that region.

Maheo (1998) used digital particle image velocimetry (DPIV) to examine a turbulent wake and a turbulent mixing layer, each as they interacted with a free surface. He found results much like those of Logory *et al.* in the wake case, and somewhat analogous behavior in the mixing layer. He used his downstream results to trace the origin of the surface layer in both cases back to the turbulent boundary layers along the splitter plate, with a Reynolds stress anisotropy driving the secondary flows.

Uijttewaal & Tukker (1998) and Uijttewaal & Booij (2000) used laser Doppler anemometry to examine a free surface mixing layer in shallow water, focusing on the region of nearly two-dimensional flow very close to the free surface and how it interacted with bottom turbulence.

Shen *et al.* (1999) numerically studied a mean shear flow in the presence of a free surface, and identified two separate near-surface layers of interest: the *surface layer*, where the dynamic requirement of zero tangential stress at the surface has influence; and the deeper-reaching *blocking layer*, where the kinematic requirement that surface-normal motion must vanish at the surface affects the flow. Shen *et al.* (2002) perform experimental and numerical studies on the wake of a towed ship model, observing and characterizing a meandering behavior in the wake flow.

1.02 Present Objectives

The objective of the present work is to build upon the work of Maheo (1998) by examining the same mixing layer studied in his work in a different fashion. The mean

flows have been characterized, but the goal of this experiment is to analyze the velocity fields in the frequency domain.

The technique of Stereo Digital Particle Image Velocimetry is utilized to simultaneously obtain all three components of velocity within a planar interrogation region. Thus, with a single setup all six components of the Reynolds stress tensor may be obtained, as well as turbulence kinetic energy.

Interrogations were performed across the mixing layer at its most developed station – *i.e.*, as far downstream as practicality permitted. Flow in the bulk region – out of the free surface influence – was measured as a baseline. Other depths were similarly examined, probing the region identified as the surface layer by Maheo, getting as near to the surface as experimental constraints allowed. A schematic of the flow and of the regions to be investigated is depicted in Figure 1.1.

Time histories of the velocity components were analyzed with two distinct regimes of investigation. First is the upper wavenumbers of the inertial subrange, where isotropy – or lack thereof – is pointed out in the decay of the turbulence. Second is the low frequency oscillations accompanying the fundamental instability of the mixing layer and possible oscillations in the surface currents described for this flow by Maheo. Interesting features in both cases were discovered, and these are discussed at some length following the exposition of the data.

1.03 Flow Selection

The flow selected for study in this set of experiments was a mixing layer with the same freestream speeds as those chosen by Maheo in his work: approximately 38 cm/s and 25 cm/s, respectively. These values were originally chosen to satisfy certain

conditions. First, it was necessary that the boundary layers on both sides of the splitter plate be turbulent; this effectively set a minimum for the low-speed side. For maximum turbulent energy, a large velocity difference between the freestreams, ΔU, was desired, so the high-speed freestream was chosen to be as high as the facility could support without flow quality issues. The particular downstream station to be studied, 1000 mm, was as far downstream of the splitter plate tip as the facility would support. This was chosen to give both as developed a flow as possible, and turbulence length scales as large as possible.

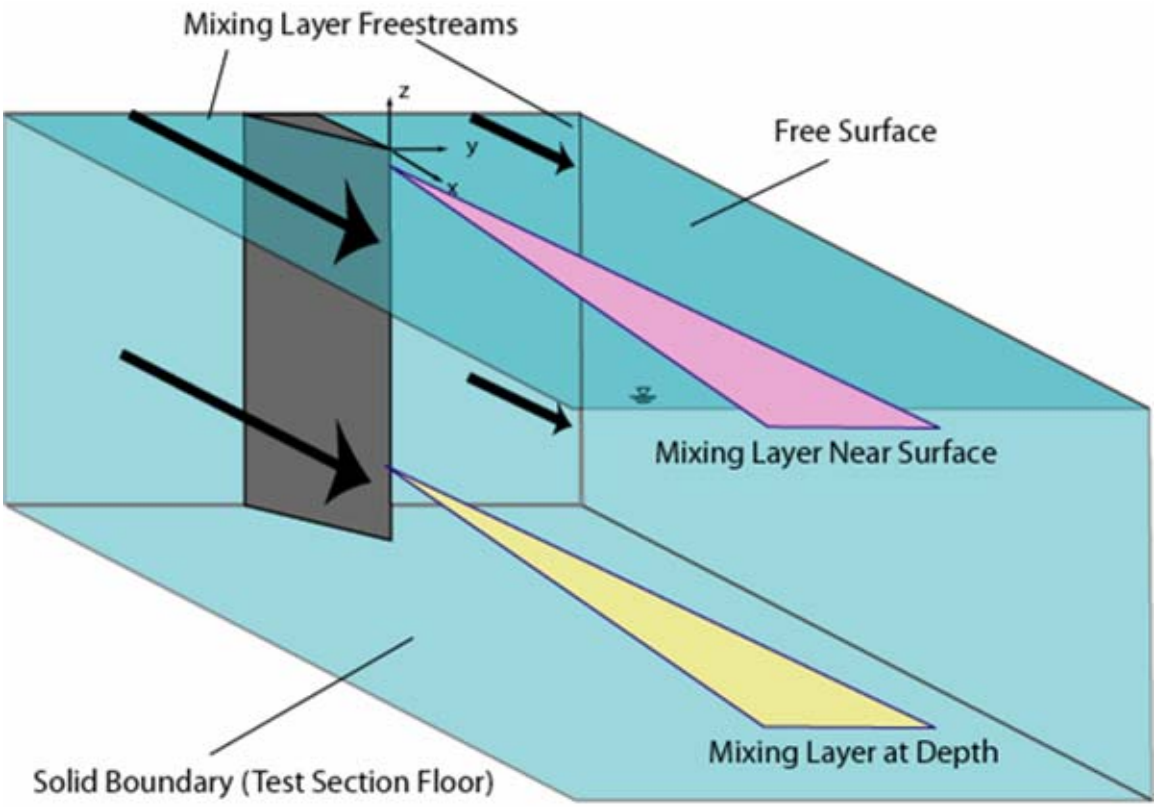

Figure 1.1: Schematic of mixing layer highlighting surface region and deep, or "bulk" region

Chapter 2 Experimental Methods

2.01 Facility

(a) Free Surface Shear Layer Facility

The experiments described in this work were performed in the Free Surface Shear Layer Facility located within the Graduate Aeronautical Laboratories, California Institute of Technology (GALCIT). Designed by M. Gharib of Caltech and constructed by Engineering Laboratory Design (Lake Forest, Minnesota), the tunnel was installed in the laboratory in 1993. A schematic of the facility, showing top and side views, is shown in Figure 2.1. Figure 2.2 depicts a schematic of the tunnel's test section along with elements of the experimental apparatus.

This recirculating water tunnel is characterized by two parallel and independently-controllable streams, separated upstream of the test section by a polyvinyl chloride (PVC) wall. The two 20 hp centrifugal pumps on each side are located below ground level to forestall cavitation by raising the hydrostatic pressure at the blades. Flow from the pumps enters the tunnel proper from below, exiting a perforated PVC tube to enter each side's respective diffuser section. The flow then passes through several flow-straightening devices (one perforated plate, one honeycomb/screen combined element, and two screens) before entering a three-dimensional 6:1 contraction section.

Upon leaving the contraction section the flow enters the Plexiglas test section of the tunnel, which begins at the terminus of the permanent splitter wall. The test section, like the entire length of the tunnel, has an open top and is 2 m long, 1 m wide, and supports a maximum water depth of 0.56 m. The bottom of the test section is 1.2 m

above the laboratory floor, allowing good optical access from below as well as from either side.

The dump tank section downstream of the test section contains turning vanes to deflect the flow to either side, where it passes downward through custom-installed vanes and honeycomb to the return tubes. The vanes and honeycomb were installed to prevent the formation of large vortices which were shown, in the devices' absence, to entrain large amounts of air and produce bubble-laden flow downstream of the pumps. The downstream end of the dump tank contains a Plexiglas window which permits optical access from directly downstream of the test section.

Variable-speed controllers could be used to set each side's flow rate anywhere between 2 and 20 m^3/min. With the test section filled (as it was for these experiments), the maximum practical speed of the tunnel was approximately 50 cm/s.

The tunnel facility is in essentially the same state as it was during the experiments performed there by Maheo (1998), with the exception of a section of honeycomb installed at the upstream end of the dump tank. These were installed to attenuate a long-period (~ 5 s) sloshing mode, corresponding to U-tube oscillations in the tunnel, discovered to exist within the tunnel when operated in certain speed combinations. This new honeycomb obstructed optical access from the downstream Lucite window, but as this window was not used during the present experiments the tradeoff was judged worthwhile.

(b) Splitter Plate

The design of the permanent dividing wall separating the two streams upstream of the test section was made flexible, to allow the fitting of a range of devices to its end. For the experiments described here, a PVC wedge was affixed to this end with stainless

steel screws to permit extended immersion in water. Of uniform cross-section from the test section floor to the top of the test section, this splitter plate is shown in Figure 2.3. The linear taper from a width of 7.3 cm (matching that of the dividing wall) to 1 mm at the tip was done at a half-angle of 4.5^{o}; this value was sufficiently low to prevent separation at tunnel working speeds due to the adverse pressure gradient imposed, yet sufficiently high to promote boundary layer transition to turbulence.

(c) Tunnel Calibration

Calibration of the tunnel as performed after installation was described in Maheo (1998). As the present experiments were performed in the same facility and under the same conditions, they will be briefly summarized here.

Laser Doppler anemometry (LDA) measurements found that flow nonuniformity in width, depth, and downstream distance was no greater than 3%, 1%, and 2.5%, respectively. These measurements were made with the tunnel in "wake mode" – both sides running at the same speed (35 cm/s). Results of the present study, presented in a separate chapter, will reveal substantially larger variation of freestream speed with depth while the two sides are at substantially different speeds – variation which does not appear to be monotonic (as the original baseline curves are).

Hot-film measurements described in detail in Maheo (1998) demonstrate that the freestream turbulence level on both sides of the tunnel are very low – approximately 0.1% or less.

2.02 Particle Image Data Acquisition Techniques

(a) Introduction

Known generically as Particle Image Velocimetry (PIV), the technique of measuring fluid flow velocity by observing the motions of tracer particles has been in use for some time, and in increasingly sophisticated ways. The review work of Adrian (1991) is an excellent reference for the history and early development of the PIV technique and its applications. The implementation of the PIV technique in a digital fashion by Willert & Gharib (1991) provided a dramatic reduction in image processing time, but at a cost of spatial resolution. Willert & Gharib (1991) and Westerweel *et al.* (1991) demonstrate that measurement accuracy is not adversely affected by a switch to digital processing. Digital Particle Image Velocimetry (DPIV), as it has come to be commonly known, has thus found application in a number of situations in which the processing of large numbers of PIV images is beneficial or necessary. Maheo (1998) put the DPIV technique to use in characterizing free surface wakes and mixing layers in terms of Reynolds decomposition – mean and fluctuating velocity components – by processing thousands of consecutively-recorded particle images.

DPIV, as conventionally applied, makes use of a single camera and interrogates a thin sheet within the region of interest; while ideally infinitesimally thin, the plane of interrogation if of necessity finite in thickness. A primary limitation of this technique is that it yields velocity data only within the target plane; the velocity component normal to this plane is lost.

Stereo DPIV (SDPIV) is a relatively straightforward extension of (planar) DPIV, using two cameras rather than the usual one. While still interrogating a single plane in

space, the technique makes use of the known (different) positions of the two cameras to obtain all three velocity components through application of the principles governing stereoscopic vision. Recent applications of SDPIV were reported by Ol (2001) and Zuhal (2001). An excellent overview of the concept may be found in Raffel *et al.* (1998). Details of both planar DPIV and SDPIV will be provided in subsequent sections.

(b) Planar DPIV System

In a fashion typical of most PIV approaches, planar DPIV measurement is performed using a single camera (CCD devices often prove most suitable), and interrogates a thin "sheet" within the region of interest. The camera is typically positioned so that the optical axis is normal to the plane formed by the sheet. A schematic of the setup is depicted in Figure 2.4.

Illumination of the interrogation region is commonly provided by lasers; a circular beam of light passed through a cylindrical lens emerges as a fan-shaped sheet. Suitable lens selection and positioning enable the entire interrogation region to be illuminated with sufficient uniformity. Pulsed high-powered lasers such as Nd:YAG types are commonly used, but continuous lasers with external shutters may be used if conditions of the experiment permit. White light sources, with the output suitably directed, have been used in the past, as well (Park, 1998). Due to the added complexity, however, this is typically not done unless some peculiarity of the situation requires it.

Small, approximately-neutrally-buoyant tracer particles are seeded into the flow, and are illuminated by the light source as they pass through the interrogation volume. Scattered light from these particles is imaged by the camera, and successive pulses of the light source are recorded in consecutive images.

Cross-correlation of corresponding sub-windows in each pair of images is performed using a technique outlined in Willert and Gharib (1991); rather than matching individual particles between exposures, the overall light intensity patterns within each sub-window are compared for offset. The location of the peak value of the cross-correlation function for each window represents the measured displacement; sub-pixel accuracy is achieved through a Gaussian fit of the highest value with its nearest neighbors. This displacement is assigned to the center of its window, and the result of this process is a field of local displacement vectors, projected onto the nominal plane of the light sheet. By proper scaling for distance, and taking into account the time passage over which this displacement occurred, an instantaneous velocity field may be obtained.

(c) Stereoscopic DPIV System (SDPIV)

Stereoscopic DPIV is an extension of the DPIV system described above, so named due to its application of the principles of three-dimensional ("stereoscopic") vision to extract 3-D information using nominally 2-D equipment. It utilizes the same principles of tracer particle seeding and illumination. The key differences are in the number of cameras used, their positioning, and the velocity components which can be measured.

Two cameras, rather than one, are used to simultaneously image the interrogation region. These cameras are placed at known, distinct locations, and record scattered light from the tracer particles just as in DPIV. It is necessary to ensure that the cameras' operation is synchronized, but this is generally straightforward to achieve with an externally-generated timing signal provided to both cameras.

The three-dimensional velocity field in the target plane is observed by each camera. The apparent velocity field observed by each camera is computed independently, using the same process - in fact, the very same software, without modification - as in DPIV. However, the lack of sufficient information to do otherwise requires that the apparent velocity field observed by each camera be taken as entirely within the target plane. Out-of-plane components of the actual velocity field will result in differences between the two observed two-dimensional velocity fields: The geometry of the setup is used to reconcile these two different two-component fields ("triangulation") and reconstruct the three-component field. A diagram illustrating this idea is shown in Figure 2.5. The resulting information is a full three-dimensional velocity field, taken in a single plane.

One obvious concern which may not be ignored is the oblique view each camera takes of the target area. This results in two issues, each of which must be dealt with: (1) blur, caused by the target plane and lens focal plane being rotated relative to one another; and (2) perspective distortion, complicating the issue of "matching" corresponding vectors in the two cameras' 2-D velocity fields for triangulation. (If two triangulated vectors were not obtained from the same location in physical space, then the exercise will produce meaningless information.)

There are two popular methods of dealing with problem (1) above, each involving repositioning of the camera itself relative to the lens (Raffel *et al.*, 1998). One method is commonly referred to as the "shift" technique, in which the camera and lens remain aligned normal to the target plane but are translated by differing amounts parallel to the target plane without rotation. A drawback to this approach is that the final optical path

from the target to the camera CCD passes through the lens at quite an oblique angle – a condition for which the lens may not have been optimized.

The method selected here is the so-called “tilt” technique, in which the camera and the lens are rotated relative to one another. The center of the CCD remains on the principal axis of the lens. When the camera, lens, and target plane are aligned according to the “Scheimpflug criterion” – their normal planes coincide at some line in 3-space – the entire image on the CCD will be in clear focus. A schematic of this setup is shown in Figure 2.6.

Problem (2) is ensuring that corresponding vectors in each camera’s individual displacement field are measured at the same location in physical space; the solution chosen for the system used here requires some pre-processing of the images prior to the calculation of the displacement vectors. The “tilt” method of handling the focus issue causes inevitable perspective distortion when the viewing angle of the camera onto the target plane is appreciable – as it must be for good out-of-plane resolution.

The solution implemented here is identical to that used to Ol and Zuhal, namely *dewarping* of the data images prior to processing with DPIV. A square grid is placed in the target plane and the image recorded by both cameras; a “center” of the grid is suitably identified, often by the intersection of two diagonal lines. A “dewarping” routine (written by H. Park) is run on each image; this routine detects the intersection of the grid lines and obtains a twelve-degree-of-freedom polynomial mapping of that perspective-distorted grid onto the square, undistorted grid. Prior to processing, the camera-appropriate dewarping function is applied to each data image; the result of this is that corresponding pixels in the two modified images represent the same location in the

physical target plane. These dewarped images are processed, and the triangulation is then done as described above. Ol provides a detailed description of the dewarping implementation.

DPIV and SDPIV may in principle be performed simultaneously, using the same particles and light source. As will be described in later sections, this was done in the experiments discussed in this thesis.

2.03 DPIV and SDPIV as Applied

(a) Introduction

The cameras used for both stereo and planar DPIV data acquisition were PULNiX (Sunnyvale, California) model TM-9701's. Those used for the SDPIV were equipped with a remote head option for convenience in mounting on the apparatus used to achieve the Scheimpflug condition mentioned above. This model has a 640x480 pixel resolution, and may be toggled between interlaced and progressive scan modes: for this experiment, interlaced analog output was used.

A PC running Windows NT 4.0 served as the storage unit for the acquired data. Video output from the cameras was captured to the PC by a Coreco RGB-SE board (one camera per color channel) and recorded to a two-drive RAID-0 ("striped") disk array – necessary to sustain the data rate of nearly 30 MB/sec from the recording cameras. The operation of the framegrabber board was handled from the PC using the Video Savant 3.0 (IO Industries, London, Ontario, Canada) software package and an accompanying OEM-provided Software Development Kit demonstration program.

Framing of all three cameras was driven by a signal from an external master triggering device (Sigma Electronics CSG-4500). The video output from one of the cameras, in addition to being sent to the framegrabber board, was fed into a locally built digital delay generator. This unit sent a TTL trigger signal to the laser controllers. By this means, all three cameras and the light source were kept in precise synchronization.

(b) Concurrent Implementation of Stereo- and Planar DPIV

In order to directly compare the results of planar and stereo DPIV, both techniques were implemented simultaneously in all phases of this experiment. The (single) camera used for planar DPIV was mounted directly beneath the tunnel test section, while the (two) stereo cameras were positioned to either side. This planar DPIV camera was also a PULNiX TM-9701, without the remote head option. The cameras used for stereo DPIV were equipped with 105 mm Nikon lenses, while the planar DPIV camera beneath the tunnel used a Nikon lens with a focal length of 180 mm. This allowed the spatial resolution for each camera to be approximately the same.

Output images from each camera were 8-bit black-and-white. Since the cameras were driven by a common source and thus synchronized, it was possible to assign one camera to each of the three color channels fed to the RGB-SE framegrabber (planar: blue; stereo: red and green). The three images were saved as a single color image, and were separated in software prior to processing. A significant side benefit of this arrangement was that the planar DPIV camera was very useful in aligning target grids and obtaining length scales during setup and calibration.

For all experiments described herein, the overall configuration of the interrogation area and the two SDPIV cameras was in general as shown in Figure 2.7. Positional variations of specific items will be discussed in detail in the following paragraphs.

The laser light sheet was, in all cases, parallel to the free surface. The Gemini PIV laser unit (New Wave Research, Sunnyvale, California), consisting of two 30 mJ/pulse Nd:YAG laser heads and attached combining optics, provided more than adequate illumination. The Gemini unit, along with a series of lenses and mirrors used to create the laser sheet and to fine-adjust its position and thickness, was mounted on a multi-purpose adjustable stand as shown in Figure 2.8. This equipment was positioned directly to the side of the water tunnel, and the laser light sheet passed transversely through the Plexiglas side wall.

The combined laser beams first pass through the two spherical lenses shown in Figure 2.8; the first lens focused the beams, while the second expanded them. The net effect of the two lenses working as a unit was a narrowing of the beams. The resulting beam diameter (and thus eventual laser sheet thickness) could be adjusted by moving the two spherical lenses relative to one another; for the experiments described in this work, the laser sheet thickness was approximately 2 mm.

The laser sheet was created by passing the beams through a pair of cylindrical lenses, both oriented to expand the beam in the horizontal direction; these are the second two lenses from the right in Figure 2.8. Two lenses were used due to their availability at the time of the experiment; the net width of the laser sheet at the test section was found to be quite satisfactory with this pair of lenses - approximately 250 mm.

The apparatus visible on the far left of the platform shown in Figure 2.8 is a pair of mirrors. Their presence is for convenience, as fine adjustments to the laser sheet's height or angle relative to the horizontal could be made by manipulating these mirrors rather than the entire laser-optics platform.

The DPIV camera was mounted quite straightforwardly directly beneath the tunnel test section, oriented to face directly up through the Plexiglas floor. This camera was mounted on a large post to facilitate vertical movement, and on a transversely aligned sliding traverse to allow adjustment of position in the lateral direction. Rotation stages of various types enable the camera to be rotated about all three coordinate axes.

The two cameras used for the SDPIV measurements were positioned directly outside the test section walls, mounted on adjustable platforms. The overall setup of these cameras was similar to that used by Ol, primarily in the use of mirrors placed within the water tunnel itself, as was shown in the schematic of Figure 2.7.

Optical distortion caused by index of refraction differences between the various media involved necessitated that the optical axes of both cameras be normal to the test section walls. Consequently, it was necessary to install mirrors inside the tunnel to allow the cameras to properly image the target region. These mirrors were mounted on adjustable 1/2” diameter post units fixed above the surface of the water. Fine adjustments of the mirror positions and orientations were done by manipulating various rotating stages on the post mounting units suspended above the tunnel.

Care was taken to insure that the support posts, and the mirrors themselves, were sufficiently downstream and outboard of the regions of experimental interest. Tests were also performed to confirm that the mirrors and their mounting hardware did not move or

deflect under the hydrodynamic loads presented by the water while the tunnel was in operation; imaging of a rigidly fixed object at the target plane revealed that any errors caused by the vibration/deflection of the mirrors was well under 1 pixel – far too small to observe in the images themselves.

A mechanical system very similar to that used by Ol and Zuhal was implemented to remedy the problem of the SDPIV cameras imaging a plane not normal to the CCD plane. To achieve the Scheimpflug condition, as defined previously, it was necessary to rotate each camera relative to its lens. The aluminum mounting apparatus shown in Figure 2.9 allowed this rotation. In practice, the rotation of each camera was optimized visually for each case: A grid (the same one used for dewarping) was placed in the target plane, and the rotation of the cameras was adjusted until the entire grid image was uniformly in focus. This method of alignment proved quicker and more accurate than attempts to mathematically calculate and then achieve the required angle between the camera and lens axes.

(c) Particle Seeding

Seeding of the flow was done using Conduct-O-Fil brand silver-coated hollow glass spheres produced by Potters Industries (Carlstadt, New Jersey), with a mean diameter of 40 μm. The individual particles are estimated by the manufacturer to have a specific gravity of approximately 0.8.

The particles were mixed into the tunnel water and allowed to evenly distribute, which they did after only a few complete circulations of the running tunnel as evidenced by study of images recorded by the DPIV camera. Due to the manner in which the particles were introduced into the tunnel, their number density is not precisely known.

Rough estimates may be made, however: Based on the known laser sheet thickness and spatial scaling of the particle images captured during the experiments, the number density of the particles is estimated at approximately 5 particles per 8 mm^3. At 0.4/mm^3, this corresponds to a volume fraction of 1.34×10^{-5}. Elghobashi (1994) suggests that the effects of the tracer particles on the flow may be completely ignored for volume fractions less than 10^{-6}; it is seen that our estimated volume fraction is an order of magnitude greater than this.

The ability of tracer particles to actually follow the flow they are assumed to be representing is a function of their characteristic response time

$$\tau_p = \frac{\rho_p}{\rho_{\text{fluid}}} \frac{d_p^2}{18 \nu_{\text{fluid}}} = 70 \ \mu\text{s}.$$

As this is several orders of magnitude less than the Kolmogorov time scale of the flow studied here, estimated in Chapter 3 to be $O(10^{-1}$ s), we may safely conclude that the particles follow the flow well.

The honeycomb section just after the fill tubes exhibited a tendency to retain particles after a period of running, so the particle density could be observed to decrease within the tunnel over a period of 15 minutes or so. This made some readjustment of the particle density necessary just before each data run. Normally it was possible to simply flush the honeycomb by vigorously moving a squeegee behind it, but occasionally more particles were added to the system as a whole.

(d) Measurement of Different Locations

Velocity measurements were taken at five different depths within the tunnel, ranging from as near to the free surface as could practically be obtained (2.5 mm) before

sheet glare off the surface became unavoidable, to well into the “bulk” flow out of the free surface’s influence as confirmed by the work of Maheo (164 mm). A schematic is shown in Figure 2.10.

Five separate, slightly overlapping domains were interrogated at each depth, as depicted in Figure 2.11. It did not prove necessary to move or otherwise adjust the light sheet for separate cases at a given depth. When the depth was altered, the entire laser head/optics platform was raised or lowered as a unit, as were each camera and mirror individually. Final adjustment of the laser sheet’s position was performed by marking its location on pieces of paper taped to each sidewall of the water tunnel: The tunnel-off free surface of the water was used as the ultimate reference for orientation of the laser sheet, while the high-speed side while running was used to define depth.

(e) Image Capture and Calibration

At each measurement location (of the 25 in this set of experiments), several calibration images were recorded before and after the recording of the data images. All of these calibration images were taken in the same form as the data images – a three-color composite images consisting of all three cameras, each encoded as one color channel.

In addition to the calibration target used for dewarping discussed previously, a synthetic dot pattern was placed into the interrogation region (aligned with the laser sheet), and imaged a total of ten times. In between these ten captures the target pattern was translated in all three directions by known distances of up to 2 mm, and these images were stored for future reference for calibration verification. A second target was imaged once, this one simply containing printed text and reference directional arrows; this was to

ensure that the various steps of rotating and flipping the images during processing were done correctly.

The data-gathering phase of each measurement location consisted of the consecutive recording of 6,000 images, or 3,000 PIV pairs. These were written directly to the hard drive of the PC, as described previously. For this period of 200 seconds, the lights in the laboratory were extinguished to reduce the background intensity as much as possible.

After the recording of the data images, several shots were taken of rulers and metersticks held into the cameras' field of view. These images were not used to obtain the spatial scale of the images, as this was more accurately and easily accomplished using the dewarping grid images; rather, these images were used to positively locate the imaged area spanwise and streamwise, relative to the tunnel walls and the tip of the splitter plate. Some simple routines were performed for each case, using data points taken from these ruler images, to assign a global (x,y) value to the center of each window. The depth (z) was already known from the adjustment of the laser sheet.

(f) Processing Details

The 640x480 pixel images recorded by each camera were (after dewarping) processed using 32x32 pixel interrogation windows with a 50% (16 pixels) overlap. The window-shifting technique described by Westerweel *et al.* (1997) and Jeon (2000) was adapted to compensate for the very high mean velocity component in the streamwise direction. The time difference between images in a pair was long enough to allow particles to advect considerably farther than 32 pixels; this was necessary to allow the relatively smaller vertical and spanwise motions, as well as the streamwise turbulent

fluctuations, to be adequately resolved. The normally iterative window shifting approach was taken on the first processing pass by specifiying a uniform streamwise "shift" specific to each location's observed mean velocity.

After this first processing step, the standard operations of outlier removal and data smoothing as described by Raffel *et al.* (1998) were performed. The images were then re-processed using this vector field as the initial offset in window-shifting. The outliers were removed from this output, but data smoothing was not performed to avoid blurring out high-wavenumber features.

2.04 Comparison of 2-D and Stereo DPIV Results

The planar DPIV results obtained from the camera beneath the tunnel and the SDPIV results based on the two outboard cameras may be compared in several respects; this is briefly done in this section. Planar DPIV, as has been noted, provides only the two in-plane components of data, but these that are obtained may be directly compared to their SDPIV counterparts.

Figure 2.12(a-b) present a single realization of data for comparison. At a depth of z = -5.0 mm and one of the intermediate spanwise stations, a single image pair was chosen at random. Fully processed in both the planar and stereo DPIV methods described above, the data laying most near the x = 1000 mm downstream station was extracted and plotted for comparison.

It can be seen for both the streamwise component (u) and the spanwise component (v) that the agreement is generally good. Local discrepancies of as much as 5 mm/s are seen in the streamwise data, and nearly 10 mm/s in the spanwise velocity measurements. It should be noted that these data are not located at *precisely* the same

downstream station, and are in fact separated by about 0.6 mm. This is a significant amount, as it corresponds to about two-thirds of an interrogation window in the SDPIV processing procedure.

Spatial resolution between the two techniques was, in this application, slightly different. In the particular case presented above, the grid spacing was 2.08 mm for the planar DPIV processing, and 2.07 mm for the stereo. It would have been possible to adjust the DPIV resolution minutely by running the dewarping scheme on these images, as well, but it was felt that this would introduce unknown factors (not normally present in planar DPIV processing) that would serve to make direct comparison between the two techniques more difficult.

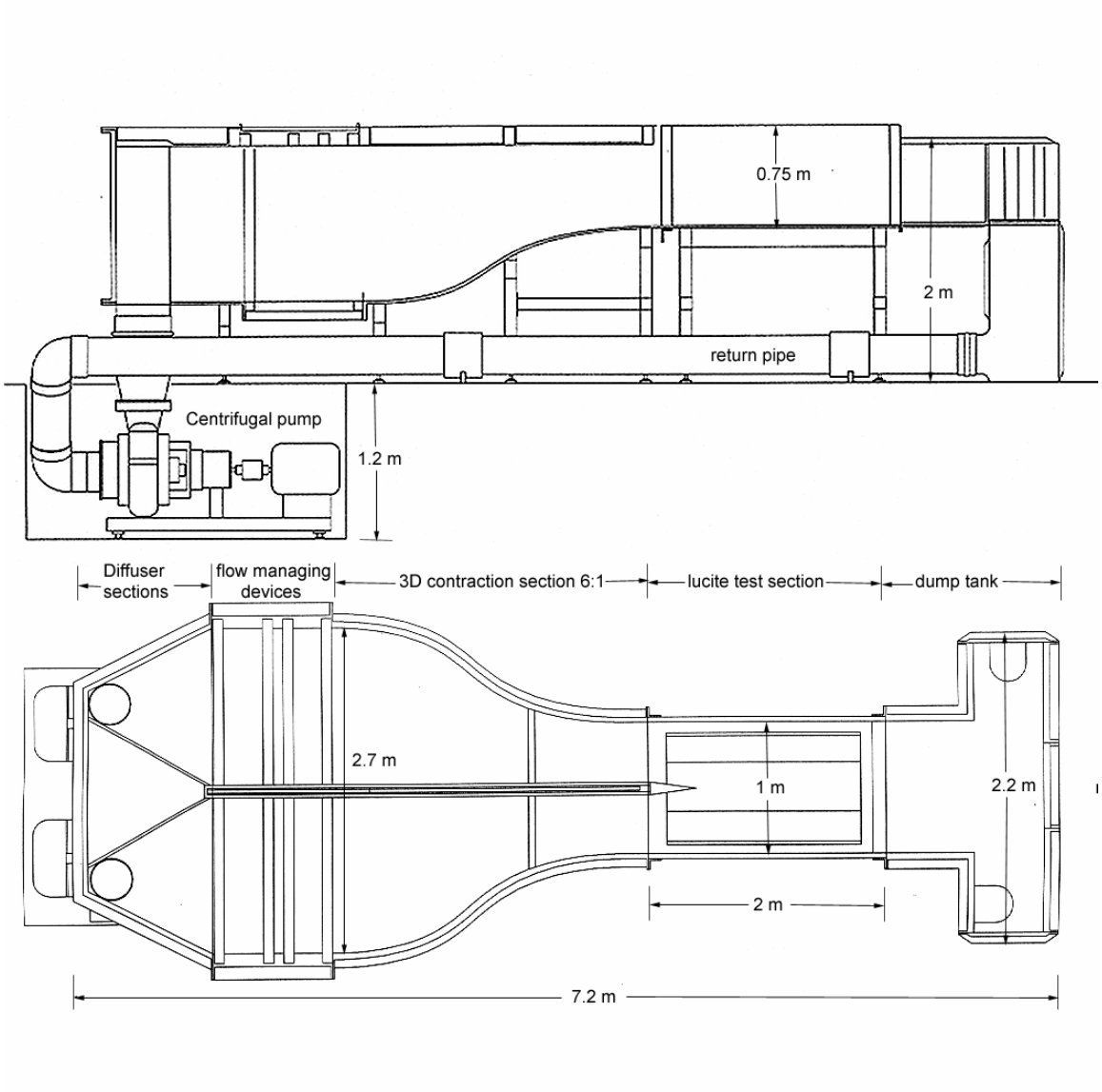

Figure 2.1: Schematic of GALCIT Free Surface Shear Layer Facility – side & top views

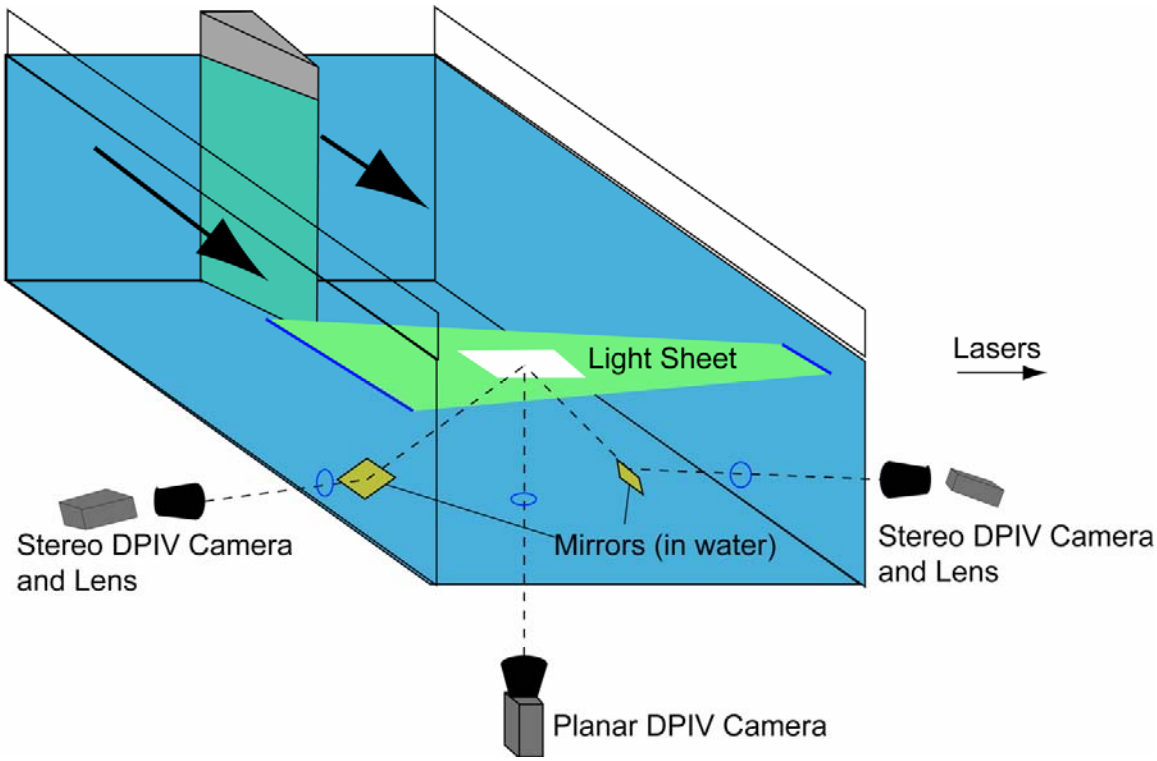

Figure 2.2: Schematic of test section and DPIV components

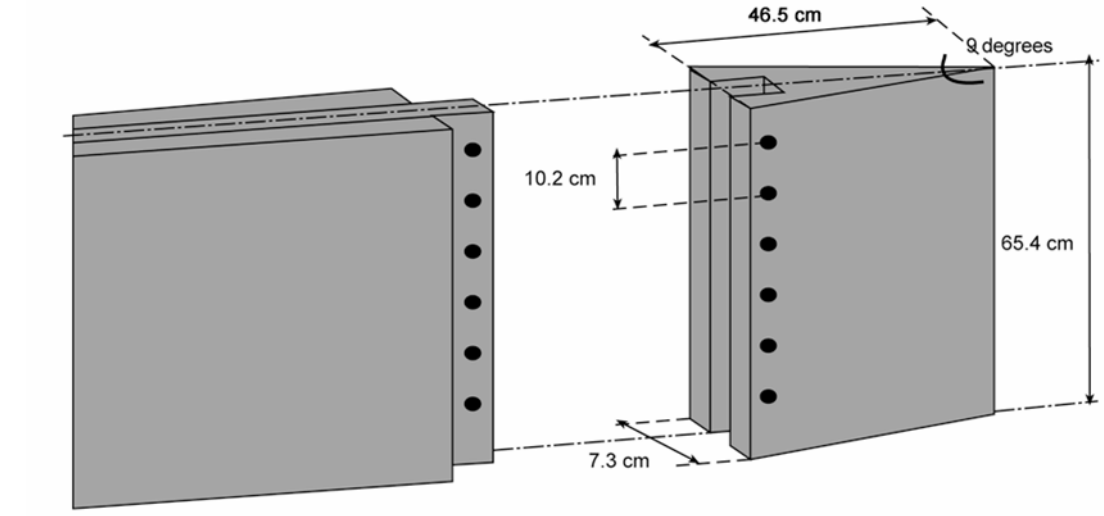

Figure 2.3: Splitter plate (not to scale)

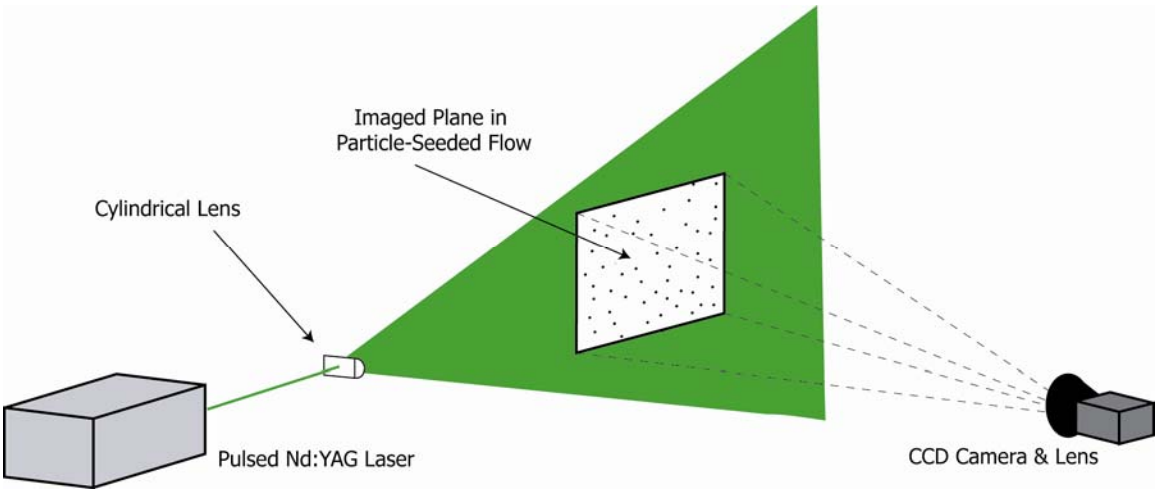

Figure 2.4: Schematic of typical planar DPIV arrangement

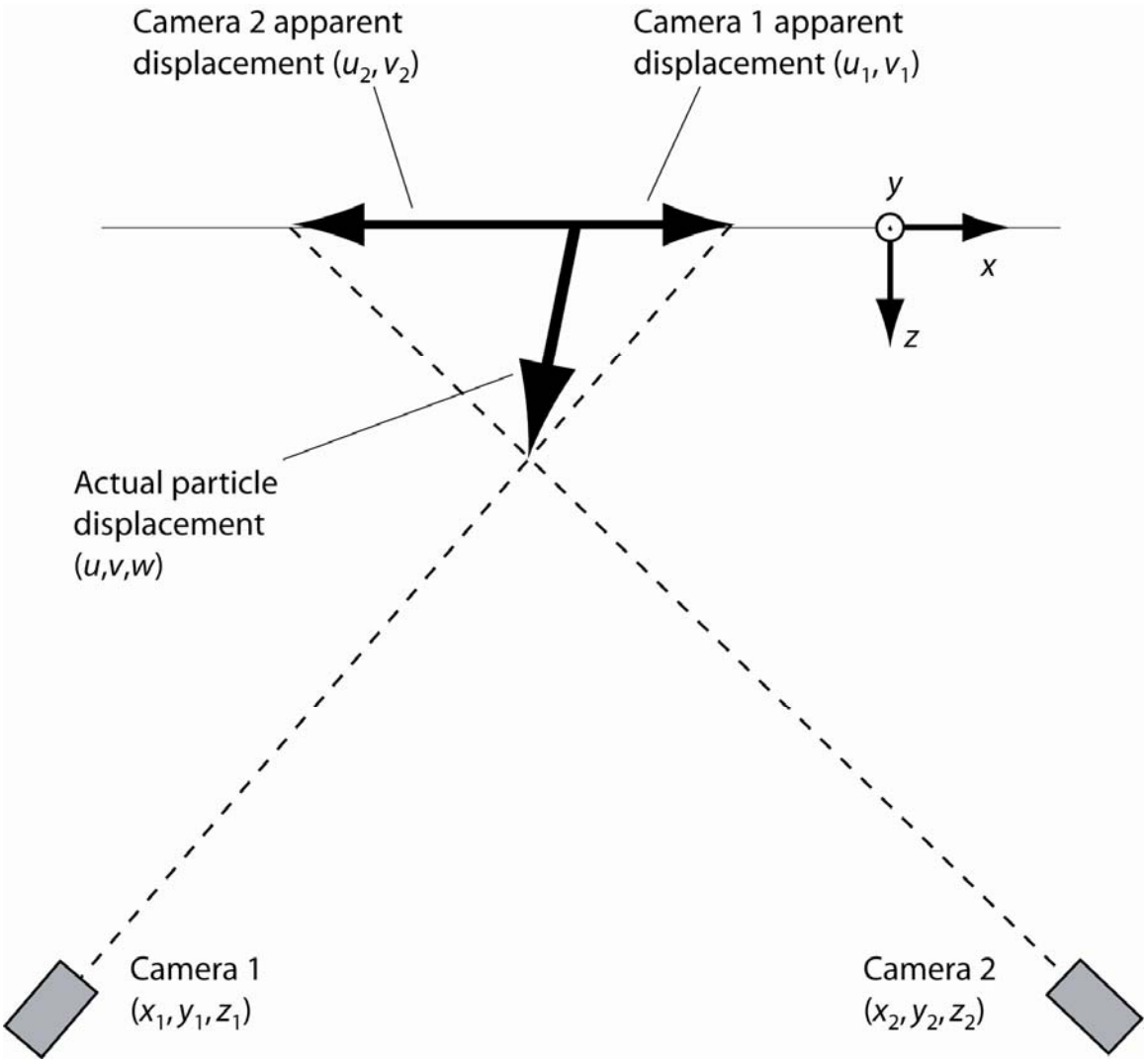

Figure 2.5: Schematic of Stereo DPIV triangulation process (overhead view)

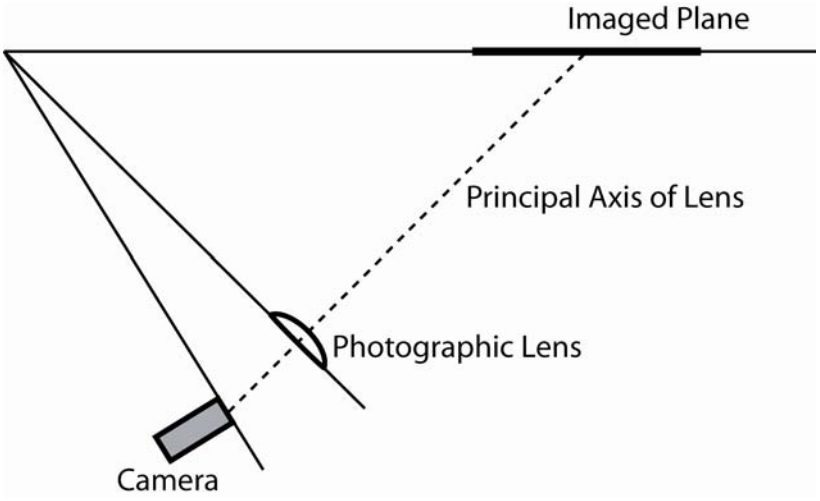

Figure 2.6: Illustration of "Scheimpflug criterion" for obtaining focused image in SDPIV

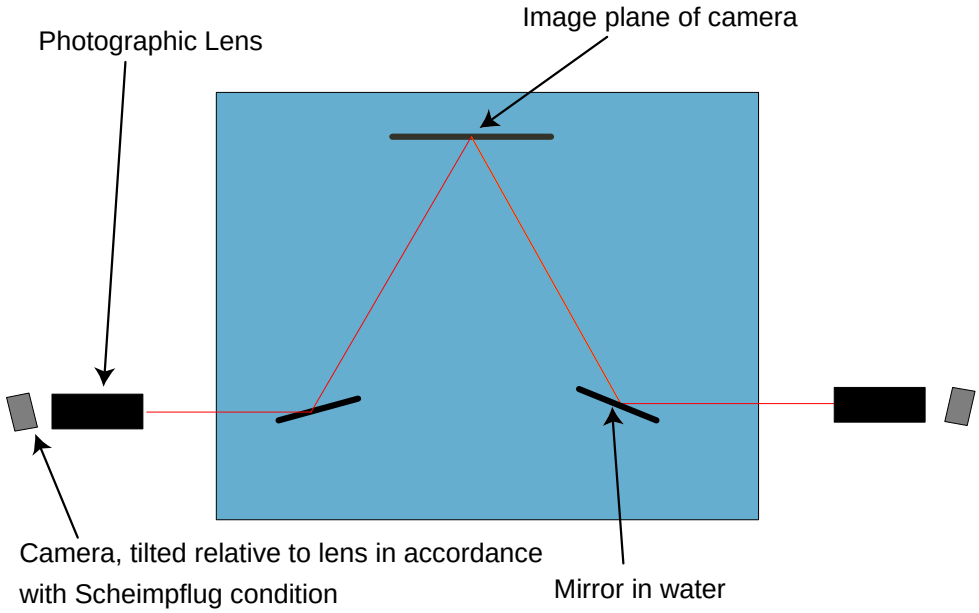

Figure 2.7: Upstream-view schematic of SDPIV setup, including mirrors in water

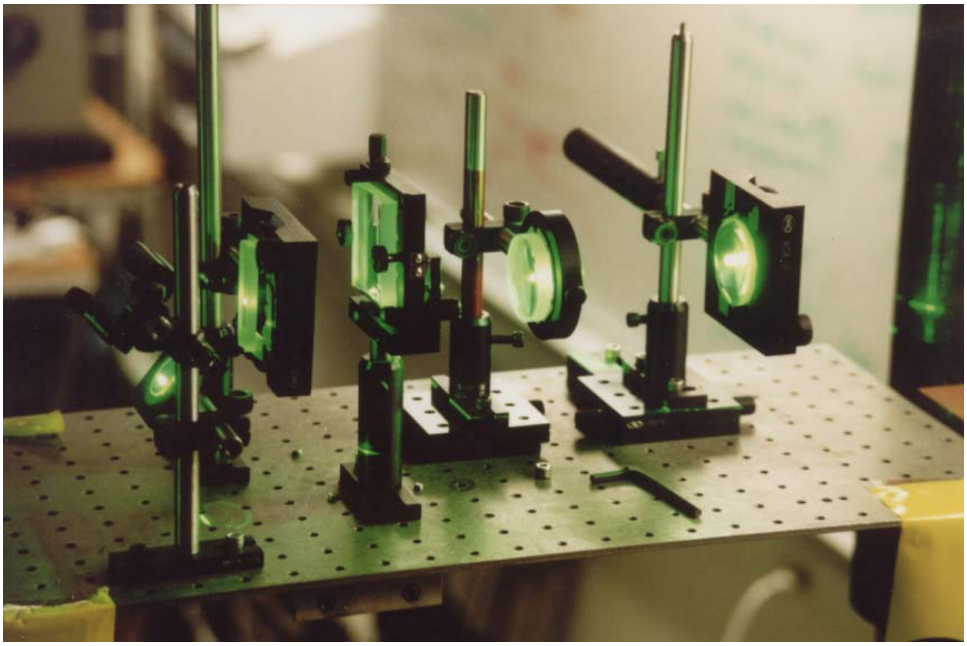

Figure 2.8: Photograph of lenses and mirrors used to create and direct laser light sheet

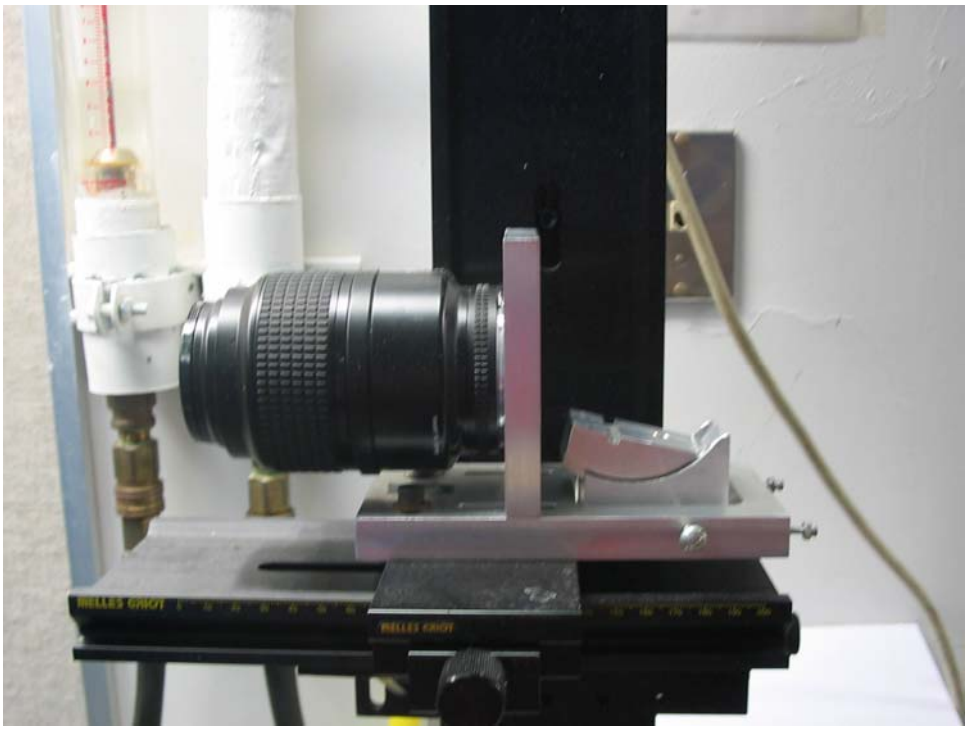

Figure 2.9: Camera housing allowing camera head (not shown) to rotate relative to lens

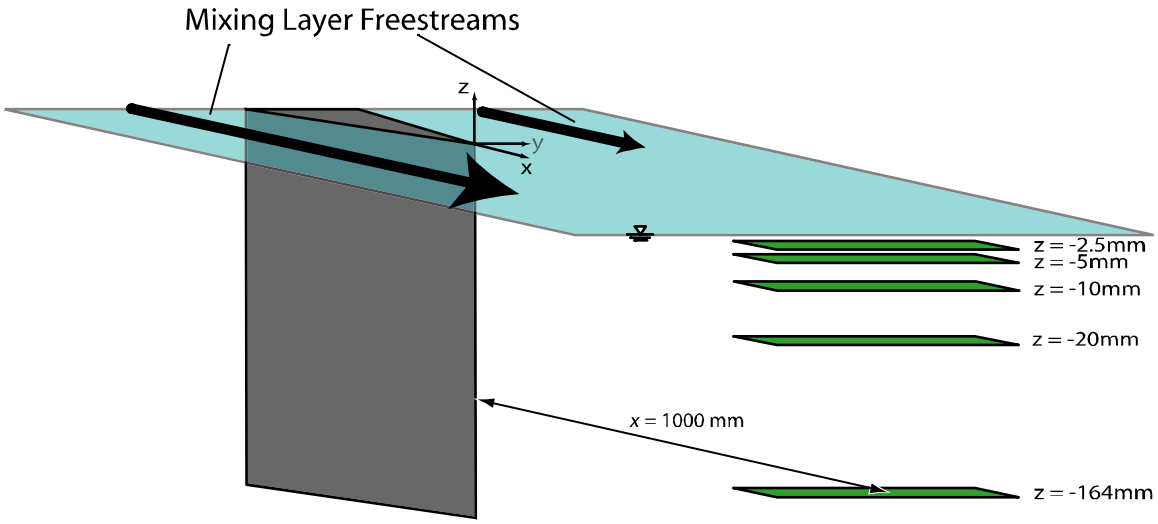

Figure 2.10: Schematic of SDPIV interrogation locations

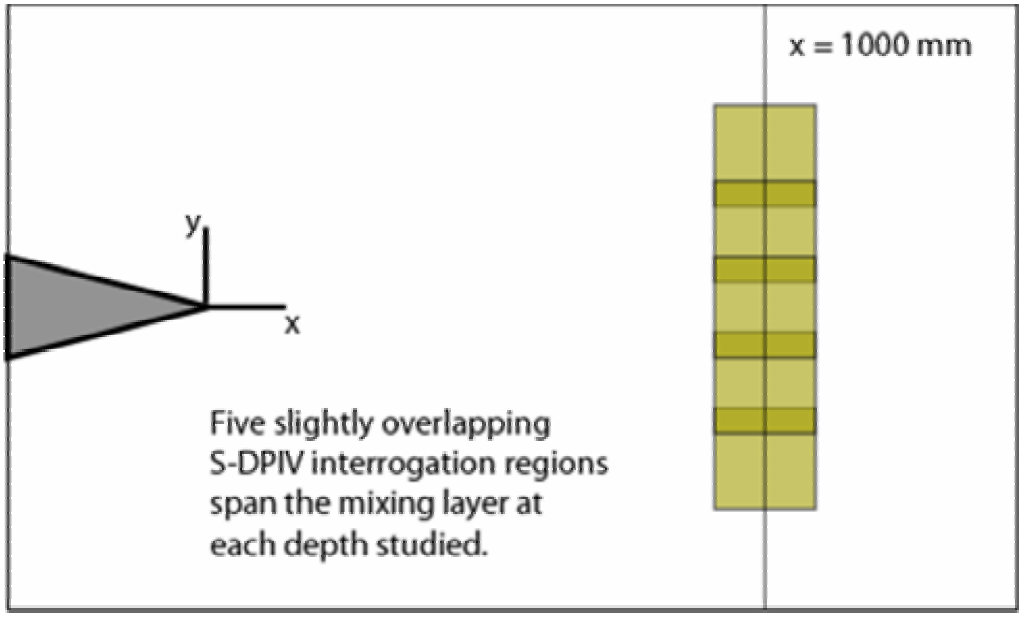

Figure 2.11: Schematic of overlapping interrogation domains at each depth studied

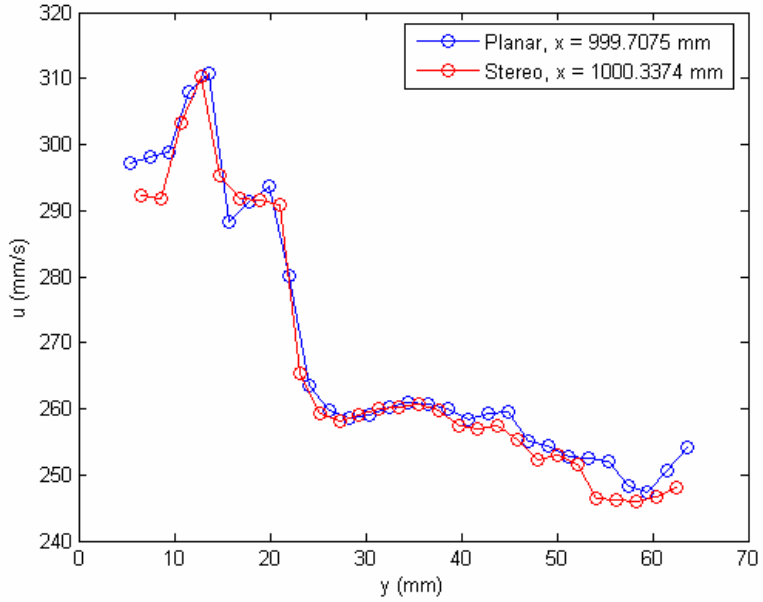

(a): Streamwise component

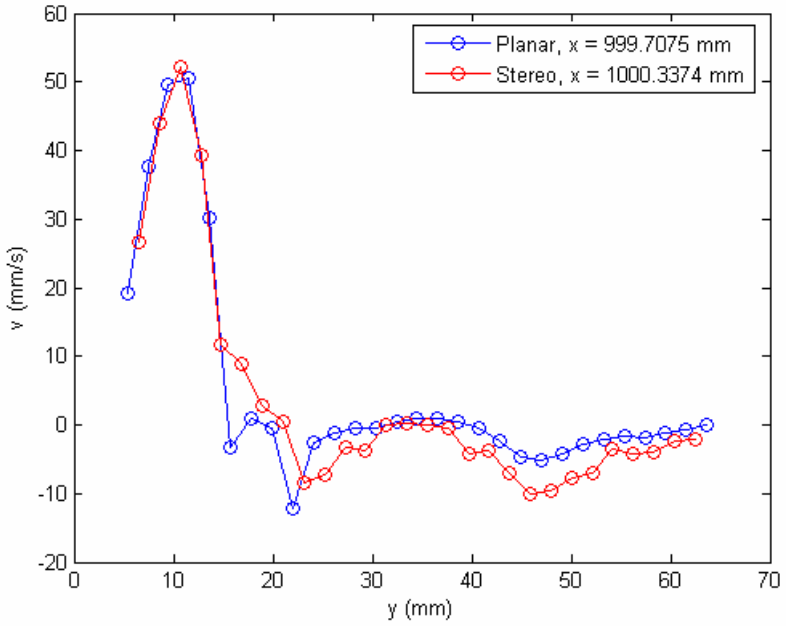

(b): Spanwise component

Figure 2.12: Comparison of Planar and Stereo DPIV - single realization

Chapter 3 Reynolds Decomposition

3.01 Flow Characterization at Depth

(a) Overview

SDPIV data as described in Chapter 2 was recorded and processed encompassing a downstream distance of x = 1m, in surface-parallel planes at z = -165 mm. In each instance, 3,000 individual three-component velocity fields were obtained, uniformly separated in time by Δt = 1/15 s. By thinking of this collection of data to be the time history of the velocity components at each of many spatial locations, it is then straightforward to perform Reynolds decomposition in the following fashion:

$$\mathbf{u}(\mathbf{x},t) = \mathbf{U}(\mathbf{x}) + \mathbf{u}'(\mathbf{x},t)\,;$$

where **U** represents the time-average of the velocity vector, and **u'** is the instantaneous fluctuation of the velocity about the mean. The vectors shown above may be represented by three Cartesian components as follows:

$$\begin{gathered}\mathbf{x} = (x, y, z) = (x_1, x_2, x_3);\\ \mathbf{u} = (u, v, w) = (u_1, u_2, u_3);\\ \mathbf{U} = (U, V, W) = (U_1, U_2, U_3);\\ \mathbf{u}' = (u', v', w') = (u_1', u_2', u_3').\end{gathered}$$

The former representation will be that used within this thesis except where the Einstein summation convention makes the use of the subscripted representation more appropriate.

This Reynolds decomposition as described above is both convenient and a useful tool for analysis. Given the Navier-Stokes equations

$$\frac{\partial u_i}{\partial t} + u_j \frac{\partial u_i}{\partial x_j} = -\frac{1}{\rho}\frac{\partial p}{\partial x_i} + \nu \frac{\partial^2 u_i}{\partial x_j^2},$$

where the Einstein summation convention is used (p is pressure, ρ the fluid density, and ν the kinematic viscosity), a substitution of the Reynolds averaged velocity components $u_i = U_i + u_i'$ yields the so-called Reynolds averaged Navier-Stokes (RANS) equations

$$U_j \frac{\partial U_i}{\partial x_j} = -\frac{1}{\rho}\frac{\partial \bar{p}}{\partial x_i} + \nu \frac{\partial^2 U_i}{\partial x_j^2} - \frac{\partial \overline{u_i' u_j'}}{\partial x_j}.$$

The overbar represents a time average of the particular quantity. It is useful to note that the fluctuating part of the velocity components appear in the RANS equations only in the final term – all other terms are based solely on mean quantities. The arguments of the derivatives of this final term ($\overline{u_i' u_j'}$) are referred to as the *Reynolds stresses*. Since the Reynolds stress terms are frequently convenient to measure, analysis of them (or, specifically, their gradients) may lead to significant understanding of physical mechanisms, such as that done by Maheo (1998). The six (distinct) Reynolds stresses are elements of a tensor quantity in the RANS equations as given above; it is not uncommon to refer to the *Reynolds stress tensor*.

It is also possible to calculate the surface-normal component of vorticity, $\omega_z = \partial v/\partial x - \partial u/\partial y$, instantaneously within each velocity field. This is done using a finite-difference routine that is part of the DPIV software package used. A similar Reynolds decomposition may be performed upon these values:

$$\omega_z(\mathbf{x}, t) = \overline{\omega_z}(\mathbf{x}) + \omega_z'(\mathbf{x}, t).$$

Commonly examined quantities, based on the mean values and fluctuation histories described above, are extracted at x = 1m and presented in the remainder of this chapter.

(b) Normalization Values

The mean streamwise velocity component profile at x = 1000 mm, in real coordinates, is shown in Figure 3.1. This set of data, taken at a depth of 164 mm, will be treated as the "bulk" flow in the sense of Maheo; his data supports this contention, as the free surface influence appears to have disappeared well before reaching this depth for this flow.

U_1 and U_2 are the high- and low-speed freestream speeds, respectively. ΔU is defined as U_1- U_2. The speed at which structures in the flow are advected downstream is typically well-approximated by $U_C = \frac{1}{2}(U_1 + U_2)$, as pointed out by Dimotakis & Brown (1976), among others.

The transverse extent of the mixing layer at depth will be defined here by the vorticity thickness, which we define by

$$\delta_\omega \equiv \frac{\Delta U}{\left|\frac{dU(y)}{dy}\right|_{\max}}.$$

Evaluation of this quantity was quite straightforward based on the mean velocity data presented in the previous section: calculation of the mean velocity derivative was done using a simple finite-difference scheme.

The normalization values thus obtained are as follows:

$$U_1 = 379 \text{ mm/s};$$
$$U_2 = 252 \text{ mm/s};$$
$$\Delta U \equiv U_1 - U_2 = 127 \text{ mm/s};$$
$$U_C \equiv \tfrac{1}{2}(U_1 + U_2) = 316 \text{ mm/sec};$$
$$\delta_\omega = 80.5 \text{ mm}.$$

These are the values used (at all depth levels), as appropriate, to normalize the various quantities presented throughout this work. It has been shown to be appropriate in flows of this type to normalize downstream distance by the momentum thickness as measured at the tip of the splitter plate (Maheo, 1998). The value used here is taken from the data of Maheo: $\theta_i = 4.8$ mm.

(c) Inner Scaling

It is also instructive to obtain estimates of what are often referred to as the "inner scales" of the flow – the scales at which viscous dissipation takes place. For the purposes of these estimates, the assumption of isotropic turbulence is made. The values are calculated for the bulk flow (z = -164 mm), a downstream distance x = 1000 mm, and at the location of peak velocity fluctuation ($y \sim 0$). The isotropy assumption, which data presented in Chapter 5 will show is approximately satisfied at this location, greatly simplifies the calculation of these inner scales.

The viscous dissipation rate per unit mass ε may be estimated using the relation

$$\varepsilon = 15\nu\overline{\left(\frac{\partial u'}{\partial x}\right)^2} = 1.2\times10^{-4}\ \mathrm{m^2 s^{-3}},$$

where as previously the overbar denotes a time average. The velocity derivative is straightforward to calculate given the SDPIV data available, and ν is the kinematic viscosity of the fluid. The Kolmogorov length scale, λ_k, may be estimated based upon this dissipation value according to

$$\lambda_k = \left(\frac{\nu^3}{\varepsilon}\right)^{1/4} = 3.0\times10^{-4}\ \mathrm{m},$$

or about 0.3 mm. This is approximately an order of magnitude smaller than the spatial resolution of the SDPIV data in this experiment. The Kolmogorov velocity scale u_k may be estimated according to

$$u_k = (\nu\varepsilon)^{1/4} = 3.3\times10^{-3} \text{ m/s};$$

the Kolmogorov time scale based on these values is thus

$$\tau_k = \frac{\lambda_k}{u_k} = 9\times10^{-2} \text{ s}.$$

Also of interest is the Taylor scale, given by the expression

$$\lambda_T = \left[\frac{\overline{u'^2}}{\overline{\left(\partial u'/\partial x\right)^2}}\right]^{1/2} = 8.1\times10^{-3} \text{ m};$$

at approximately 8 mm this scale lies within the spatial resolution of the present experiment. The Taylor Reynolds number at that location in the flow is given by

$$Re_T = \frac{\left(\overline{u'^2}\right)^{1/2}\lambda_T}{\nu} = 180.$$

On the basis of these values we may refer to the work of Dimotakis (2000), in which it is argued that *necessary* but not *sufficient* conditions for *fully developed* turbulent flow are an outer-scale Reynolds number $Re \geq 1-2\times10^4$, or a Taylor Reynolds number $Re_T \geq 100-140$. The values in the present experiment for those two parameters are $Re = \Delta U\delta_\omega/\nu = 10{,}200$ and $Re_T = 180$, placing us at approximately those thresholds.

3.02 Flow Property Variations with Depth

(a) Selection of Depths for Interrogation

The depths at which measurements were taken in the experiments described in this thesis were determined based on the data obtained by Maheo (1998) in his study of the same flow in the same facility. Figure 3.2 depicts mean velocity vectors and vorticity contours at the downstream station x = 1000 mm ($x/\theta_i = 210$). The plane of the figure normal to the x-axis; the mean flow is out of the page. z = 0 represents the free surface, while y = 0 denotes the mixing layer centerline; both spatial coordinates are normalized by the vorticity thickness.

The primary features of note are the two counter-rotation vortical structures sitting astride the mixing layer centerline, just below the free surface. Of key interest in the present experiments was understanding of the dynamics in the vicinity of the free surface, and these vortical structures were suspected to play an important role. Four interrogation depths near the free surface were thus chosen to be z/δ_ω values of -0.25, -0.12, -0.062, and -0.031. These depths are indicated by the red bars on the left side of Figure 3.2 (the uppermost two depths are too close together to resolve as separate lines). The fifth interrogation depth was selected as z/δ_ω = -2.0, which the data of Maheo demonstrates to be effectively out of the influence of the free surface. This depth also represented the maximum distance below the free surface which was accessible to the SDPIV setup as described.

(b) Mean Velocity

Figure 3.3 shows the normalized mean streamwise velocity profile at $x/\theta_i = 210$, at various depths. It can be seen that effective freestream speeds on both sides of the mixing layer are depth-dependent, with freestream speeds (and corresponding in-layer speeds) rising from their bulk flow values by as much as five percent before falling again extremely close to the free surface. The presence or absence of this phenomenon is not reported in the work of Maheo – his "wake mode" freestream measurements showed only slight (and monotonic) variations of freestream speed with depth. There is also visible what may be thought of as a "wake component" in the profiles at the three most shallow profiles: Even well outside the well-defined mixing layer, the mean streamwise component is seen to gradually increase with distance from the centerline.

It is also clear that the width of the mixing layer varies strongly with depth. Figure 3.4 presents the *locally calculated* vorticity thickness $\delta_\omega^{\text{local}}$ (calculated as described previously, and normalized by the bulk vorticity thickness) as a function of normalized depth. The layer can be seen to narrow from its bulk width before growing more broad close to the free surface. The data of Maheo supports the assumption that the vorticity thickness is essentially constant with depth well before $z/\delta_\omega = -210$, and also indicates the pronounced narrowing and then widening of the profile as the free surface is approached from depth which is shown more quantitatively by the present data.

Figure 3.5 presents the normalized mean spanwise velocity profile, at the same locations. It is clear that the sharp upwards and downward peaks in the profile become considerably larger and more pronounced as the free surface is approached from below. It should be noted that the $V > 0$ nearly everywhere across the profile. This is in keeping

with the well-documented tendancy for the mean flow to be towards the low-speed stream (which lies to the positive *V* direction). The data of Maheo does not appear to reflect this trend, but it should be noted that the coordinate axes of the data presented here have not been rotated relative to the tunnel walls. Maheo performed this coordinate rotation in order to align the *x*-axis with the centerline of the mixing layer as it developed downstream.

The differing profiles of *V* with depth are consistent with the surface currents which Walker (1997) observed to be present in all turbulent shear flows in the vicinity of a free surface. Of particular note is the differing shape of the *V* profile at $z/\delta_\omega = -0.25$; this depth is just below the core of the persistent streamwise vortices identified by Maheo. On both sides of the mixing layer, the streamwise vorticity which may crudely be estimated simply by $\Delta V/\Delta z$ is of the proper sign to support the vortices reported there.

It is in this mean spanwise velocity component that the overlapping SDPIV data appears to have the poorest agreement – particularly in some segments in the bulk. The cause of this is believed to be very slight misalignments of the dewarping grid, upon which the streamwise and spanwise directions are ultimately based for each individual data run. Since the mean streamwise component is very large compared to the spanwise, very slight rotation of the grid will result in errors that are too small to notice in the streamwise direction, but that are quite apparent in the spanwise. The obvious poor overlap in the data in the bulk ($z/\delta_\omega = -2.0$) on the high-speed side, for example, may be analyzed trigonometrically and shown to stem from a grid rotation of just under 1^o.

Figure 3.6 presents the normalized vertical velocity profile, at the same locations. In the bulk flow, there is a pronounced region of mean flow in the direction of the free surface ($W > 0$), which more or less disappears in the intermediate depths shown. In the vicinity of the free surface this upwelling mean flow is seen to decrease markedly in magnitude.

(c) Surface-normal Vorticity

Figure 3.7 shows the mean surface-normal vorticity values at various depths. As before, these values are normalized by the bulk flow parameters. The center of the vorticity peak can be seen to be biased towards the low speed side for all levels besides that of the bulk flow. The relative widths of the peaks also follow the general trend observed in the previous section based on the mean streamwise velocity profile: narrowing at some intermediate depths ($z/\delta_\omega = -0.12$ and -0.25, respectively), and then growing to exceed the deep width as the free surface is neared.

Where the width of the peak is reduced, the magnitude of its peak value is increased: Figure 3.8 shows the maximum value of vorticity as a function of depth. This is to be expected, as the general relation $\int_{-\infty}^{\infty} \left|\overline{\omega_z}\right| dy = \Delta U$ should hold. It was shown previously that ΔU is approximately constant at all depths studied, and so it is reasonable to expect that the area under the vorticity profile curve should be approximately equal at all depth levels.

(d) Velocity Component Fluctuations

Given the time history of all three velocity components made available through SDPIV, it is straightforward to compute the root-mean-square fluctuation intensity of

each component of velocity across the width of the mixing layer, at each depth. Figure 3.9 shows the normalized profile of $\sqrt{\overline{u'^2}}$ across the mixing layer at the five depths examined. As noted with previously discussed quantities, the peak of the fluctuation intensity is shifted towards the low speed stream for all near-surface levels (relative to that in the bulk). Peak widths behave in a manner similar to that of the vorticity described previously. Figure 3.10 shows the maximum as a function of depth. It is seen that the peak values at all near-surface levels is somewhat higher than that in the bulk, with the highest – and most narrow – peak occurring at $z/\delta_\omega = -0.25$. This is the depth at which the mean velocity and mean vorticity profiles were also observed to be at their least wide.

Figure 3.11 shows a similar collection of $\sqrt{\overline{v'^2}}$ profiles. In this, the spanwise direction, we note that profile peak intensity values vary far less with depth than do those of streamwise intensity. Variations in peak width with depth follow the trends described previously for other Reynolds averaged quantities. Figure 3.12 shows the maximum value as a function of depth; the variation is very small by comparison to the other components.

Figure 3.13 reveals normalized vertical velocity fluctuation intensity, $\sqrt{\overline{w'^2}}$, plotted in the same manner. Figure 3.14 shows the maximum as a function of depth: In this component, the dependence on depth is most pronounced: There is a monotonic reduction in peak value with reducing depth. The same peak width and spanwise offset characteristics noted for other fluctuating quantities are noted in this case.

The curious increase in the $\sqrt{\overline{w'^2}}$ values as the high-speed freestream is approached is quite noticeable. The origin of this observation is not entirely clear; it should be noted, however, that the values of *W* are still fairly high at that spanwise station. Surface current activity of some type is entirely possible, and given the similar behavior of two independent data sets (the two most near the free surface) it is considered unlikely to be an artifact.

(e) Reynolds stresses

The three-component nature of the SDPIV data make it possible to calculate the three distinct off-diagonal components of the Reynolds stress tensor, as well. Figure 3.15 shows a normalized profile of $\overline{u'v'}$ at several depths at $x/\theta_i = 210$. A pronounced peak is seen in each case, and the location of the peak's center varies with depth in a manner very similar to those of other quantities presented previously. The magnitude of the peak value is seen to be considerably higher at $z/\delta_\omega = -0.25$ than at any other depths, mirroring the trend observed in the $\overline{\omega_z}$ profiles. The two profiles most close to the free surface exhibit somewhat lower peak values than those seen at considerable depth; at $z/\delta_\omega = -0.12$ the profile can be seen as intermediate between that seen in the extreme near-surface region and that observed at double the depth. Figure 3.16 shows the maximum as a function of depth.

Figure 3.17, at the same location and depths, shows normalized profiles of $\overline{u'w'}$. Clear distinctions between the profiles at the different depths are not apparent: Peak heights and widths appear similar. The peak values are considerably lower – by a factor of approximately five – than those of the equivalent $\overline{u'v'}$ values. The peaks' spanwise

position with depth changes in approximately the same manner that has been observed in all quantities so far presented. Figure 3.18 shows the maximum as a function of depth, and highlights the relatively low variation.

Figure 3.19, also at the same locations, shows normalized profiles of $\overline{v'w'}$. This quantity is seen to remain very near zero in value at the two levels most near the free surface: $z/\delta_\omega = -0.031$ and $z/\delta_\omega = -0.062$. Low-magnitude peaks are observed in the intermediate depths, but the values are sharply increased in the bulk flow. This profile peak value outside the influence of the free surface is greater than that of $\overline{u'w'}$ at the same depth by approximately 60 percent. Figure 3.20 shows the maximum as a function of depth.

Figure 3.21, also at the same locations, shows normalized profiles of the three-component turbulence kinetic energy, $E = \overline{u'^2 + v'^2 + w'^2}$. Many of the general trends observed in the individual component intensities may be seen, such as the pronounced narrowing of the profile and raised peak value at $z/\delta_\omega = -0.25$ and $z/\delta_\omega = -0.12$. In the very near surface region the total energy of the fluctuations is seen to take a profile similar to that in the bulk, but slightly wider and with a slightly lower peak value. Figure 3.22 shows the maximum as a function of depth. The turbulence kinetic energy *E* is clearly a function of *y* at each depth, and we may integrate across the measurement domain to obtain the total amount of energy at each depth: $E_{total} = \int E(y)dy$. This value as a function of depth is plotted in Figure 3.23, where we see that the quantity is nearly independent of depth at all locations observed.

(f) Near-Surface Data

An unfortunate consequence of what appear to have been surface waves is that some elements of the very near-surface data are not suitable for use in the comparison of some of the parameters to be presented in this section. Primarily noted by the presence of considerable streamwise variation in select components, the data which is clearly misleading has been omitted from the expositions below. Details of the process by which data was vetted, and a discussion of this issue as a whole may be found in Appendix B.

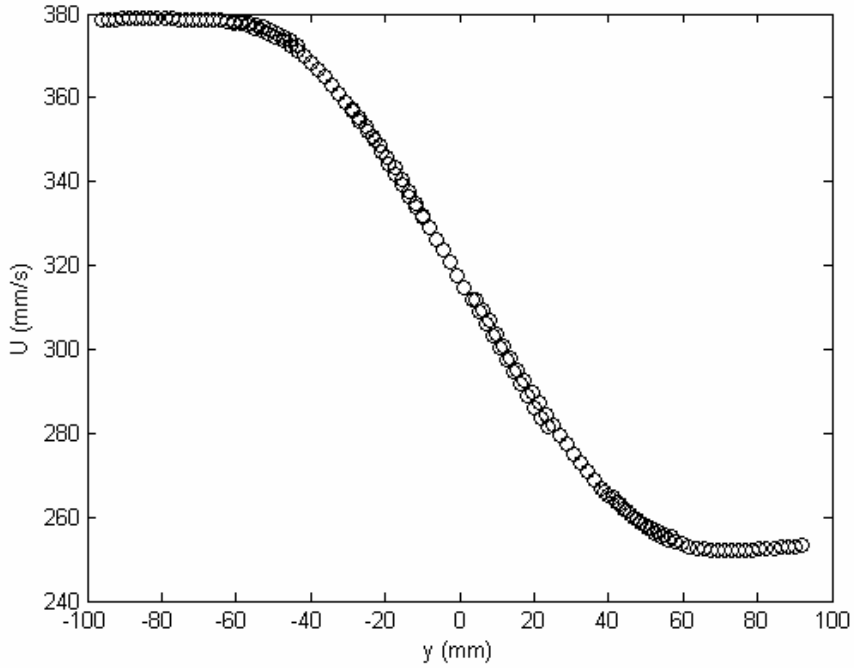

Figure 3.1: Mean streamwise velocity profile, x = 1000 mm, z = -164 m

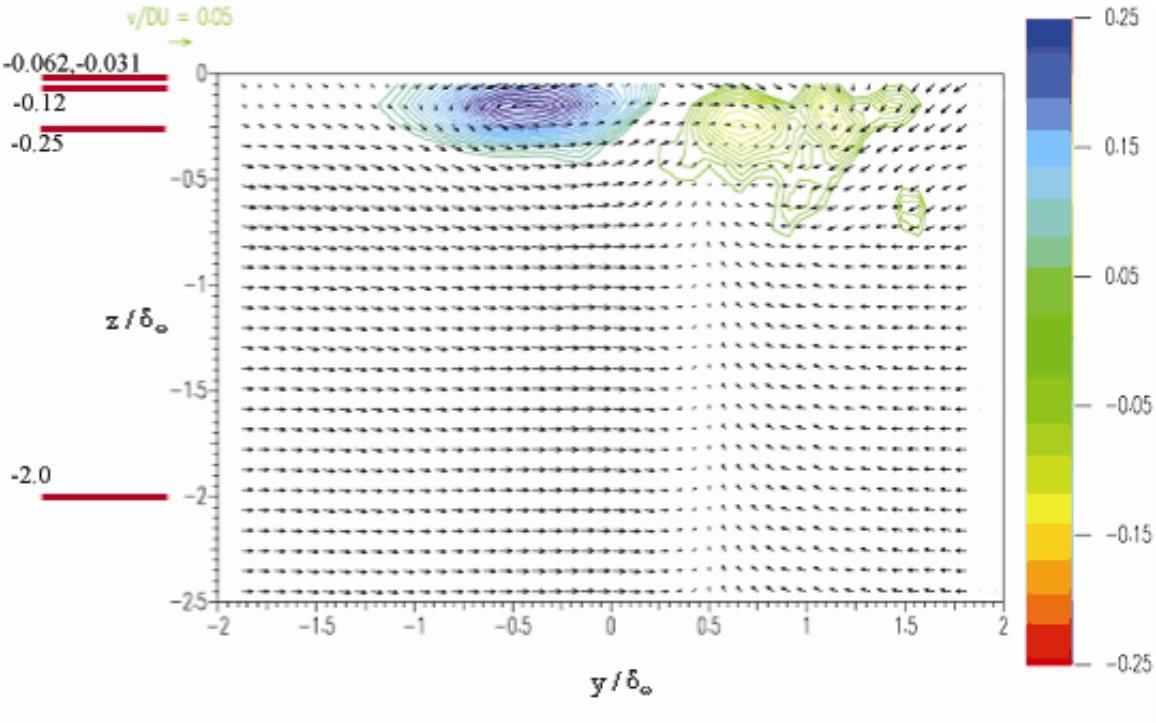

Figure 3.2: Upstream view of mean velocity, vorticity data of Maheo, x = 1000 mm – red lines at left denote interrogation depths in present work

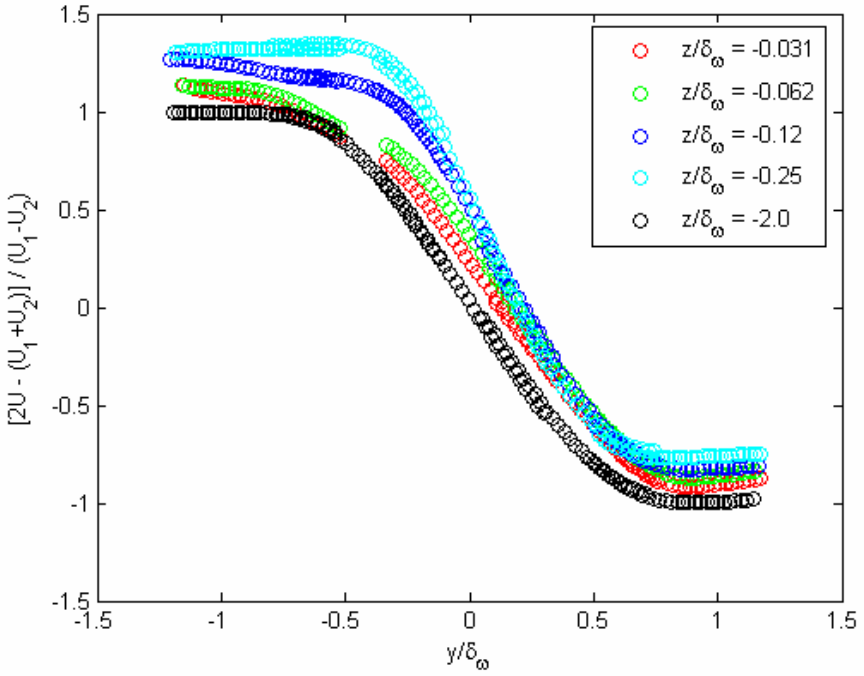

Figure 3.3: Normalized mean streamwise velocity profiles, x/θ_i = 210

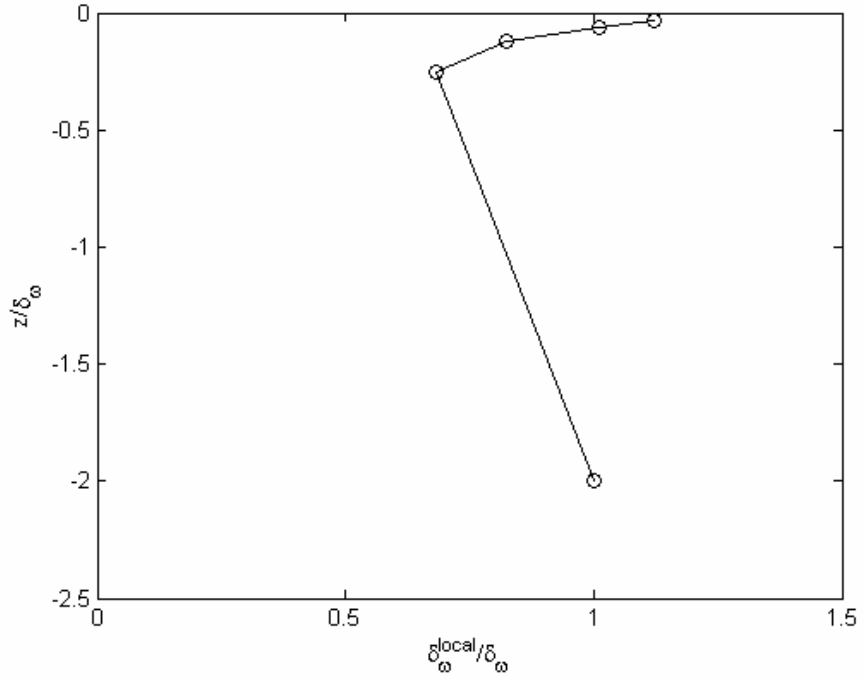

Figure 3.4: Locally calculated vorticity thickness vs. depth, x/θ_i = 210

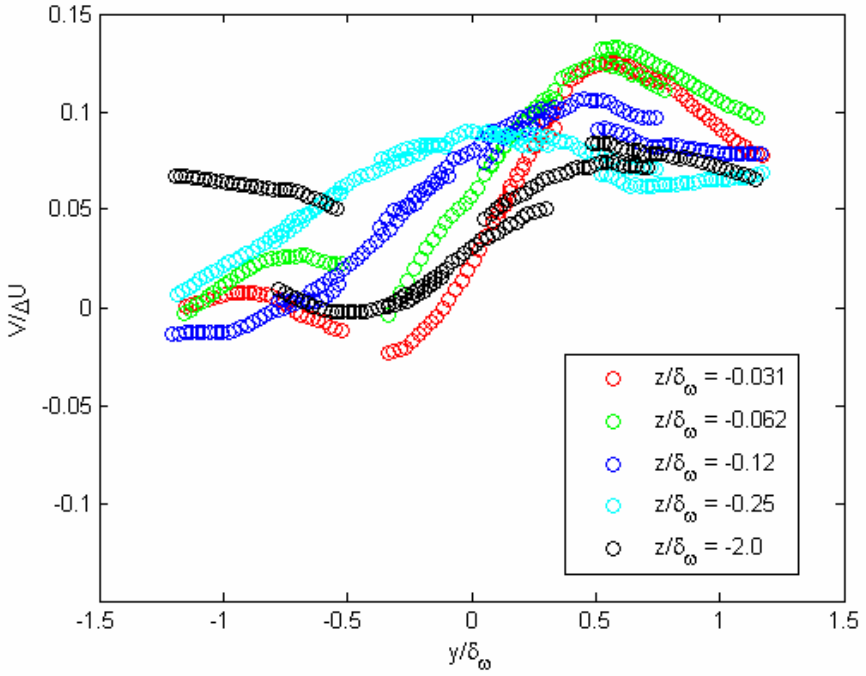

Figure 3.5: Normalized mean spanwise velocity profile vs. depth, $x/\theta_i = 210$

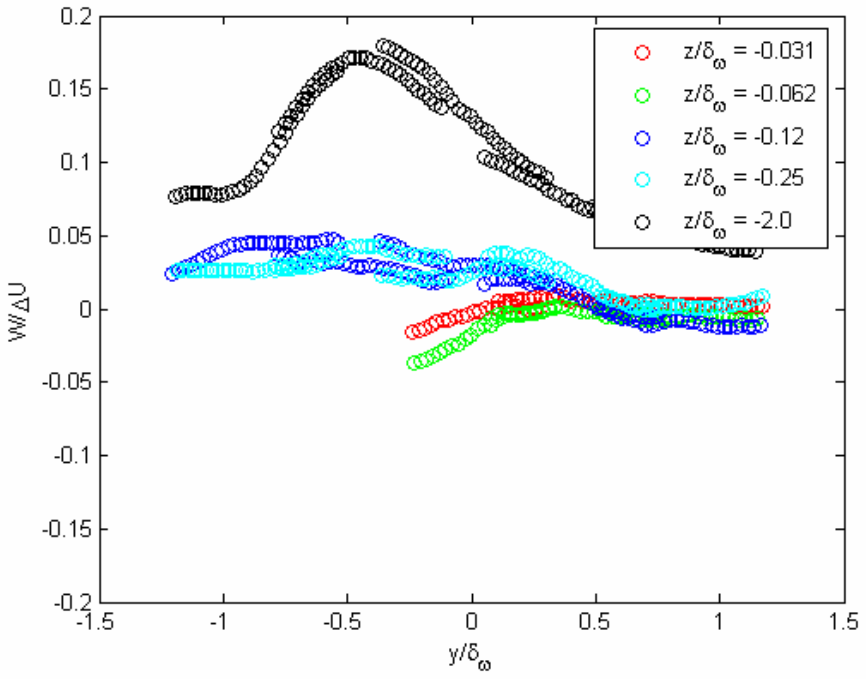

Figure 3.6: Normalized mean vertical velocity profile vs. depth, $x/\theta_i = 210$

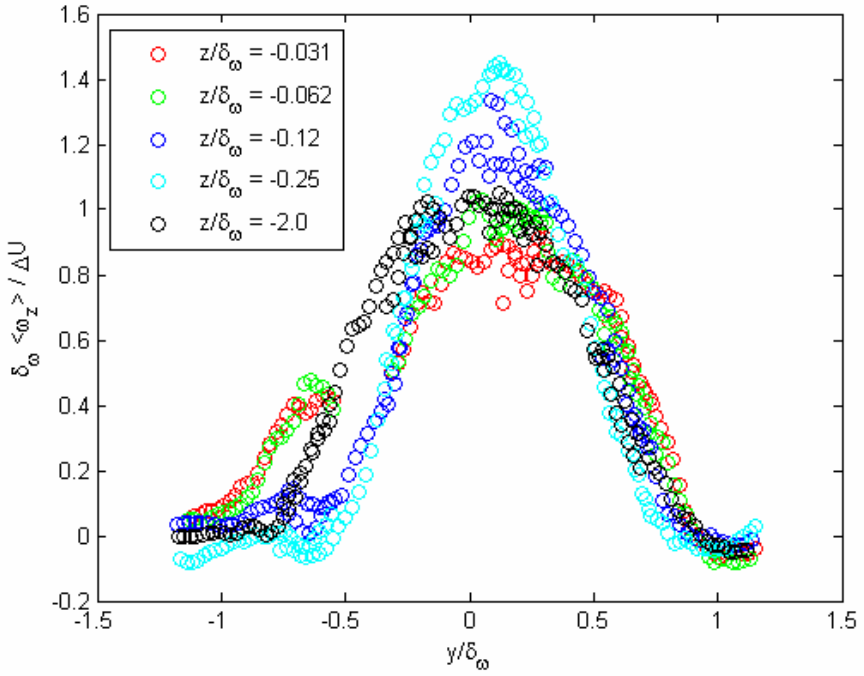

Figure 3.7: Normalized mean surface-normal vorticity profile vs. depth, $x/\theta_i = 210$

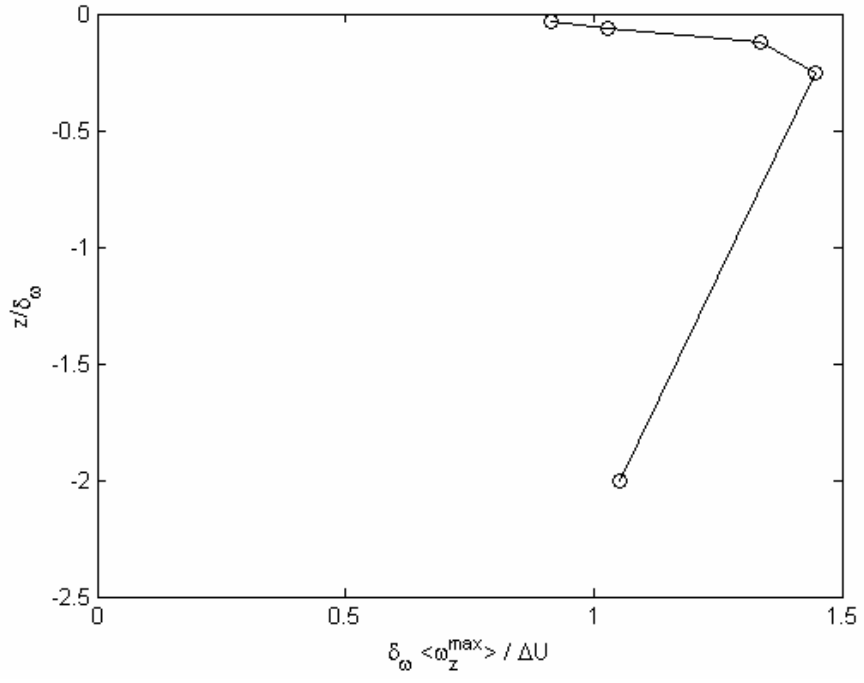

Figure 3.8: Maximum vorticity level vs. depth, $x/\theta_i = 210$

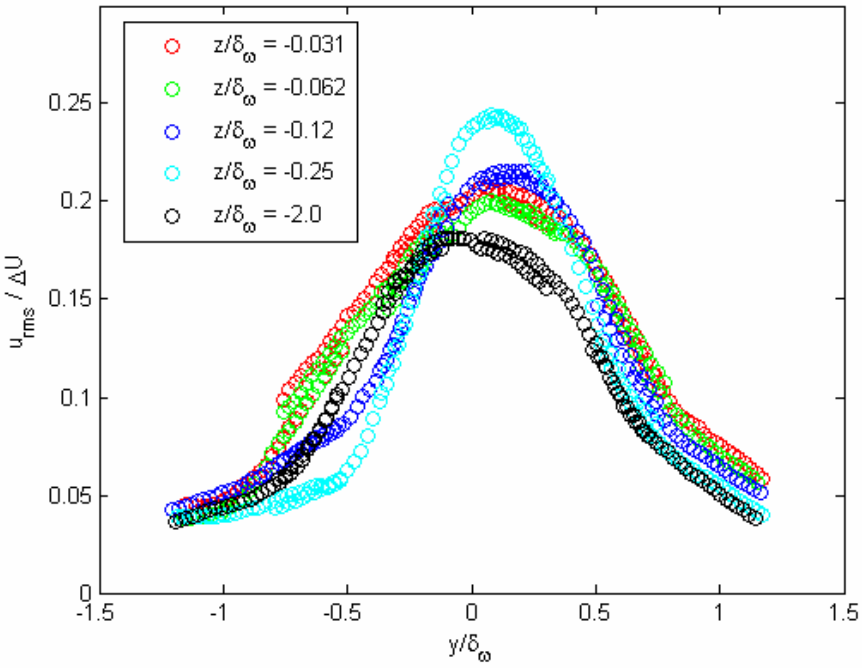

Figure 3.9: Normalized streamwise velocity fluctuations vs. depth, $x/\theta_i = 210$

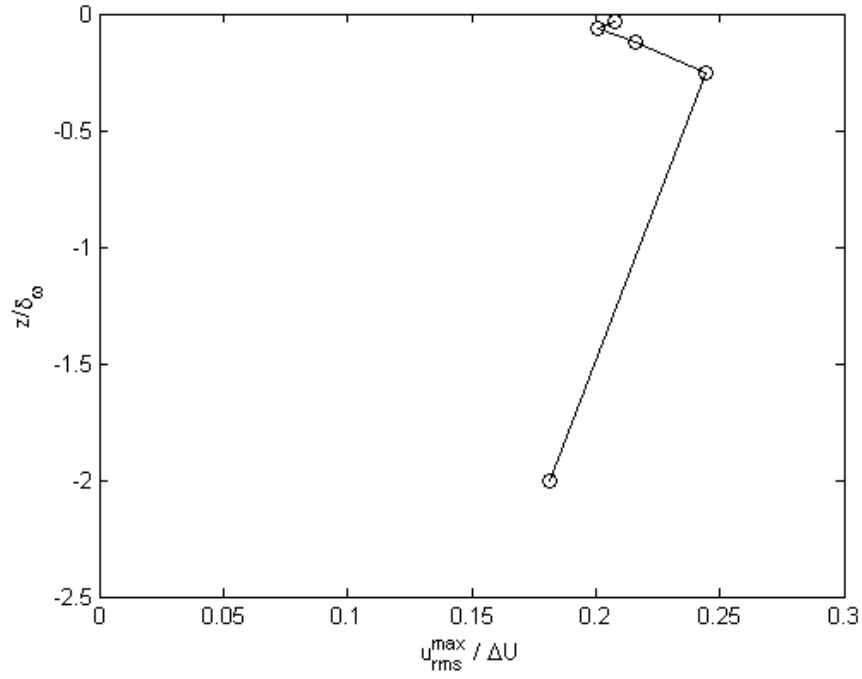

Figure 3.10: Maximum streamwise velocity fluctuation vs. depth, $x/\theta_i = 210$

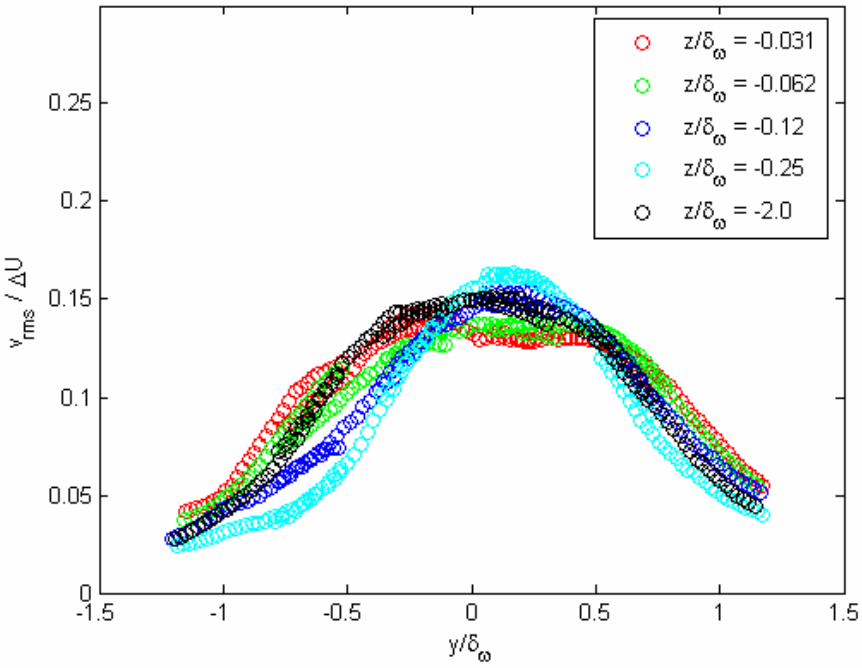

Figure 3.11: Normalized spanwise velocity fluctuations vs. depth, $x/\theta_i = 210$

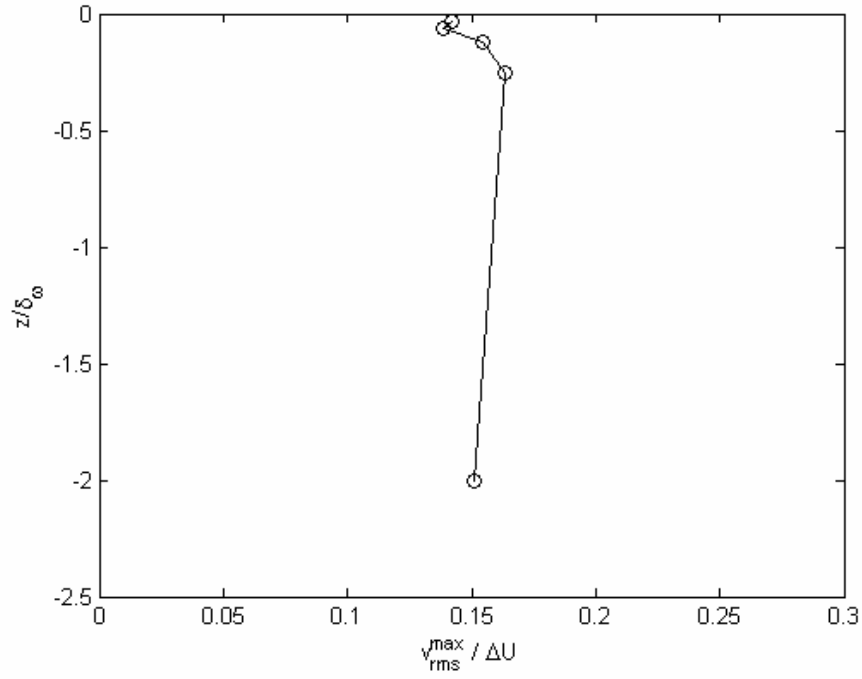

Figure 3.12: Maximum spanwise velocity fluctuation vs. depth, $x/\theta_i = 210$

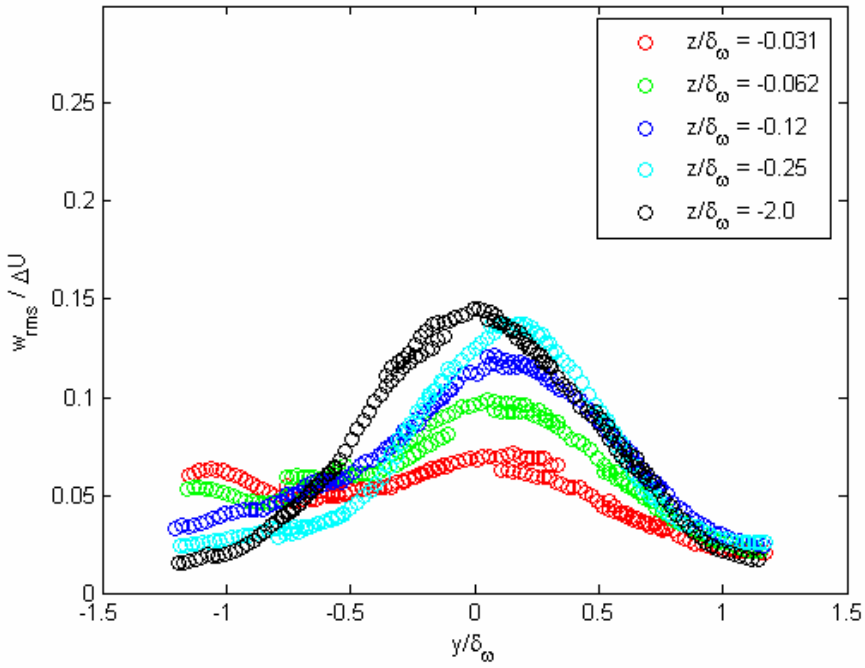

Figure 3.13: Normalized vertical velocity fluctuations vs. depth, $x/\theta_i = 210$

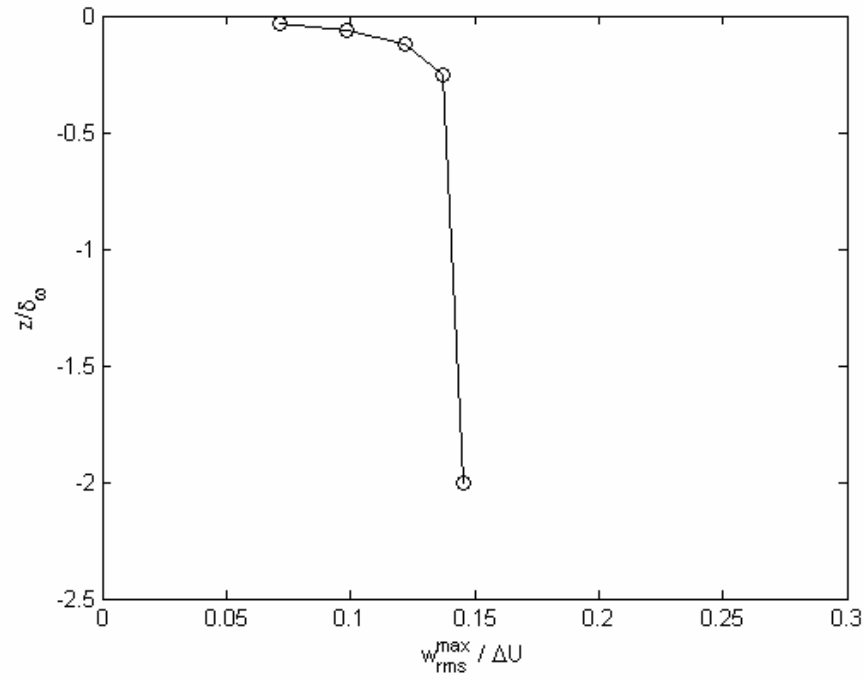

Figure 3.14: Maximum vertical velocity fluctuation vs. depth, $x/\theta_i = 210$

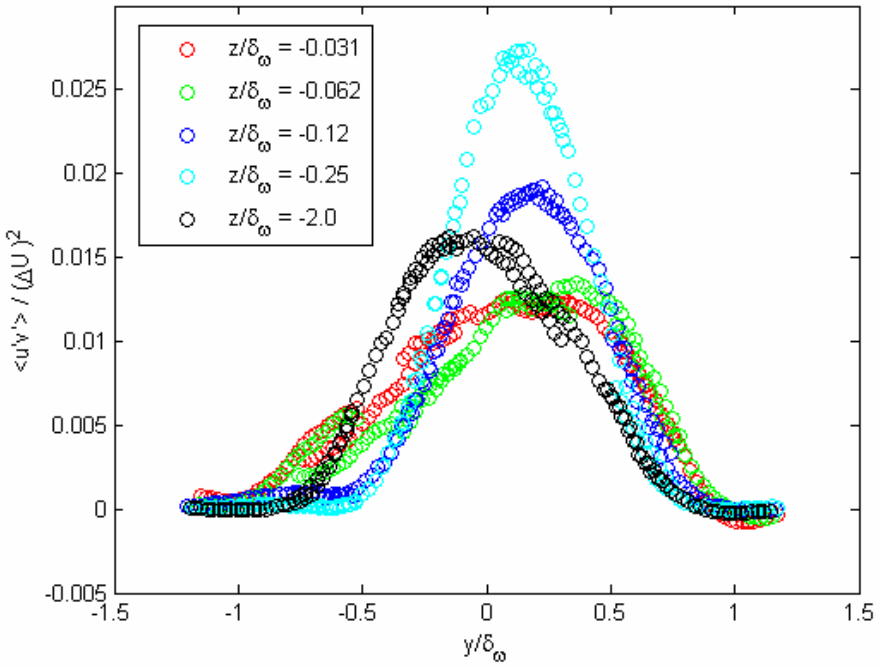

Figure 3.15: Normalized $\overline{u'v'}$ profiles vs. depth, $x/\theta_i = 210$

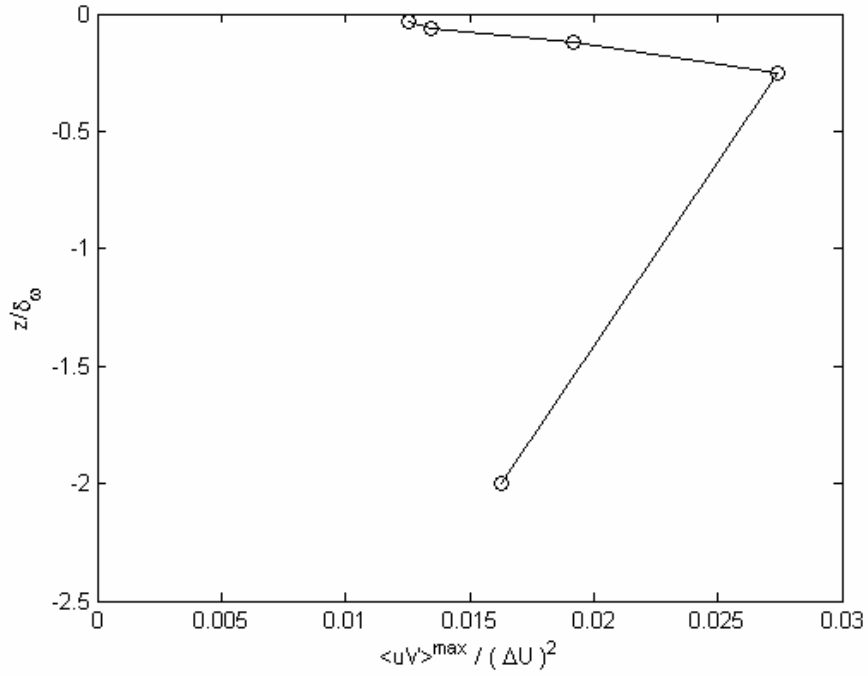

Figure 3.16: Maximum $\overline{u'v'}$ value vs. depth, $x/\theta_i = 210$

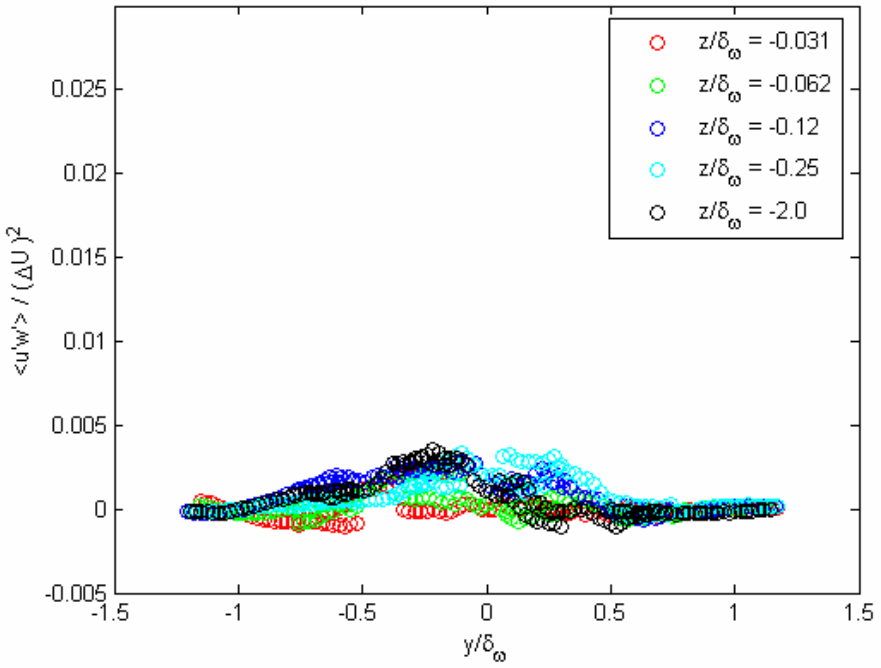

Figure 3.17: Normalized $\overline{u'w'}$ profiles vs. depth, $x/\theta_i = 210$

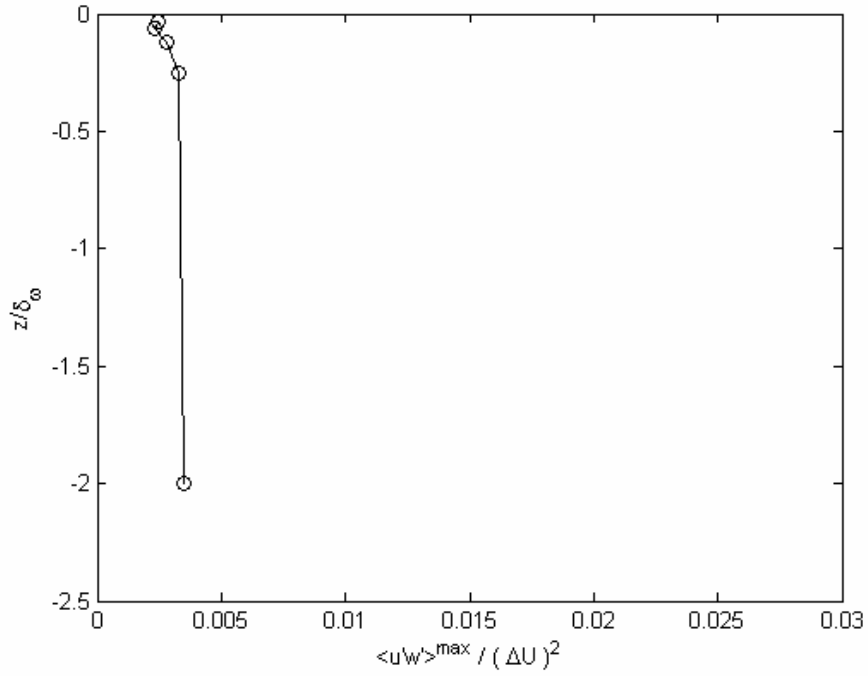

Figure 3.18: Maximum $\overline{u'w'}$ value vs. depth, $x/\theta_i = 210$

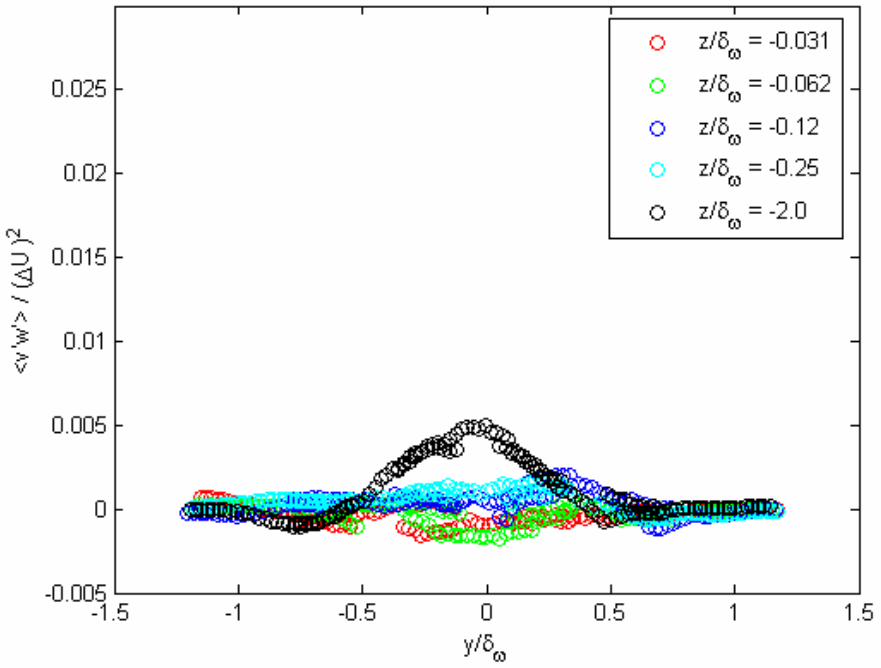

Figure 3.19: Normalized $\overline{v'w'}$ profiles vs. depth, $x/\theta_i = 210$

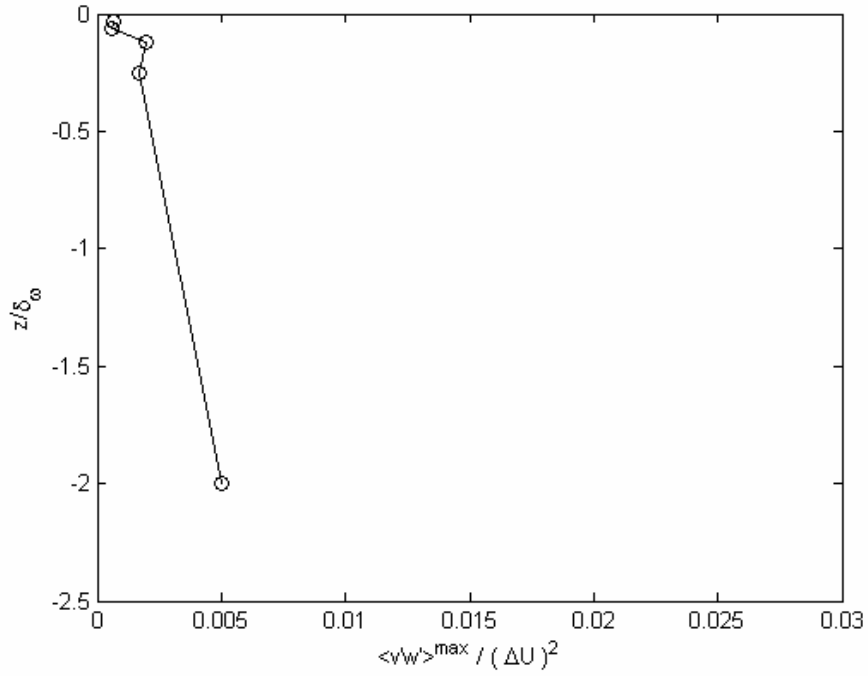

Figure 3.20: Maximum $\overline{v'w'}$ value vs. depth, $x/\theta_i = 210$

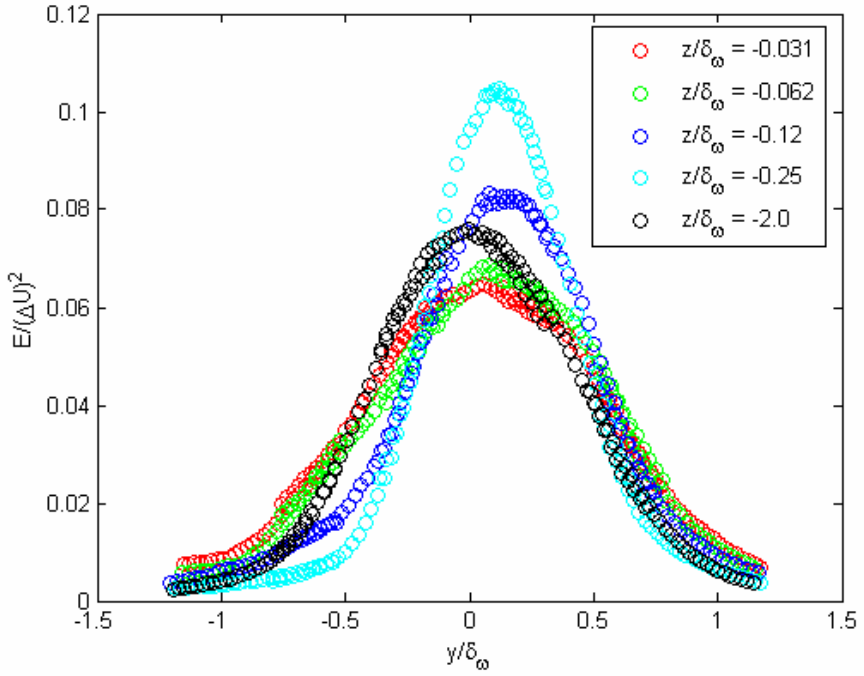

Figure 3.21: Normalized turbulence kinetic energy profiles vs. depth, $x/\theta_i = 210$

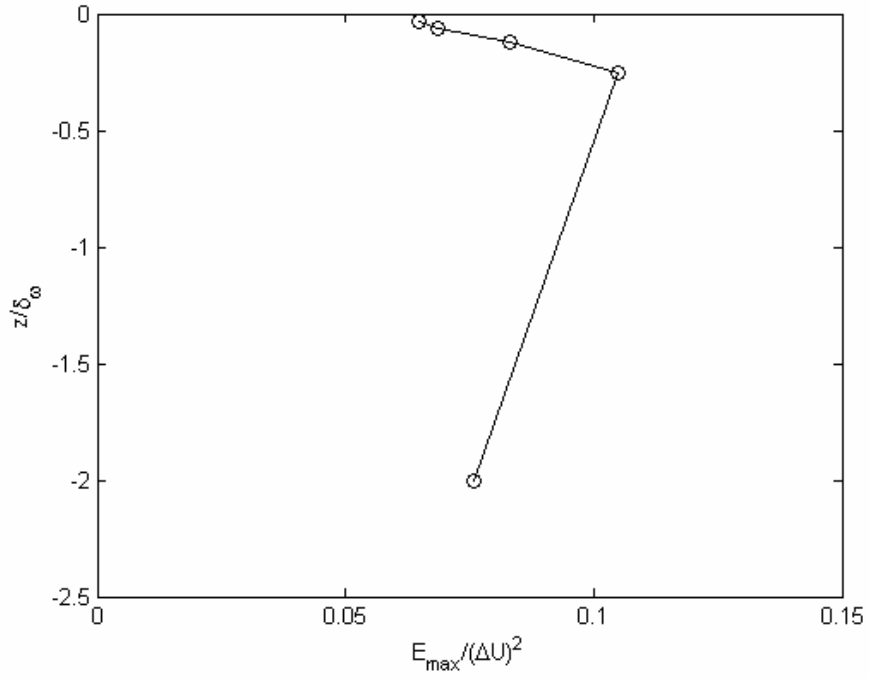

Figure 3.22: Maximum turbulence kinetic energy vs. depth, $x/\theta_i = 210$

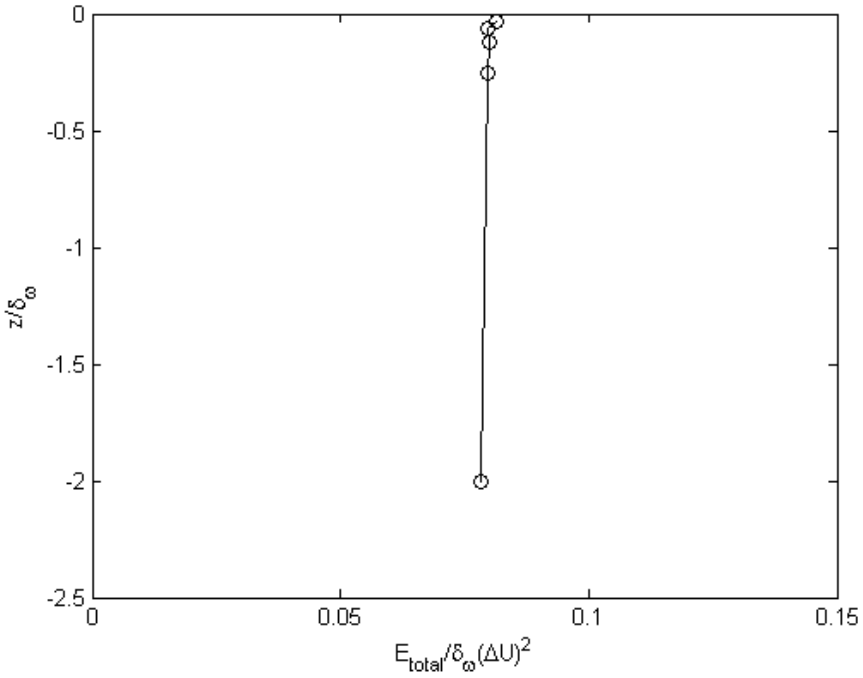

Figure 3.23: Total turbulence kinetic energy (integrated) vs. depth, $x/\theta_i = 210$

Chapter 4 Spectral Analysis

4.01 Temporal Spectra

(a) Overview

The nature of the SDPIV equipment (lasers, cameras, and image recording hardware) used in this experiment imposed a sampling rate of 15 Hz on the recorded data. This is clearly too low to resolve the finer scales of the turbulence in a single-point fashion analogous to that involving a hot-film anemeter, for example. However, frequencies of 7.5 Hz and below are easily examined by making use of long-time velocity histories.

As described previously, at every interrogation location SDPIV data was recorded for 6,000 images, or 3,000 pairs resulting in an instantaneous velocity field. As these fields are separated temporally by a uniform $\Delta t = 1/15\,\text{s}$, the total record length of the velocity profiles is 200 seconds. Recalling that the Kolmogorov dissipation length scale λ_k was previously estimated as 0.3 mm for this flow and that the structures in the flow are advecting through the interrogation region at approximately the convective velocity $U_C = 316\,\text{mm/sec}$, we note that $\lambda_k / U_C = 9.4 \times 10^{-4}\ \text{s}^{-1}$ and conclude that our resolution in these temporal spectra (the Nyquist frequency is 7.5 s^{-1}) falls several orders of magnitude short of that needed to capture the dissipation scales. The calculation of velocity and energy spectra in this fashion implicitly makes use of the Taylor hypothesis of frozen flow, as spectra defined in terms of wavenumbers (spatial frequencies) are computed in terms of temporal frequencies. Saddoughi & Veeravalli (1994) and others

indicate that this process is valid for flows in which the turbulence intensity is sufficiently low compared to the speed of the mean flow that

$$\frac{\sqrt{\overline{u'^2}}}{U_C} < 0.1.$$

Based on the data presented in the previous chapter we calculate the maximum value of $\sqrt{\overline{u'^2}}$ to be approximately 32 mm/s. The convective velocity $U_C = 316\,\text{mm/s}$ indicates that the condition above is thus (just) satisfied in the most active region of the flow, and is easily satisfied in the less active regions.

This three-component velocity profile is available at all locations within a given interrogation plane. Quantities such as in-plane vorticity may also be computed, a step which requires the use of some spatially adjacent data.

Single-point time histories of all three velocity components at $x/\theta_i = 210$ were extracted and examined spectrally. Of particular interest is the power spectral density (power spectra) of each of the three velocity components. Several different mathematical techniques are available for the calculation of this quantity: Used for this work is a routine native to the MATLAB (The MathWorks, Inc.) software environment. This routine produces PSD estimates using Welch's averaged periodogram technique. A separate but similar MATLAB routine was used to calculate cross-spectral densities and, from them, cospectra. Further mathematical details of this operation may be examined in Appendix C.

(b) Single Point Power Spectra

In this section select examples will be presented of component power spectra calculated by the method described above, using compiled time histories of the velocity data at each location. Of particular interest will be the isotropy (or lack thereof) of the turbulent motions as a function of depth.

Figures 4.1(a-e) present the three one-component power spectra obtained at various depths on the tunnel centerline ($y/\delta_\omega = 0$). The time frequency, *f*, has been normalized by the large-scale parameters of the mixing layer in the bulk, as have the power spectra $E(f)$. The solid blue line in all power spectrum plots in this chapter represents the slope of a $f^{-5/3}$ profile – this being the slope taken by each component of isotropic turbulence in the inertial subrange. The low-frequency features visible in this data will be addressed comprehensively in the following section; of particular note here is the extent to which the three power spectra of the individual components converge to approximately equal levels.

In the bulk flow data ($z/\delta_\omega = -2.0$) we see that the three curves become essentially coincident for $f\delta_\omega/\Delta U > 1$, and that all three profiles approximately follow a $-5/3$ power law at these higher frequencies. This tendency is still seen at $z/\delta_\omega = -0.25$, although the convergence takes place at perhaps double the frequency that it does in the bulk flow. The dramatic increase at this depth of the low frequency motions in the streamwise direction (*u*) will be discussed in the following section.

At $z/\delta_\omega = -0.12$ the convergence is delayed until a still higher frequency, and at $z/\delta_\omega = -0.062$ it only occurs, if at all, at the upper reaches of the available bandwidth. It

is also clear by this point that the power spectrum of the vertical fluctuations (*w*) is nearly flat, resembling white noise.

At the most shallow station examined, $z/\delta_\omega = -0.031$, the anisotropy is quite pronounced, as the vertical fluctuations appear highly damped. A comparison of this depth to the bulk flow for $f\delta_\omega/\Delta U > 1$ reveals that the spanwise component's spectrum remains approximately the same, while that of the streamwise component *u* is markedly eleveated (by a factor of roughly five). The vertical fluctuations are attenuated by a similar amount.

Figures 4.2(a-e) present the same sort of data, but at a spanwise station of $y/\delta_\omega = 0.75$, which is towards the low-speed freestream. What is seen is that the general observations made for the tunnel centerline also apply here. One distinction which merits attention is that here, as the free surface is approached from below, no notable increase is seen in the higher frequencies of the streamwise velocity component.

Figures 4.3(a-e) again present the same information, but this time as observed at $y/\delta_\omega = -0.75$, in the direction of the high-speed freestream. As before, essentially the same trends are to be observed. There is considerably more activity in the lower frequencies seen near the surface in all components, and this is believed to be caused by the nearly-steady surface wave proposed to exist in the near-surface region as discussed in Chapter 3.

It is interesting to note that at the peripheries of the mixing layer the overall level of streamwise fluctuations do not increase to nearly the extent that they do along the tunnel center, remaining along the edges more or less equal to the spanwise fluctuations in the upper frequencies examined in this section. What is clearly seen is what appears to

be the upper end of the inertial subrange (where the $-5/3$ profile is approximately followed) tending away from isotropy as the surface is approached from below. This is in general agreement with the results of Mangiavacchi *et al*. (1994) obtained in the study of a turbulent jet near a free surface.

(c) Power Spectra Compared across Domain

In this section power spectra of each of the three velocity components across the entire examined spanwise range and at all depths surveyed, will be presented for $x/\theta_i = 210$. The interest in this section is the characterization of the relatively low-frequency oscillations which influence the mean and secondary flows known to exist in the free surface layer (Maheo, 1998).

Power spectra such as those presented in the previous section were calculated not just for those spanwise stations shown there, but all the way across the measured area at a spacing of approximately 1 mm. At a given depth beneath the free surface, said power spectra may be presented as a contour plot in which the ordinate axis represents spanwise station (y/δ_ω) and the abscissa indicates frequency *f*; the contour color depicts the value of the power spectrum. This method of data presentation easily highlights spectral peaks that span all or part of the mixing layer; as shall be seen the extent of this span may vary considerably with depth.

The data displayed in this section are plotted linearly, rather than logarithmically, as the emphasis here is on the larger magnitude, low frequency oscillations. Such are made more clear in the plots if a linear color mapping is applied.

A spanwise smoothing algorithm was applied to the data as presented in this section, primarily to deal with some “sawtooth” patterns that occurred when overlapping data windows (recall that there are five slightly overlapping regions which were investigated individually) did not precisely match up. The algorithm used was the

Lowess smoothing method with a span of 11 stations, as implemented by the MATLAB routine *smooth.m*. This process did not materially alter the contours shown below, but did substantially improve their ease of interpretation.

Figures 4.4(a-c) show the power spectra of the individual components in the bulk flow ($z/\delta_\omega = -2.0$). Very clearly apparent in the streamwise (u) and spanwise (v) data is a strong peak at approximately $f\delta_\omega/\Delta U = 0.8$. This peak would appear to represent the dominant coherent structure in the form of vertically-oriented vortices. In real coordinates this frequency is f = 1.25 Hz, corresponding to a timescale $\tau = 1/f = 0.8$ s. We thus have

$$\frac{\tau U_C}{\delta_\omega} = 3.1,$$

where the convective velocity $U_C = \frac{1}{2}(U_1 + U_2) = 315.5$ mm/s. This is in reasonable agreement with the range of $3.1 < \tau U_C/\delta_\omega < 5.0$ reported by Dimotakis & Brown (1976), as well as some others referred to in that work: $\tau U_C/\delta_\omega \sim 3.8$ by Brown & Roshko (1974); and $\tau U_C/\delta_\omega \sim 3.3$ by Winant & Browand (1974). Dabiri (2003) performed experiments in the present facility, but at different speeds; the dominant frequency displayed in the power spectra produced in that work correspond approximately to $\tau U_C/\delta_\omega \sim 3.3$. The frequency we see such strong oscillations at in this data would thus appear to be approximately what one would expect as the dominant frequency of the coherent structures.

The peak is observed to be considerably wider in the v component than in u, and there are stronger images of smaller peaks at different (mostly lower) frequencies to be seen in the u data. The magnitude of the peak in both u and v is approximately $E(f)/(\delta_\omega \cdot \Delta U) = 0.04$. A significantly weaker and narrower peak at this same frequency may be seen in the vertical component of velocity, w; inspection of Figure 5.1(a), which contains the same data at $y/\delta_\omega = 0$, clarifies this difference in peak magnitude to a factor of roughly four.

Figures 4.5(a-c) show the same data at $z/\delta_\omega = -0.25$. While the vertical (*w*) spectrum still shows no strong peaks, there remains a visible (but much less intense and of less spanwise extent) peak at $f\delta_\omega/\Delta U = 0.8$. It should also be noted that the fluctuating activity in the *z* direction exists in a significantly narrower spanwise band at this depth than it does at $z/\delta_\omega = -2.0$. This same reduction in apparent width of the mixing layer is also seen in the *u* and *v* plots. Most notable, however, is the very strong peak in *u* seen at approximately $z/\delta_\omega = -0.25$. Having a magnitude near $y/\delta_\omega = 0$ of nearly $E(f)/(\delta_\omega \cdot \Delta U) = 0.1$ and a very narrow span, this peak dwarfs any other fluctuations described in this section. The origin of this peak, and the significance of the frequency, is not immediately clear and will be discussed subsequently. The *v* data contains a peak at this same frequency, but it is of considerably lower intensity. There is still activity visible at $f\delta_\omega/\Delta U = 0.8$, but compared to the data at depth it is considerably attenuated and much narrower.

Figures 4.6(a-c) show that this $f\delta_\omega/\Delta U = 0.5$ peak is still seen in the *u* and *v* data at a depth of $z/\delta_\omega = -0.12$, but the intensities are much less than those seen at $z/\delta_\omega = -0.25$. At this depth the $f\delta_\omega/\Delta U = 0.8$ and $f\delta_\omega/\Delta U = 0.5$ fluctuations in *u* are of nearly the same magnitude and lateral span, again peaking at approximately $E(f)/(\delta_\omega \cdot \Delta U) = 0.04$. Both peaks are quite visible in *v*, but are significantly lower in intensity; the $f\delta_\omega/\Delta U = 0.8$ peak, at the center of the mixing layer, is clearly stronger in this component than the $f\delta_\omega/\Delta U = 0.5$ one. As with all depths seen thus far, the *z* fluctuations show only a low-intensity peak at $f\delta_\omega/\Delta U = 0.8$ and nothing of any significance at $f\delta_\omega/\Delta U = 0.5$.

Moving up to depths $z/\delta_\omega = -0.062$ (Figures 4.7(a-c)) and $z/\delta_\omega = -0.031$ (Figures 4.8(a-c)), we see a general reduction in intensity of all peaks compared to their deeper counterparts. At $z/\delta_\omega = -0.031$ the vertical fluctuations have dropped nearly to zero, but a small peak is still visible across a fairly broad span at $f\delta_\omega/\Delta U = 0.8$. The streamwise fluctuations are very similar between these two near-surface depths, and we still see

moderate peaks at both normalized frequencies 0.5 and 0.8. Similar behavior is observed in the spanwise fluctuations, but as the surface is approached there appears to be a concentration of the $f\delta_\omega/\Delta U = 0.5$ fluctuation into two lobes around the tunnel centerline. This bimodal spanwise intensity distribution is not seen in the $f\delta_\omega/\Delta U = 0.8$ fluctuation in *v*.

(d) Single Point Cospectra

In a manner nearly identical to that used to obtain the power spectra of each individual velocity component, the cross-spectral densities (CSD) of each combination of components may be obtained. In this section the cospectra, defined as the real part of the CSD and referred to as C_{ab} for arbitrary quantities *a* and *b*, are presented at the same locations as the power spectra shown in section (b). The absolute values of the cospectra, which may change sign, are presented in this chapter.

Wyngaard & Coté (1972) demonstrate that in isotropic turbulence absent a mean shear all three cospectra will vanish. However, in the presence of some mean shear such as the large $\partial U/\partial y$ values extant in the mixing layer under current study, the corresponding cospectrum $C_{u'v'}$ will be nonzero, and will decay in the frequency domain according to an $f^{-7/3}$ power law.

Figures 4.9(a-e) show the calculated cospectra of the three combinations of velocity components along the tunnel centerline, $y/\delta_\omega = 0$. The relative values of the profiles in the higher frequency range do not appear to change significantly with depth, although some clear differences are visible in the lower frequencies – specifically the two at which peaks were noted in the previous section. Discussion of this topic will be deferred to the following section. What is noteworthy is the greater magnitude of $C_{u'v'}$

compared to the other two components throughout the higher frequencies and at all depths shown.

Figures 4.10(a-e) present the same variety of data, but at a spanwise station of $y/\delta_\omega = 0.75$, which is towards the low-speed freestream. The general trends seen at $y/\delta_\omega = 0$ are also extant here, but the magnitudes are somewhat lower, and the peaks in the lower frequency ranges are much less distinct if they are seen at all.

Figures 4.11(a-e) again present the same information, but this time as observed at $y/\delta_\omega = -0.75$, in the direction of the high-speed freestream. These profiles are of still lower overall magnitude than those taken on the far side of the mixing layer. At the greater depths we observe that the profiles are all of approximately the same magnitude, while as the free surface is approached ($z/\delta_\omega \geq -0.062$) the $C_{u'v'}$ values are seen to rise in the higher frequencies by a factor of about three. The remaining cospectra seem to maintain approximately the same values as they had at depth.

(e) Cospectra Compared Across Domain

Figures 4.12(a-c) present the cospectra of the three combinations of velocity components in much the same fashion as seen in the section (c). For clarity, the colorbars are not identical; that for $C_{u'v'}$ goes a factor of two higher than that for the other three. This scheme is used for all plots presented in this section. In all three plots a strong peak at a frequency of approximately $f\delta_\omega/\Delta U = 0.8$ is clearly seen – much wider and more intense in *u'v'*, but clearly visible in all cases. Of interest is the spanwise placement; the apparent peak value of intensity occurs some $0.1\delta_\omega$ towards the high-speed freestream

relative to the tunnel centerline. Recall that the mixing layer as a whole, even at this depth, has been observed to have deflected towards the low-speed side.

At $z/\delta_\omega = -0.25$ (Figures 4.13(a-c)), we see nearly no energy in the cospectra of *u'w'* and *v'w'*, but extremely strong correlation in *u'v'*. This strong $C_{u'v'}$ peak occurs most intensely at approximately $f\delta_\omega/\Delta U = 0.5$, which was seen to be a dominant mode in the power spectra at this depth, but there is also a smaller peak (and of lesser spanwise extent) at about $f\delta_\omega/\Delta U = 0.8$. Contrasting considerably with the deep data just presented, these peaks appear to be offset from the tunnel centerline in the positive *y* direction.

Figures 4.14(a-c) show the same data at $z/\delta_\omega = -0.12$; we again see little correlation in the form of strong peaks in the *u'w'* and *v'w'* cospectra. There are at this depth two distinct peaks in the *u'v'* cospectra, much like those seen at $z/\delta_\omega = -0.25$. These two are of approximately equal peak value, but each peak is offset laterally by a different amount; the $f\delta_\omega/\Delta U = 0.5$ peak is biased towards the low-speed side by approximately $0.1\delta_\omega$ more than the similarly shaped peak at $f\delta_\omega/\Delta U = 0.8$.

At $z/\delta_\omega = -0.062$ (Figures 4.15(a-c), we again observe no strong cospectrum peaks in *u'w'* and *v'w'*. While there is a visible increase in *u'v'* intensity at $f\delta_\omega/\Delta U = 0.8$, the only sizeable peak in that plot is seen at $f\delta_\omega/\Delta U = 0.5$; this peak is offset towards the high-speed side of the mixing layer by even more than the one seen at $z/\delta_\omega = -0.12$.

Figures 4.16(a-c) show this data at a the shallowest position, $z/\delta_\omega = -0.031$. Again we see little of interest in the *u'w'* and *v'w'* plots, but there remain at this depth peaks at $f\delta_\omega/\Delta U = 0.5$ and $f\delta_\omega/\Delta U = 0.8$ in the *u'v'* cospectrum. Both are rather weak, by

comparison to those seen at greater depths, and the most dominant one is at the lower frequency. The $f\delta_\omega/\Delta U = 0.5$ peak, in particular, is offset a great deal towards the low-speed side of the tunnel – to an extent greater than any others seen.

(f) Combining Temporal and Spatial Power Spectra

In addition to the purely temporal spectral results presented thus far (with their maximum frequency of 7.5 s^{-1}), it is possible to make use of the Taylor hypothesis to convert *spatial* spectral results into temporal for direct comparison, and for extension of the available dynamic range. Recall that 3,000 velocity fields were obtained at each measurement station, each spanning approximately 11 cm in the streamwise direction. Given that the mean flow at each location is dominated by the streamwise component *U*, it is possible to convert this spatial data along the *x*-axis into temporal data with a considerably higher Nyquist frequency than that available from the purely temporal data shown previously. As was discussed earlier in this chapter, the Taylor hypothesis is expected to be valid based on the relative magnitudes of the velocity fluctuations and their mean values. Details of the mathematics are given in Appendix C.

Figures 4.17(a-e) display the calculated in this manner three one-component power spectra calculated in this manner at various depths on the tunnel centerline ($y/\delta_\omega = 0$). These figures are analogous to Figures 4.1(a-e), and in fact contain that same data; the difference is the addition of the higher-frequency information. It is essential to point out that no "correction factors" of any kind were used to force agreement between the spatial and temporal data in the region of overlap.

Figures 4.18(a-e) display data of this sort as calculated at a spanwise station of $y/\delta_\omega = 0.75$, which is towards the low-speed freestream. The main item to note by

comparison of these plots with their counterparts in Figure 4.17 is that the "matching" between the spatial and temporal spectra at the frequencies at which they overlap remains fairly good, even though the magnitude of the spectra is in some cases different by an order of magnitude between the mixing layer centerline and the periphery.

(g) Three-Component Energy Spectra

The ability of the SDPIV system to simultaneously extract all three components of velocity gives the ability to calculate full three-component energy spectra. At any point of interest within the measurement area, a time history not just of the individual velocity components, but of the total turbulence kinetic energy E_{tot} may be calculated:

$$E_{tot}(t) = \sqrt{u'^2(t) + v'^2(t) + w'^2(t)},$$

after which the power spectral density of E_{tot} may be calculated in an identical fashion to that used for the individual velocity components. The normalized contour plots (analogous to Figures 4.4-4.8) of the energy spectrum as it varies with depth are shown in Figures 4.19(a-e).

The overall impression given by these plots is essentially the same as those given by those presented so far. Very intense activity at $z/\delta_\omega = -0.25$ compared to any other depths, and a distribution of activity among frequencies similar to that seen previously. A considerably more pronounced bimodal distribution of energy is seen across the span of the mixing layer than has been observed in any of individual component power spectra.

4.02 Comments

Perhaps the most interesting (or surprising) result presented in this chapter is the very strong $f\delta_\omega/\Delta U = 0.5$ peak in the streamwise power spectrum at $z/\delta_\omega = -0.25$, as well as the considerably smaller peaks in other components at that frequency. This in particular bears further examination.

The various fluctuations at that frequency are consistent with a slow transverse oscillation of the mean flow pattern. The mean streamwise velocity profile $U(y)$ has a very high gradient near the center of the mixing layer, so even a slight transverse periodic motion of the mean profile will result in quite large differences in U at a given point within the mixing layer – and thus a strong peak in the streamwise power spectrum. The relative magnitudes of the mean spanwise and vertical velocities are much less, so the considerably lower peaks in their respective power spectra are unsurprising.

The difference in the magnitude of the streamwise spectral peak as the depth is varied is interesting. As pointed out above, one of the contributing factors in the peak's size at a give location in an oscillating mean flow would be the slope of the $U(y)$ profile, which we have observed changes somewhat with depth.

This change is not enough to explain the differences in peak height with depth, however: At $z/\delta_\omega = -0.25$ the maximum slope of the $U(y)$ profile was measured to be 2.3 s^{-1}, while at $z/\delta_\omega = -0.12$ that slope is 1.9 s^{-1} – a ratio of approximately 1.2. However, the magnitudes of the spectral peaks at $f\delta_\omega/\Delta U = 0.5$ for those depths have a ratio of approximately 2.2. This disparity between maximum $U(y)$ gradient and peak height becomes even greater as the free surface is approached.

It is hypothesized on this basis that the transverse oscillation taking place near the free surface has a magnitude that strongly varies with depth. We also note that the maximum apparent amplitude of this oscillation is at the depth which Maheo showed to be approximately that at which two streamwise counter-rotating vortices appear in the mean flow.

Given that such vortices also have been shown to appear in the wakes of surface ships, and that towed ship model wakes have been observed to meander (Shen, *et al.*, 2002), a potential connection is clear. It has also been shown that a pair of counter-rotating vortices may exhibit instability, and that the wavelengths at which the instability is most amplified have been characterized (*e.g.*, Crow, 1970).

In the case under study here, the frequency of the oscillation as it advects by the measurement station at x = 1000 mm is approximately 0.8 s^{-1}. Taken into account with the convective speed noted in Chapter 3 of $U_C = 316$ mm/s, we may conclude from this that the streamwise wavelength of the oscillation is approximately 250 mm.

According to the data of Maheo, at x = 1000 mm under these flow conditions the two streamwise vortices just under the surface in mean flow possess a core diameter to separation distance ratio (b/d) of approximately 0.35. The work of Widnall (1975) suggests that the most unstable wavelength for such a vortex pair would be approximately 650 mm ($\lambda/b \sim 6.5$).

This is considerably larger than the apparent wavelength observed here, but it must also be taken into account that 650 mm is of the order of the downstream distance at which measurements are being taken. The mixing layer has been shown to grow more or less linearly with x, and the data of Maheo demonstrates that the spacing between the

persistent vortices also grows at approximately the same rate. It is thus rather questionable whether that simplified analysis, based on vortices which are parallel over distances comparable to the unstable wavelengths, should be given great credence.

The work of Shen *et al.*, mentioned briefly above, merits additional comparison to the present results. Their subject of study was of towed model ship wakes of varying beam/draft ratios; they combined experiments, numerical simulations, and an Orr-Sommerfeld stability analysis to reach their conclusions. Working at a Reynolds number based on ship beam of approximately 1,000, they found a fairly well-defined wavelength L_m for the meander in the model wakes to be approximately four times the beam b:

$$L_m \sim 4b .$$

Their experiments showed this parameter to be relatively insensitive to variations in beam/draft ratio.

The closest analog in the flow studied in this thesis to a beam is the only lateral lengthscale present, δ_ω. The wavelength of the oscillation in the present experiment, as noted above, is approximately triple the vorticity thickness:

$$\lambda = 3.1\delta_\omega .$$

This is similar to the wavelength of Shen *et al.*, but the phenomena are somewhat different and, more importantly, the observed behavior of the meandering diverge sharply in one respect. Shen *et al.* report, both in experiments and numerical simulations, the amplitude of the oscillation to be at its peak near the free surface, and to monotonically decrease with depth. In the present work, on the other hand, the amplitude of the oscillation has a very pronounced peak value at some distance beneath the free surface, and decreases as the surface is approached from below.

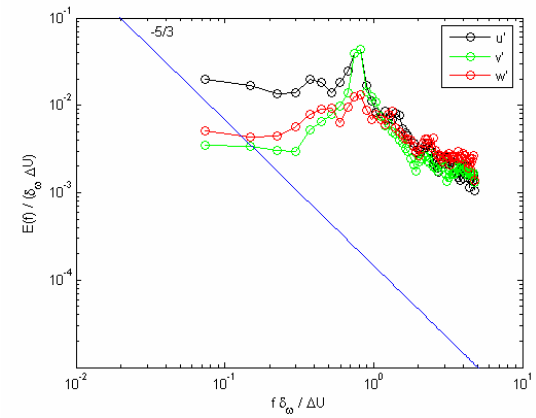

(a): $z/\delta_\omega = -2.0$

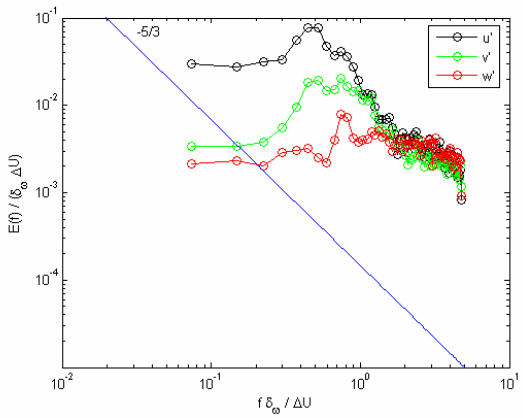

(b): $z/\delta_\omega = -0.25$

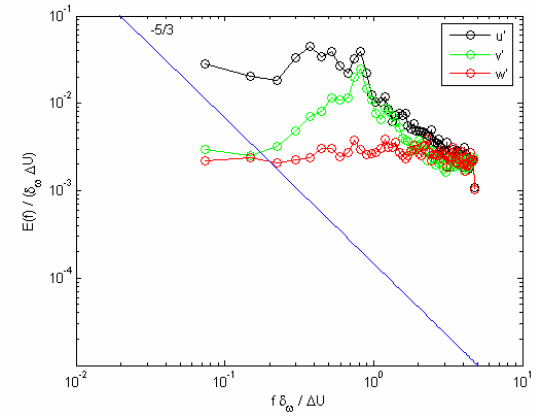

(c): $z/\delta_\omega = -0.12$

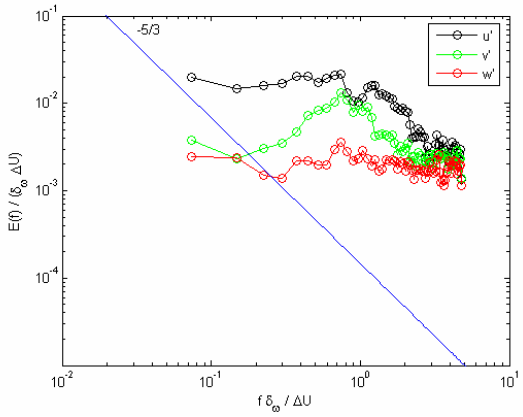

(d): $z/\delta_\omega = -0.062$

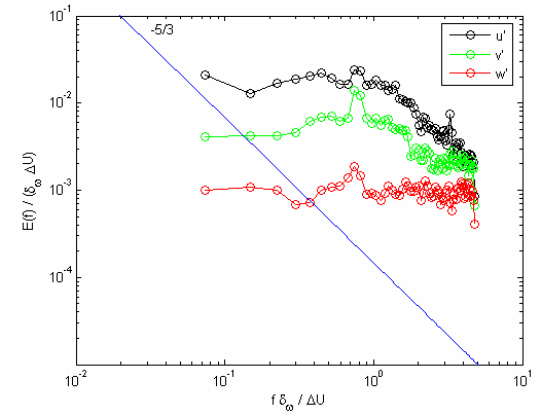

(e): $z/\delta_\omega = -0.031$

Figure 4.1: Normalized one-component power spectra, $x/\theta_i = 210$, $y/\delta_\omega = 0$

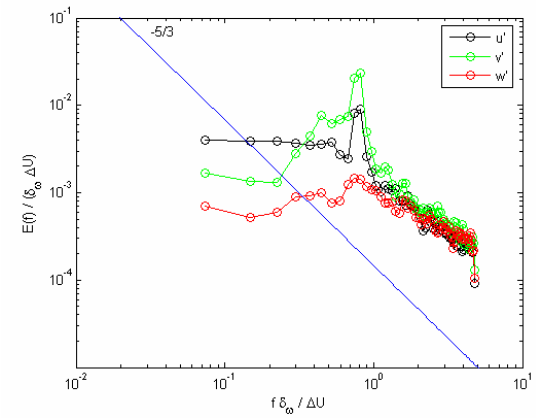

(a): $z/\delta_\omega = -2.0$

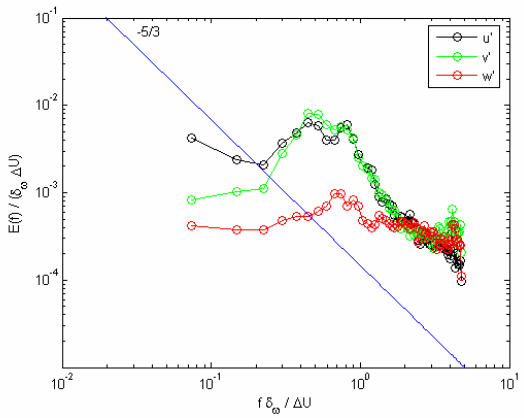

(b): $z/\delta_\omega = -0.25$

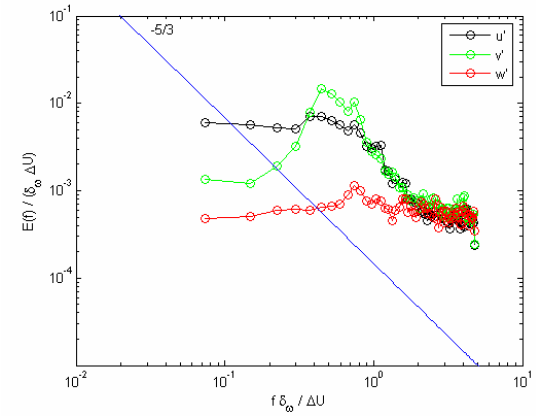

(c): $z/\delta_\omega = -0.12$

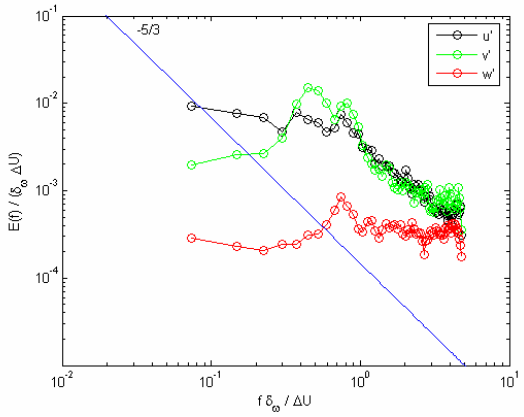

(d): $z/\delta_\omega = -0.062$

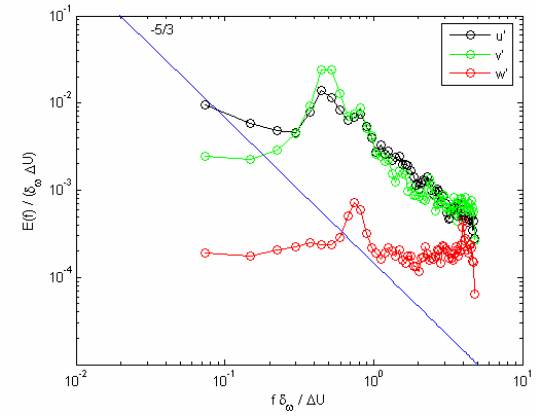

(e): $z/\delta_\omega = -0.031$

Figure 4.2: Normalized one-component power spectra, $x/\theta_i = 210$, $y/\delta_\omega = 0.75$

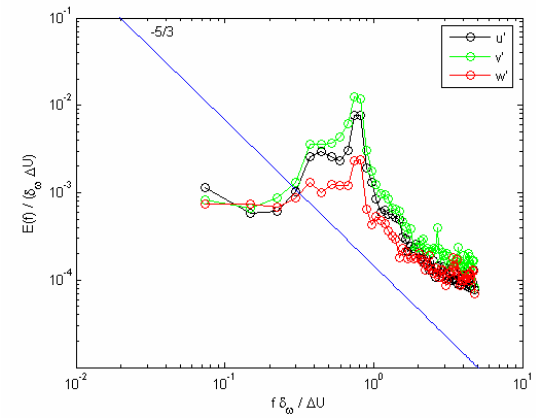

(a): $z / \delta_\omega = -2.0$

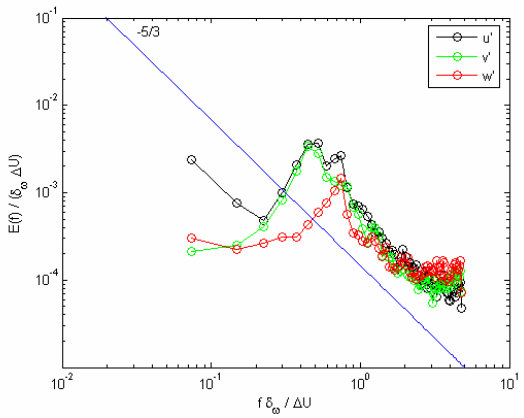

(b): $z / \delta_\omega = -0.25$

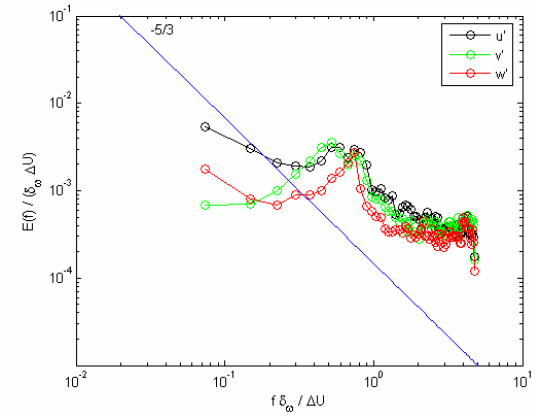

(c): $z / \delta_\omega = -0.12$

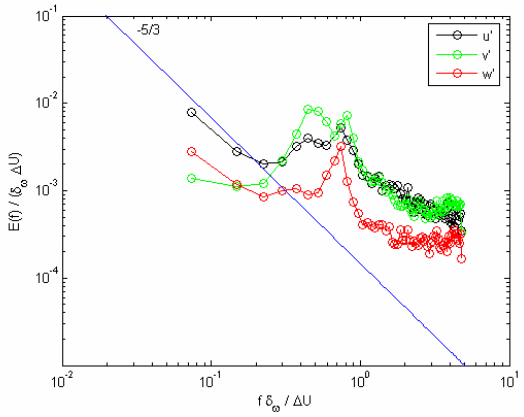

(d): $z / \delta_\omega = -0.062$

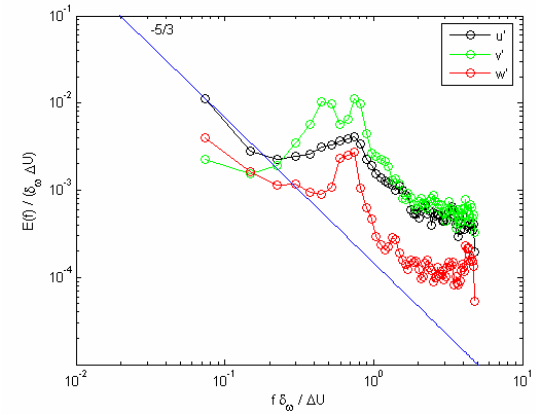

(e): $z / \delta_\omega = -0.031$

Figure 4.3: Normalized one-component power spectra, $x/\theta_i = 210$, $y/\delta_\omega = -0.75$

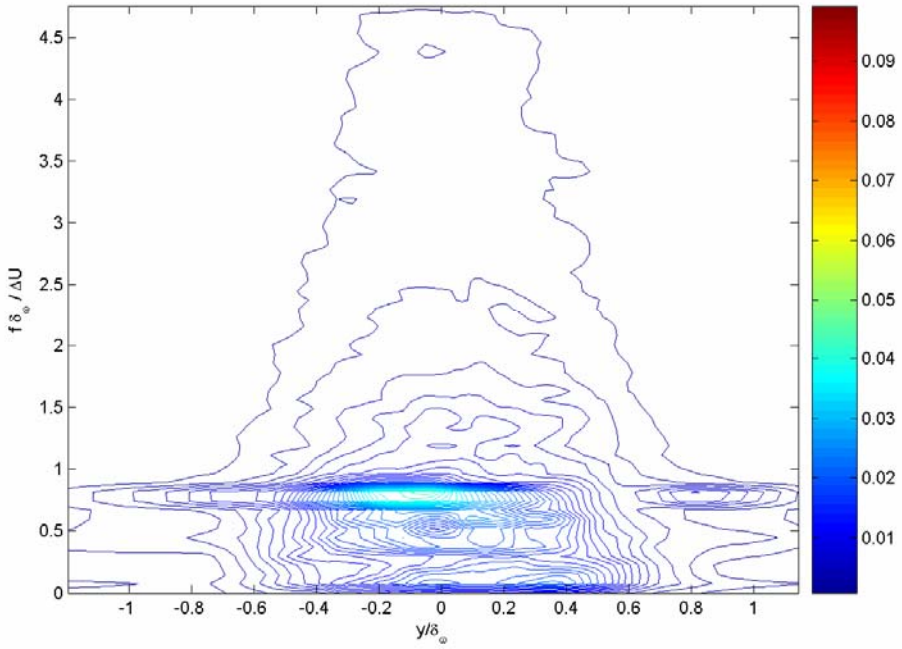

4.4(a): Streamwise power spectrum $E_u(f)/(\delta_\omega \cdot \Delta U)$

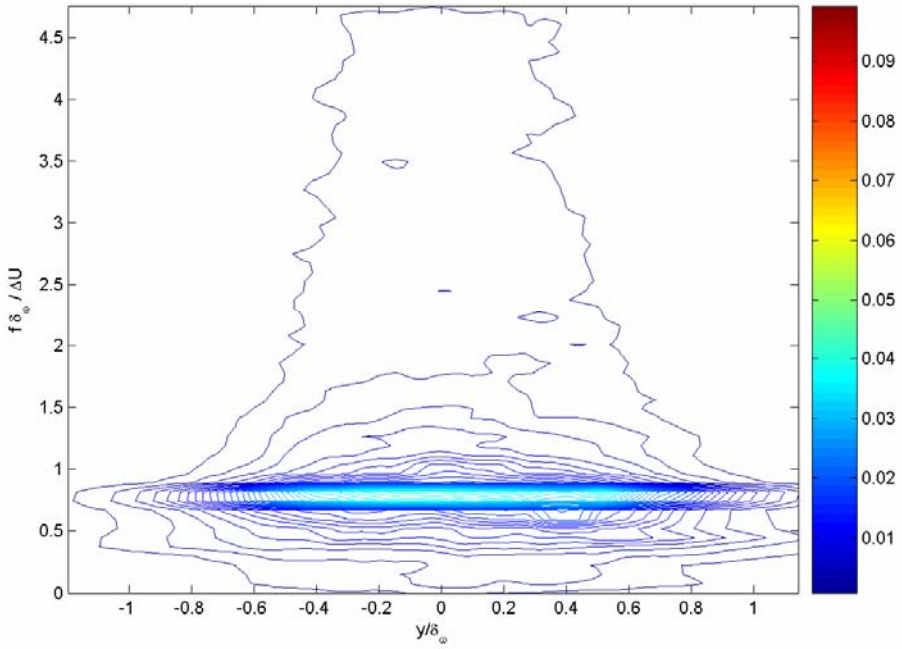

4.4(b): Spanwise power spectrum $E_v(f)/(\delta_\omega \cdot \Delta U)$

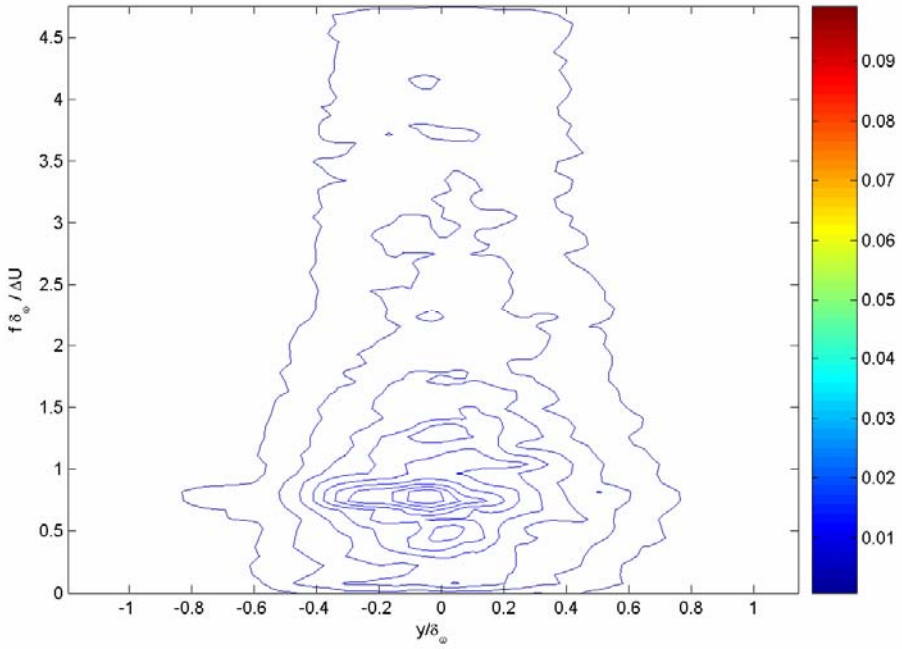

4.4(c): Vertical power spectrum $E_w(f)/(\delta_\omega \cdot \Delta U)$

Figure 4.4: Normalized one-component power spectra, x/θ_i = 210, z/δ_ω = -2.0

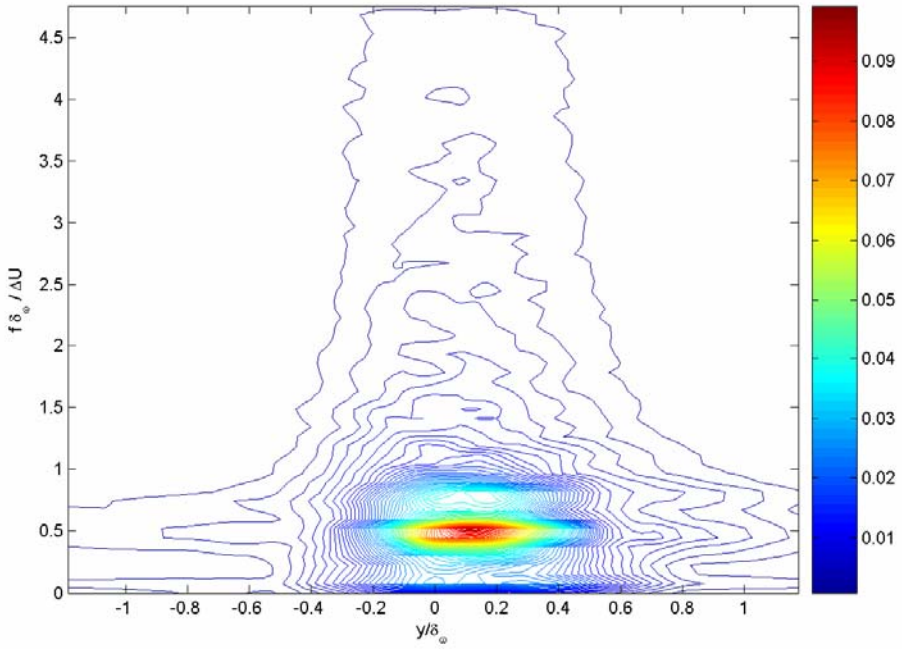

4.5(a): Streamwise power spectrum $E_u(f)/(\delta_\omega \cdot \Delta U)$

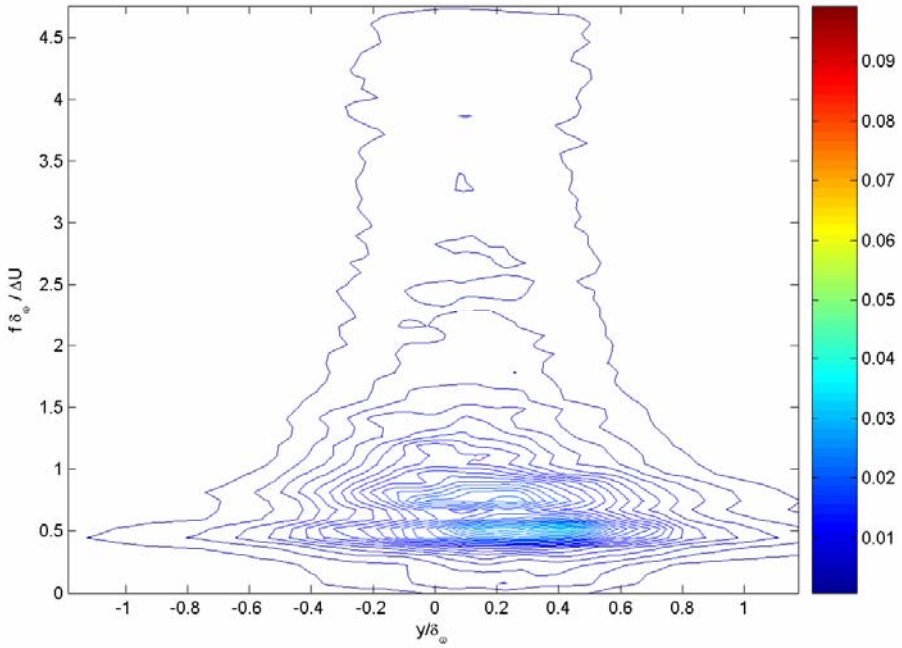

4.5(b): Spanwise power spectrum $E_v(f)/(\delta_\omega \cdot \Delta U)$

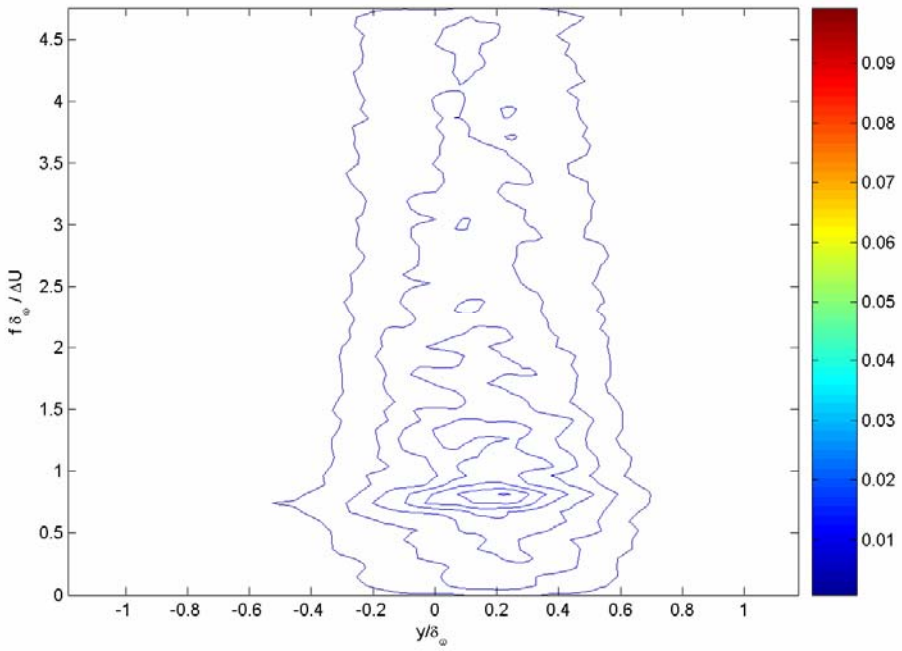

4.5(c): Vertical power spectrum $E_w(f)/(\delta_\omega \cdot \Delta U)$

Figure 4.5: Normalized one-component power spectra, x/θ_i = 210, z/δ_ω = -0.25

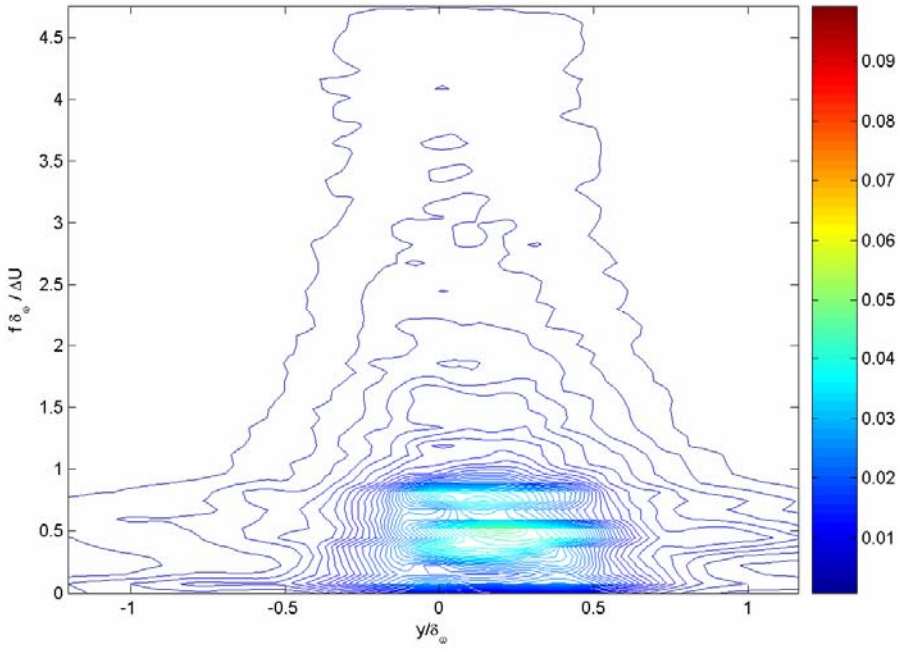

4.6(a): Streamwise power spectrum $E_u(f)/(\delta_\omega \cdot \Delta U)$

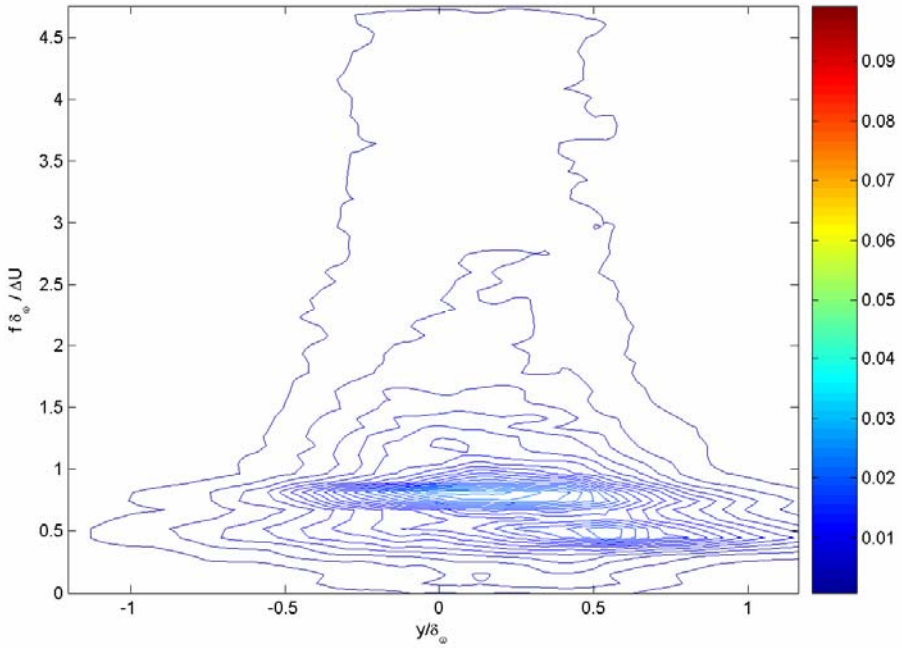

4.6(b): Spanwise power spectrum $E_v(f)/(\delta_\omega \cdot \Delta U)$

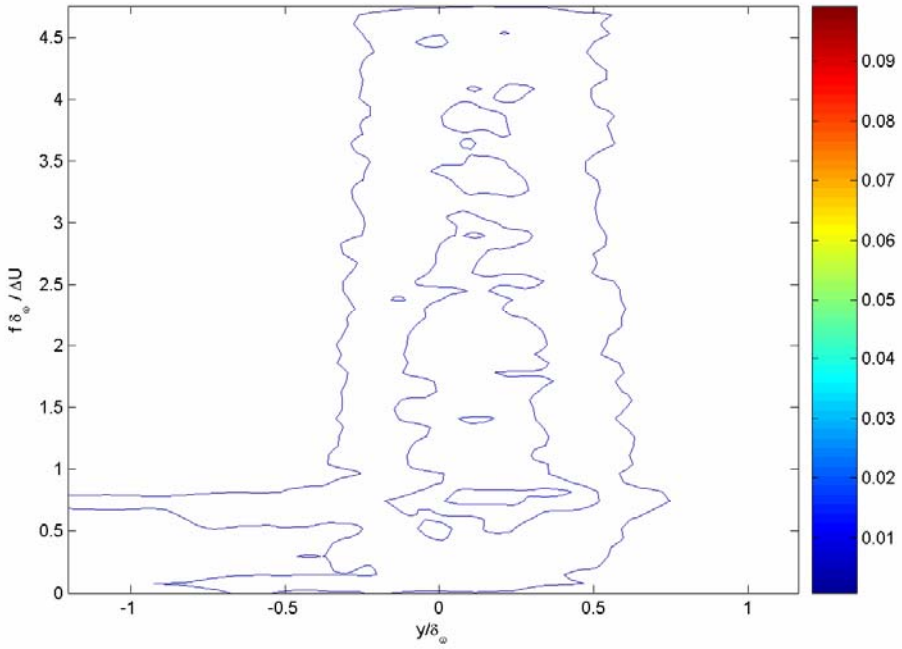

4.6(c): Vertical power spectrum $E_w(f)/(\delta_\omega \cdot \Delta U)$

Figure 4.6: Normalized one-component power spectra, x/θ_i = 210, z/δ_ω = -0.012

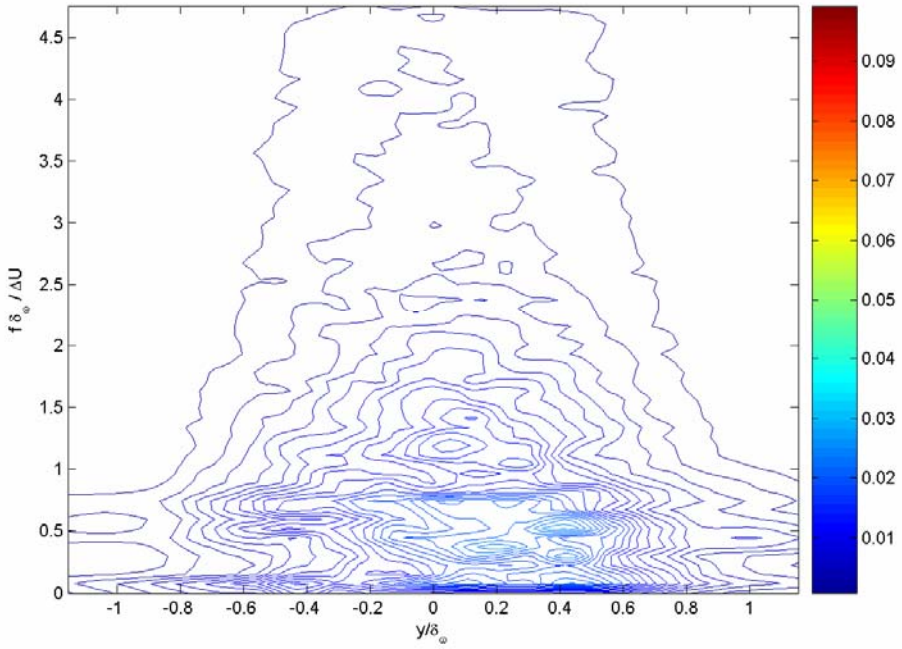

4.7(a): Streamwise power spectrum $E_u(f)/(\delta_\omega \cdot \Delta U)$

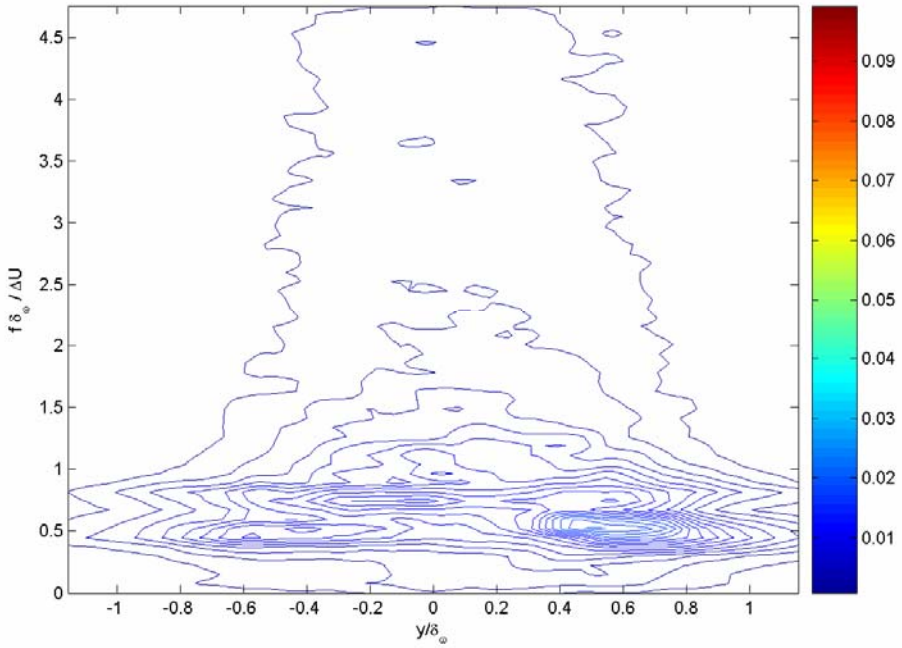

4.7(b): Spanwise power spectrum $E_v(f)/(\delta_\omega \cdot \Delta U)$

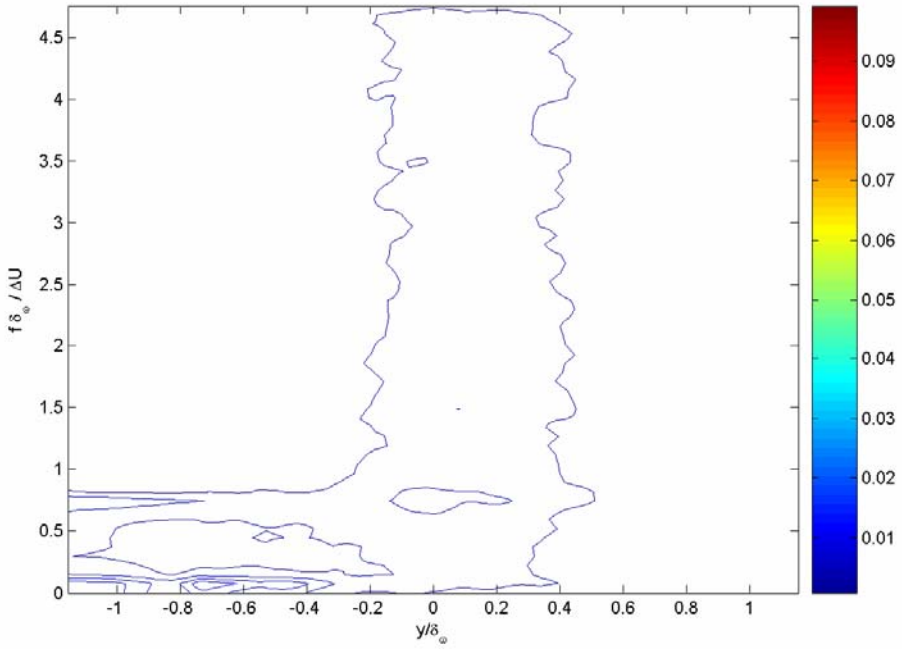

4.7(c): Vertical power spectrum $E_w(f)/(\delta_\omega \cdot \Delta U)$

Figure 4.7: Normalized one-component power spectra, x/θ_i = 210, z/δ_ω = -0.062

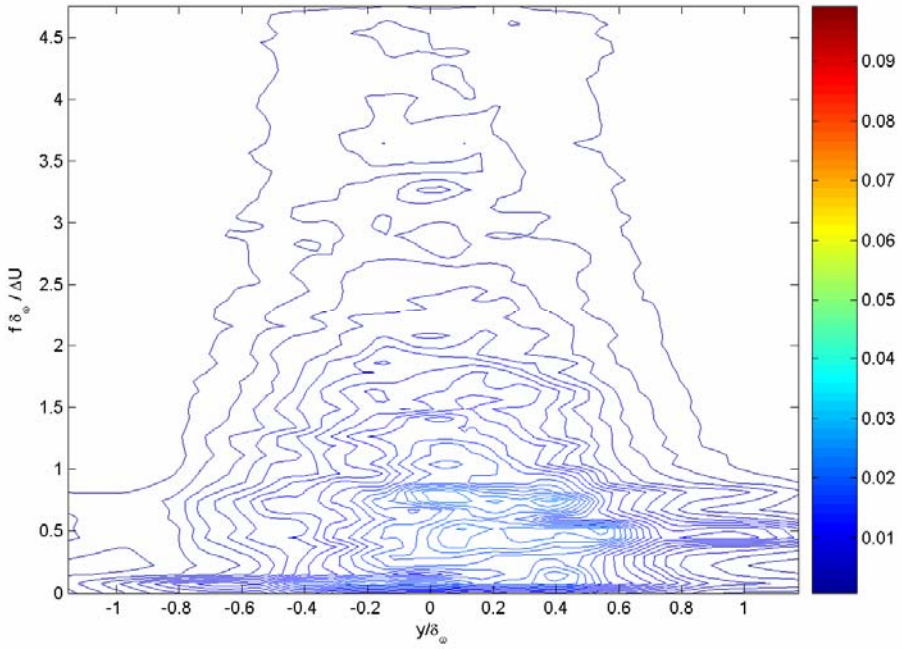

4.8(a): Streamwise power spectrum $E_u(f)/(\delta_\omega \cdot \Delta U)$

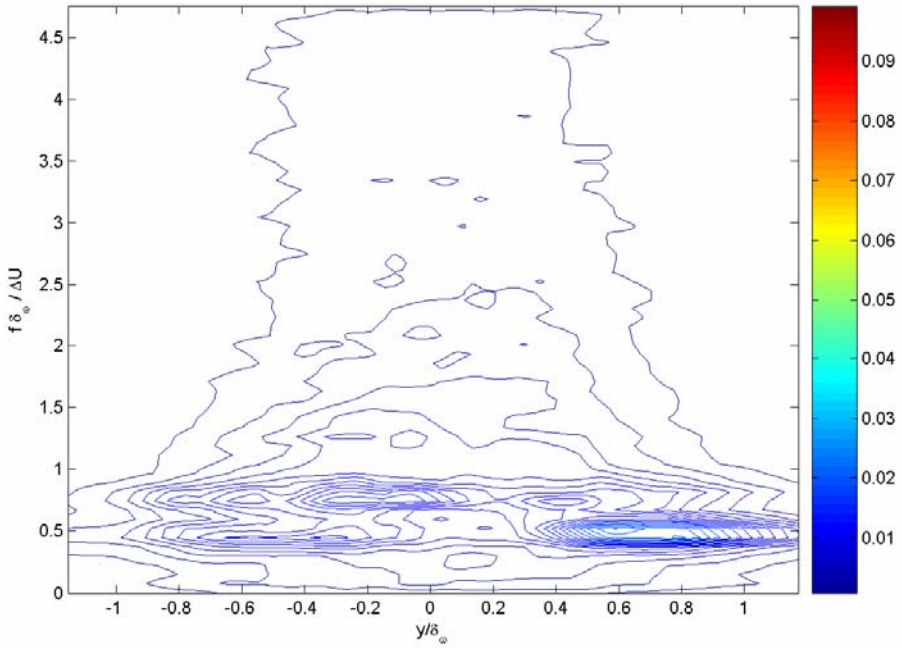

4.8(b): Spanwise power spectrum $E_v(f)/(\delta_\omega \cdot \Delta U)$

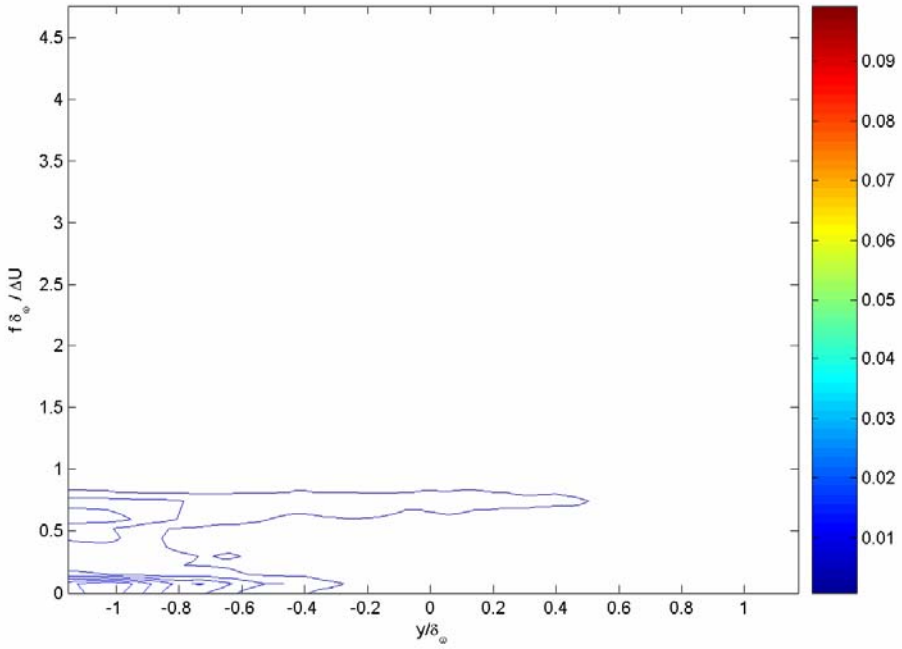

4.8(c): Vertical power spectrum $E_w(f)/(\delta_\omega \cdot \Delta U)$

Figure 4.8: Normalized one-component power spectra, x/θ_i = 210, z/δ_ω = -0.031

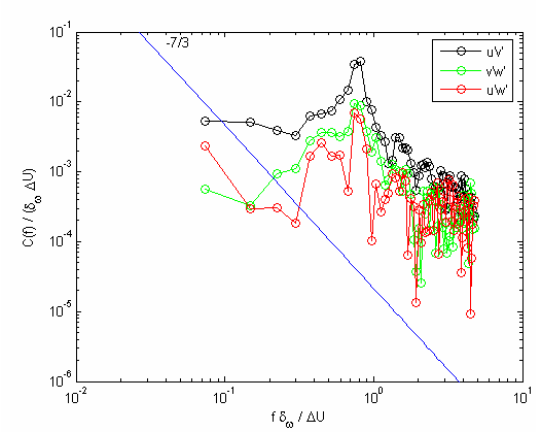

(a): $z / \delta_\omega = -2.0$

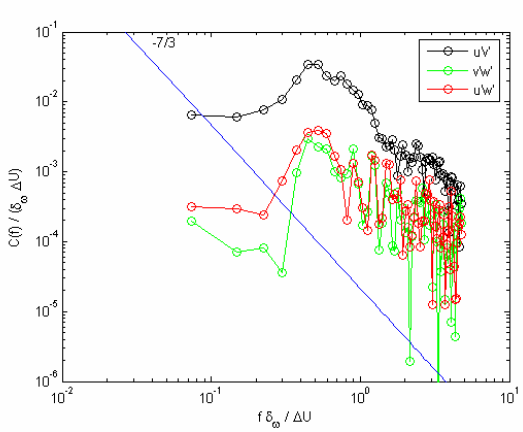

(b): $z / \delta_\omega = -0.25$

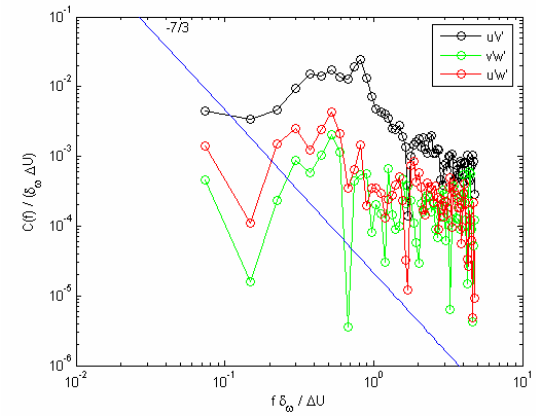

(c): $z / \delta_\omega = -0.12$

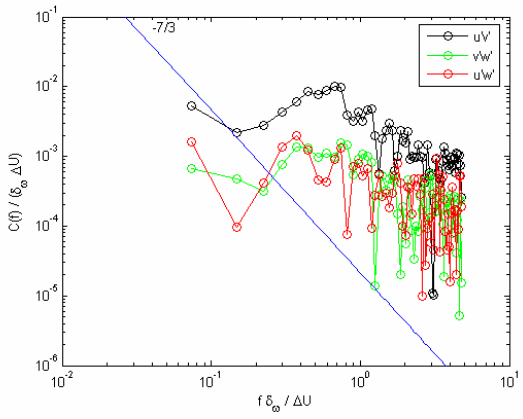

(d): $z / \delta_\omega = -0.062$

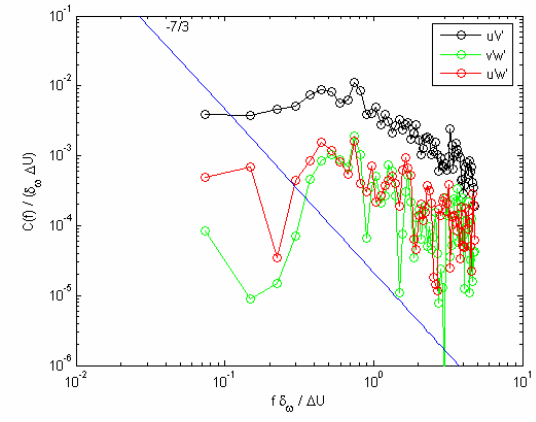

(e): $z / \delta_\omega = -0.031$

Figure 4.9: Normalized cospectra, $x/\theta_i = 210$, $y/\delta_\omega = 0$

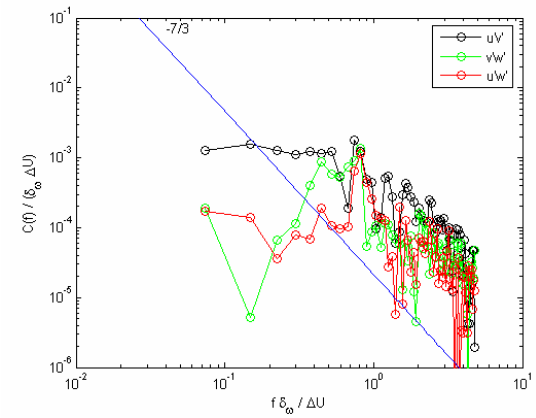

(a): $z / \delta_\omega = -2.0$

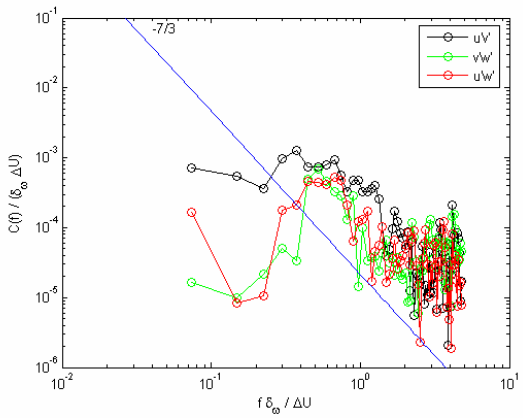

(b): $z / \delta_\omega = -0.25$

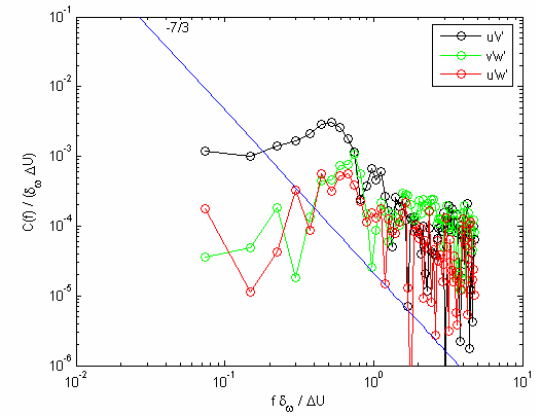

(c): $z / \delta_\omega = -0.12$

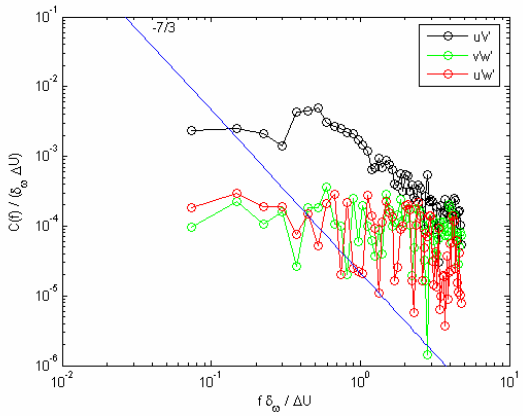

(d): $z / \delta_\omega = -0.062$

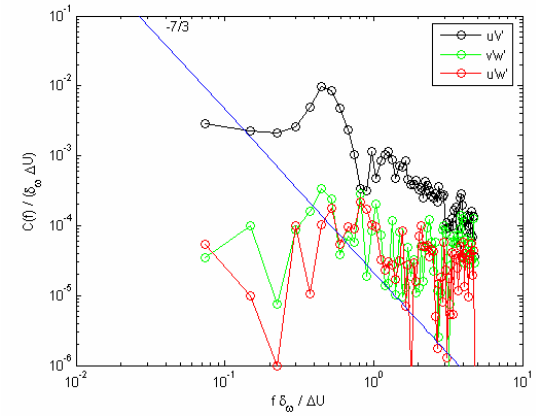

(e): $z / \delta_\omega = -0.031$

Figure 4.10: Normalized cospectra, $x/\theta_i = 210$, $y/\delta_\omega = 0.75$

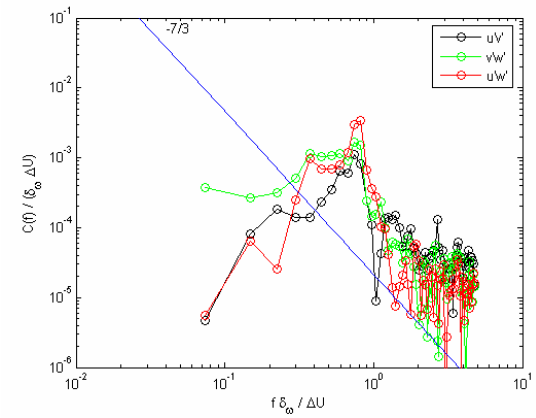

(a): $z/\delta_\omega = -2.0$

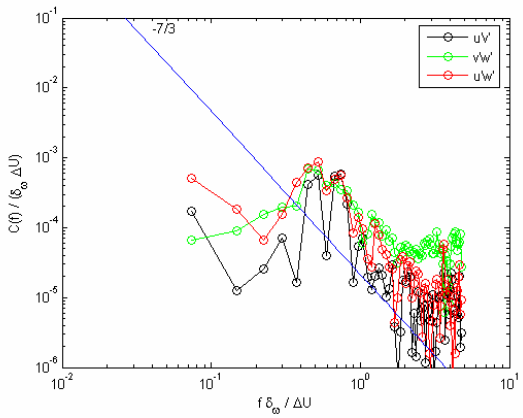

(b): $z/\delta_\omega = -0.25$

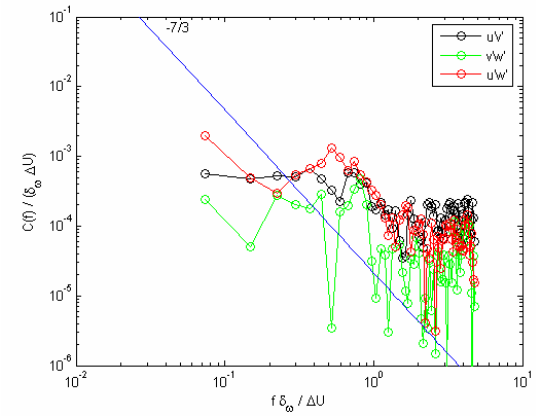

(c): $z/\delta_\omega = -0.12$

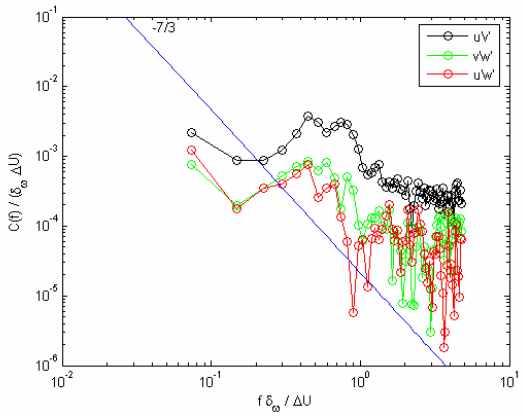

(d): $z/\delta_\omega = -0.062$

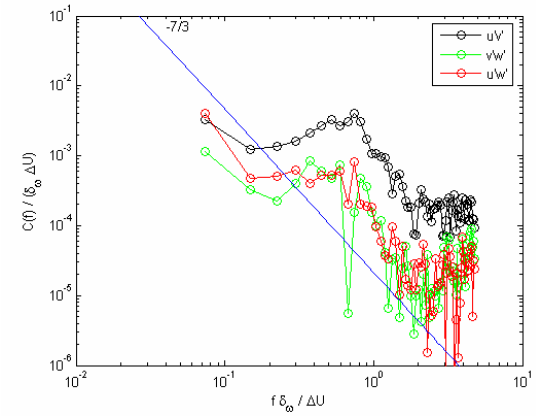

(e): $z/\delta_\omega = -0.031$

Figure 4.11: Normalized cospectra, x/θ_i = 210, y/δ_ω = -0.75

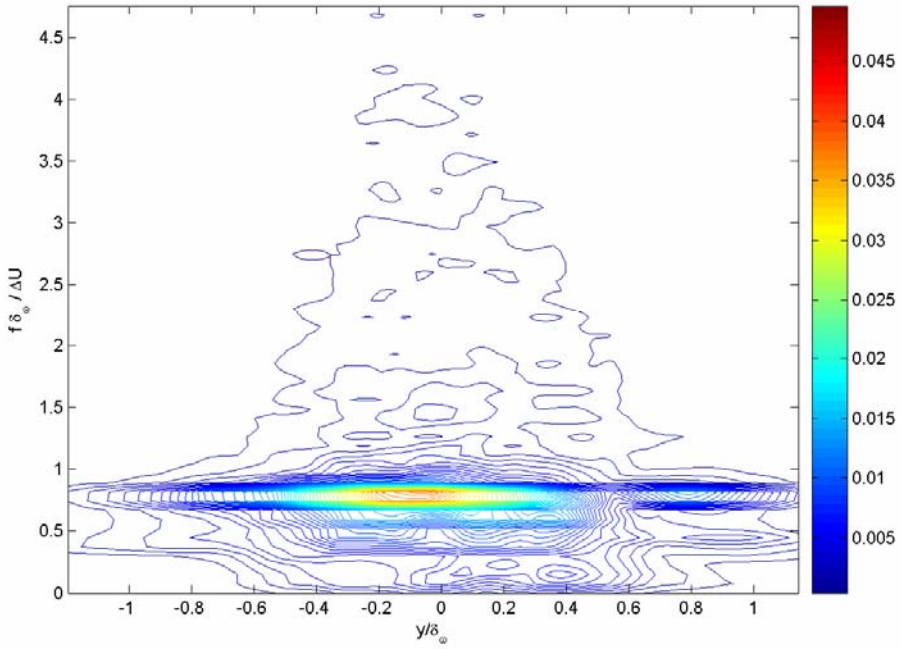

4.12(a): Cospectrum $C_{u'v'}(f)/(\delta_\omega \cdot \Delta U)$

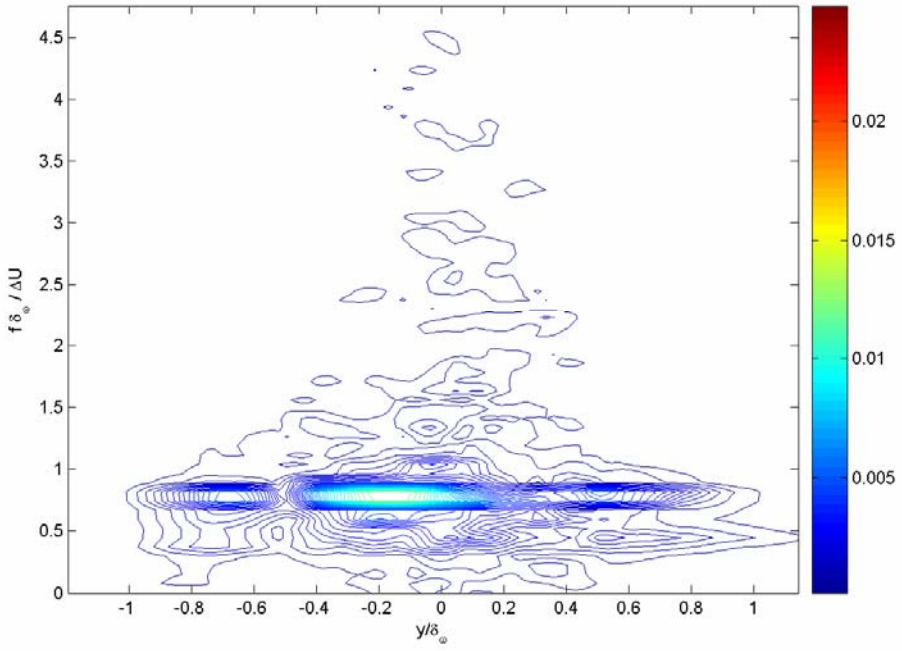

4.12(b): Cospectrum $C_{v'w'}(f)/(\delta_\omega \cdot \Delta U)$

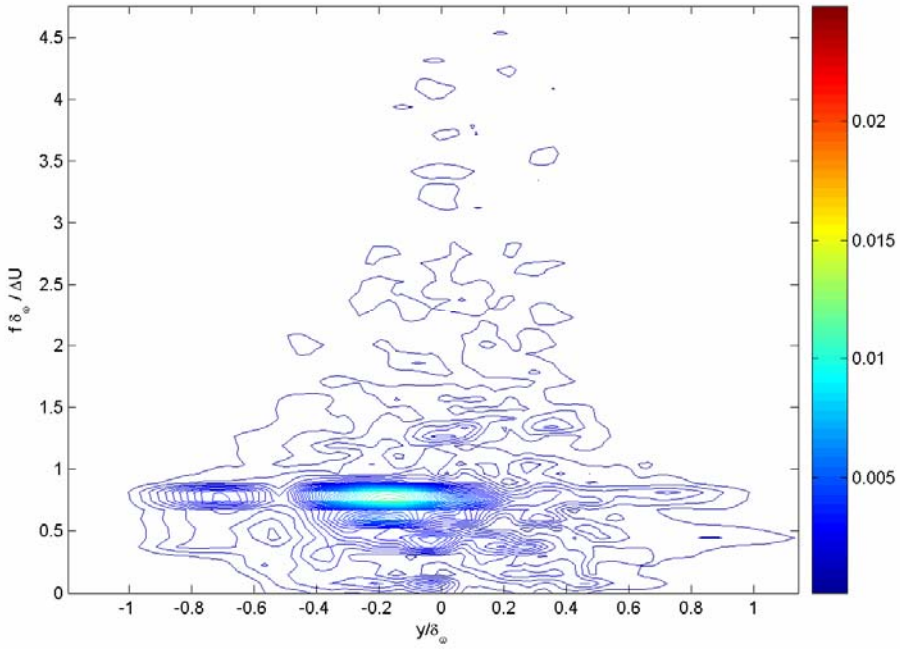

4.12(c): Cospectrum $C_{u'w'}(f)/(\delta_\omega \cdot \Delta U)$

Figure 4.12: Normalized cospectra, x/θ_i = 210, z/δ_ω = -2.0

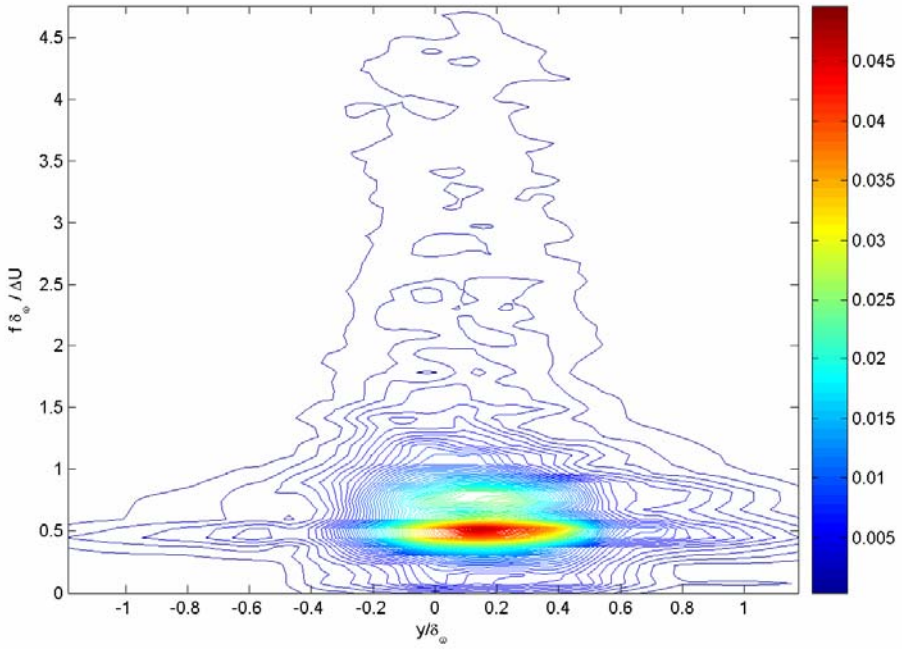

4.13(a): Cospectrum $C_{u'v'}(f)/(\delta_\omega \cdot \Delta U)$

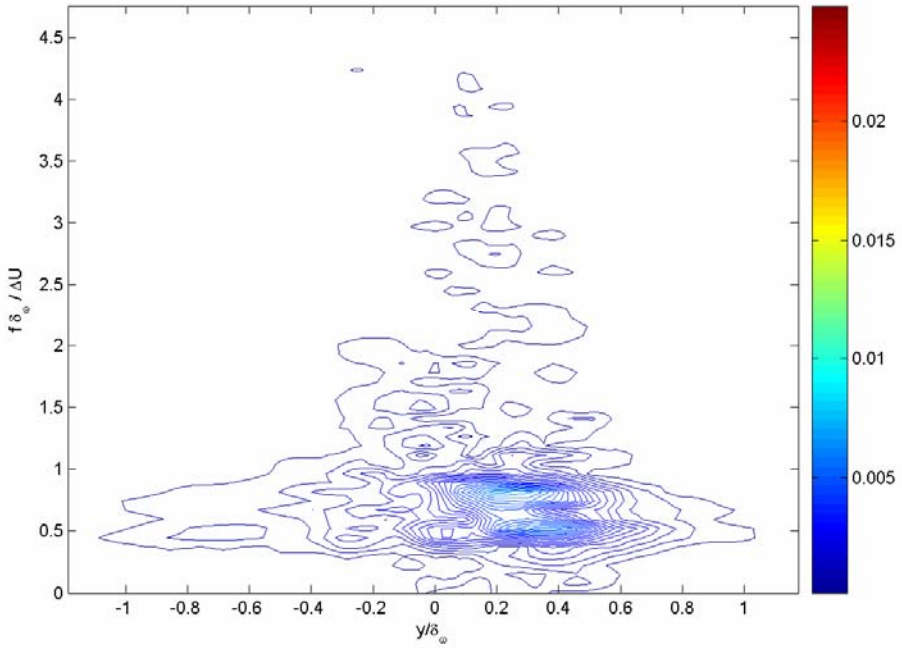

4.13(b): Cospectrum $C_{v'w'}(f)/(\delta_\omega \cdot \Delta U)$

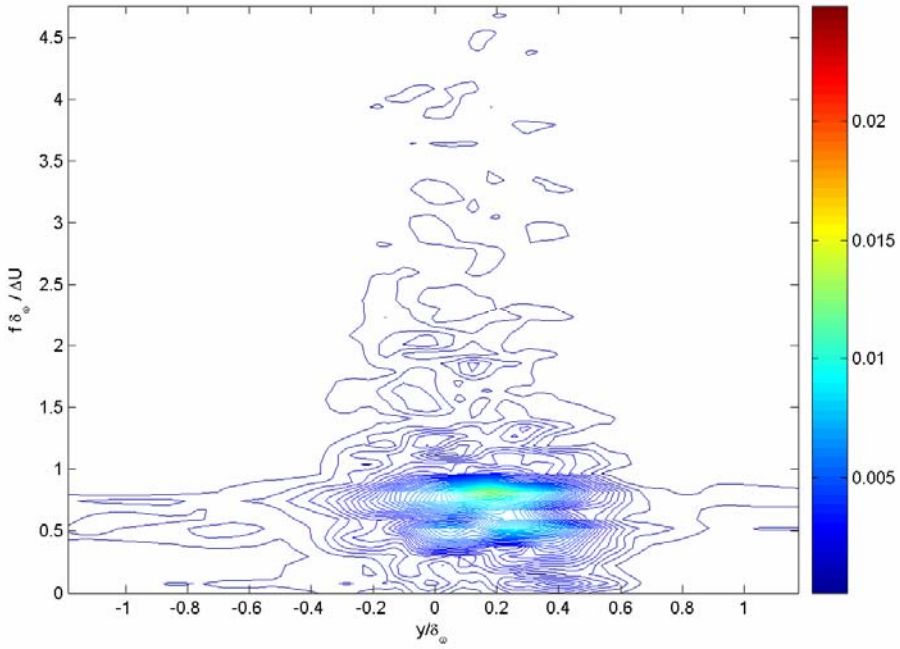

4.13(c): Cospectrum $C_{u'w'}(f)/(\delta_\omega \cdot \Delta U)$

Figure 4.13: Normalized cospectra, x/θ_i = 210, z/δ_ω = -0.25

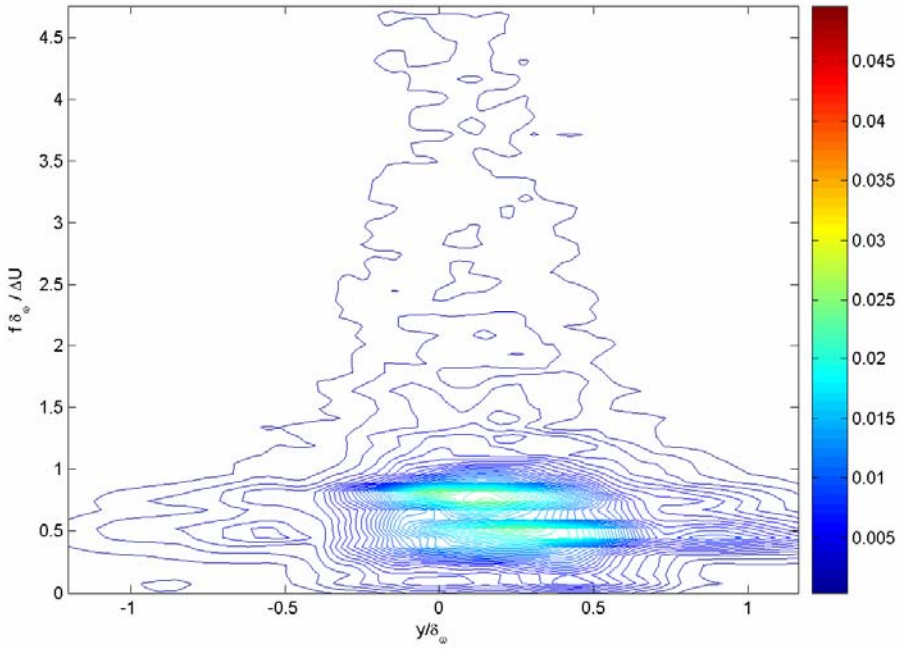

4.14(a): Cospectrum $C_{u'v'}(f)/(\delta_\omega \cdot \Delta U)$

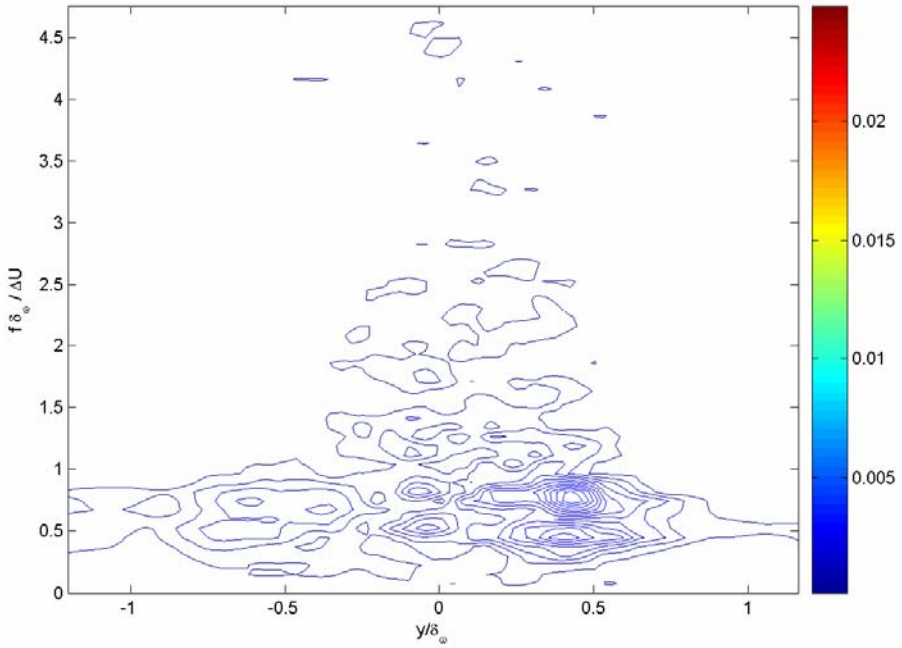

4.14(b): Cospectrum $C_{v'w'}(f)/(\delta_\omega \cdot \Delta U)$

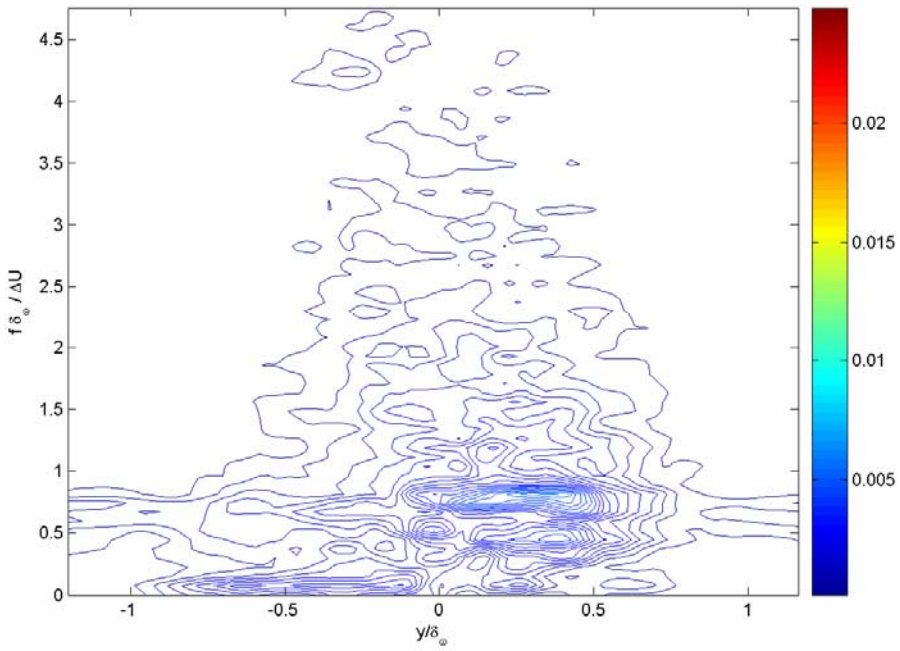

4.14(c): Cospectrum $C_{u'w'}(f)/(\delta_\omega \cdot \Delta U)$

Figure 4.14: Normalized cospectra, x/θ_i = 210, z/δ_ω = -0.12

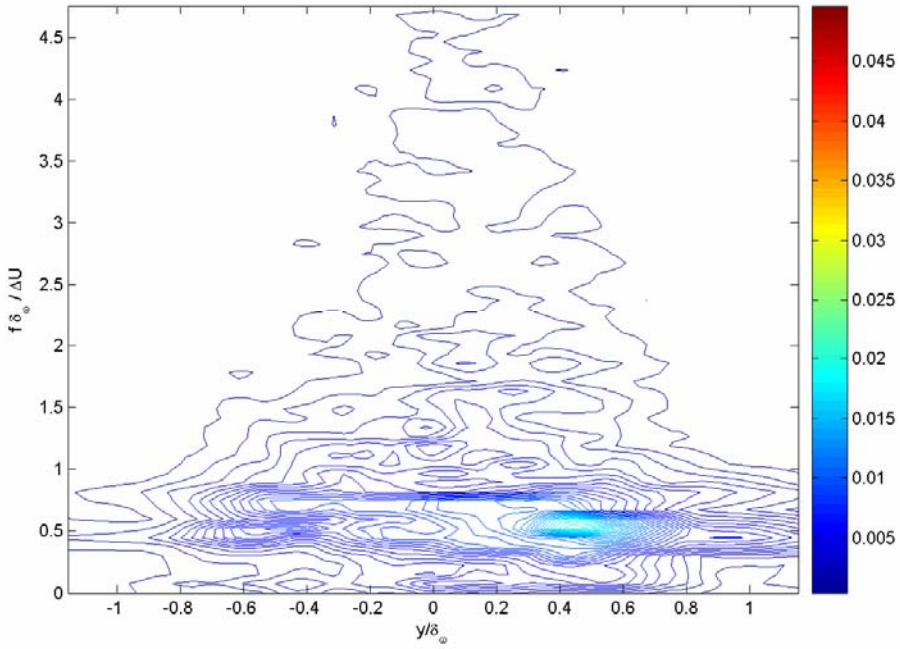

4.15(a): Cospectrum $C_{u'v'}(f)/(\delta_\omega \cdot \Delta U)$

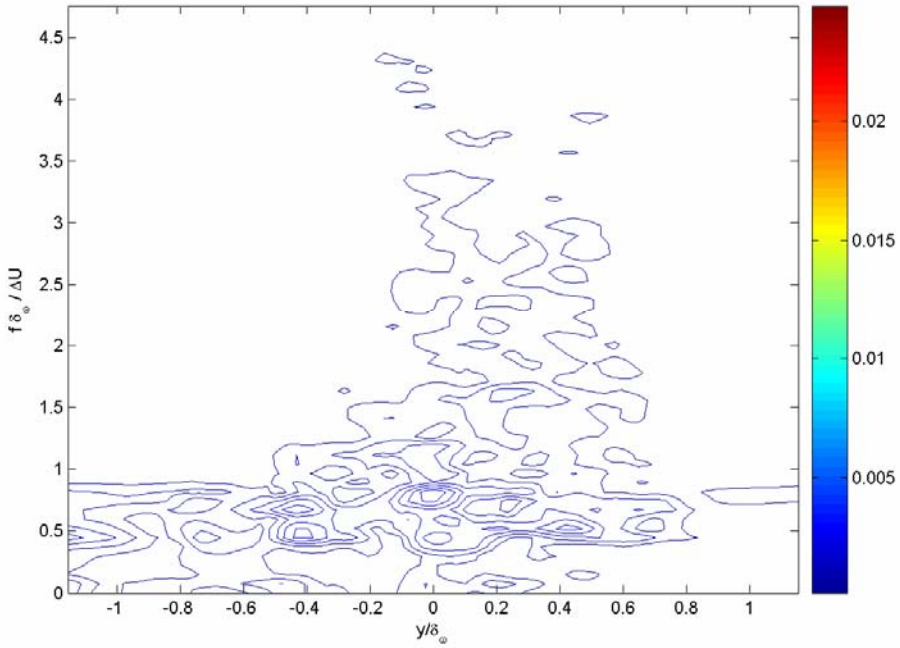

4.15(b): Cospectrum $C_{v'w'}(f)/(\delta_\omega \cdot \Delta U)$

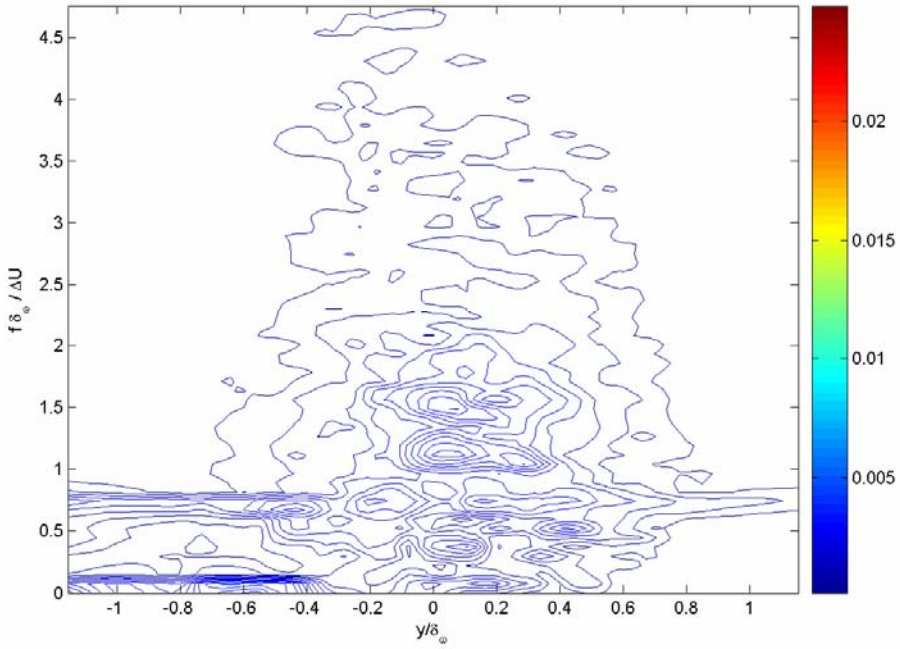

4.15(c): Cospectrum $C_{u'w'}(f)/(\delta_\omega \cdot \Delta U)$

Figure 4.15: Normalized cospectra, x/θ_i = 210, z/δ_ω = -0.062

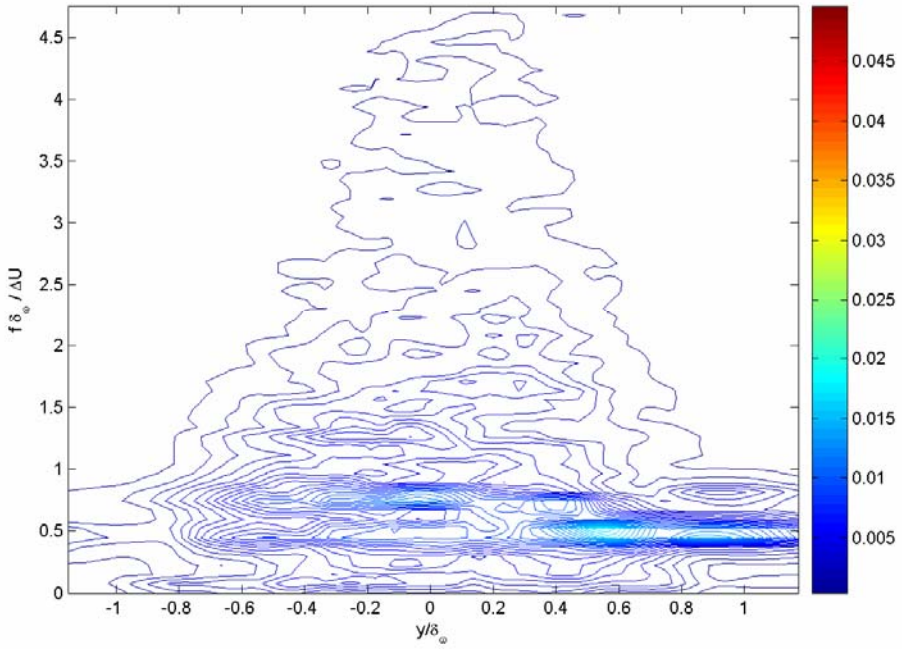

4.16(a): Cospectrum $C_{u'v'}(f)/(\delta_\omega \cdot \Delta U)$

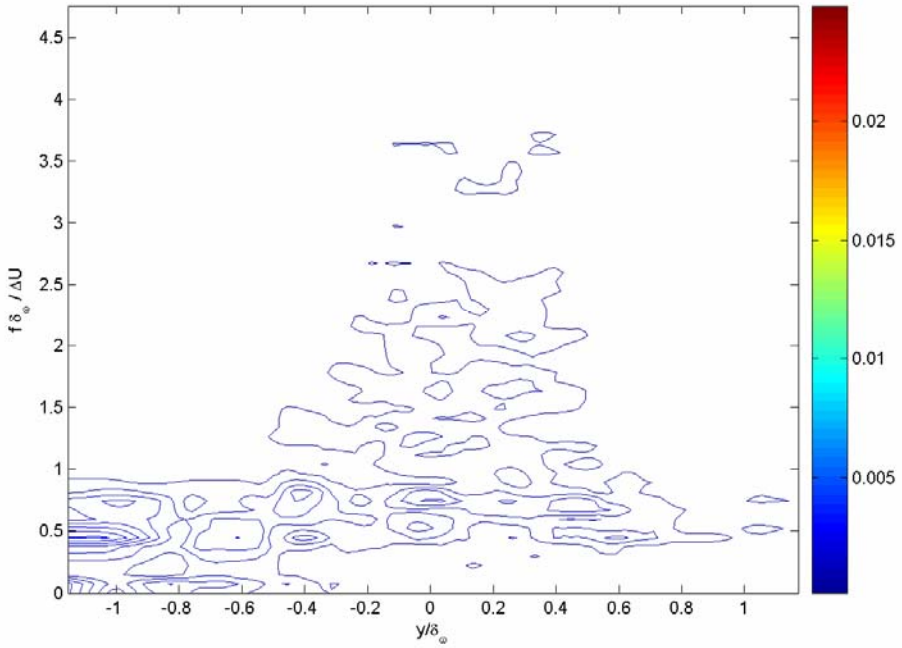

4.16(b): Cospectrum $C_{v'w'}(f)/(\delta_\omega \cdot \Delta U)$

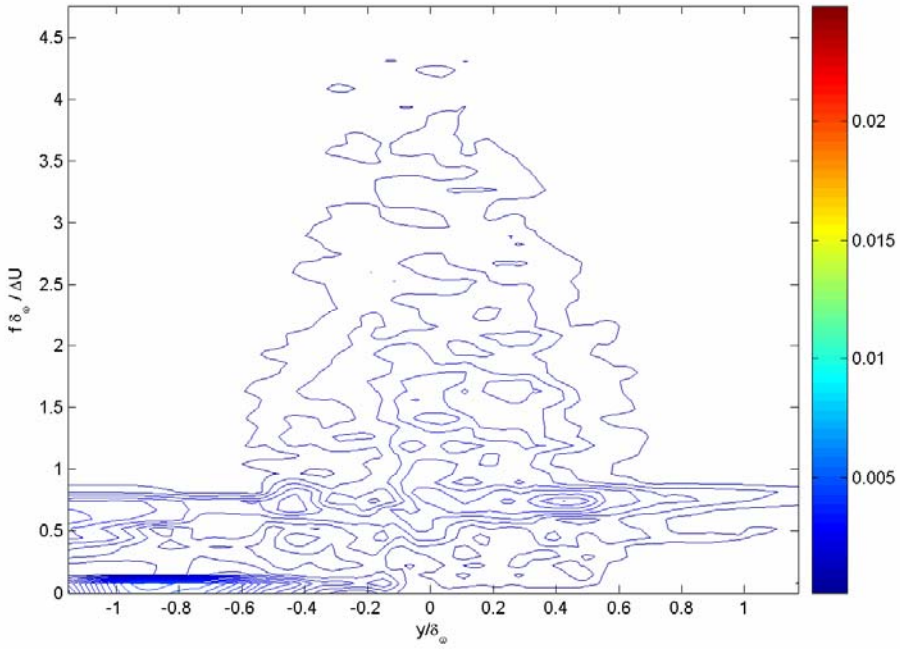

4.16(c): Cospectrum $C_{u'w'}(f)/(\delta_\omega \cdot \Delta U)$

Figure 4.16: Normalized cospectra, x/θ_i = 210, z/δ_ω = -0.031

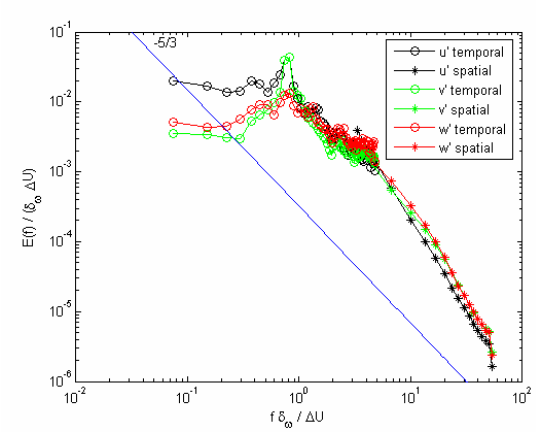

(a): $z / \delta_\omega = -2.0$

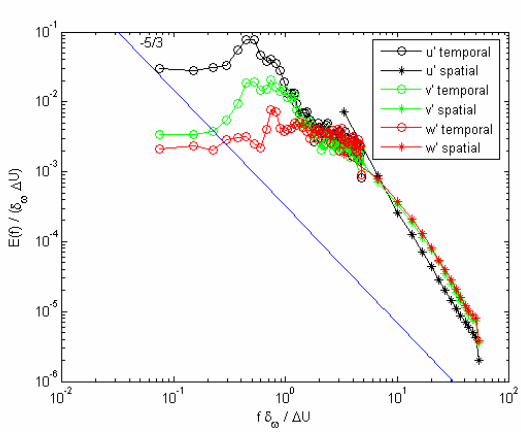

(b): $z / \delta_\omega = -0.25$

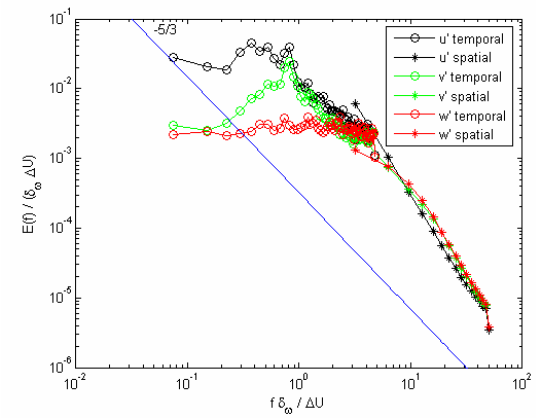

(c): $z / \delta_\omega = -0.12$

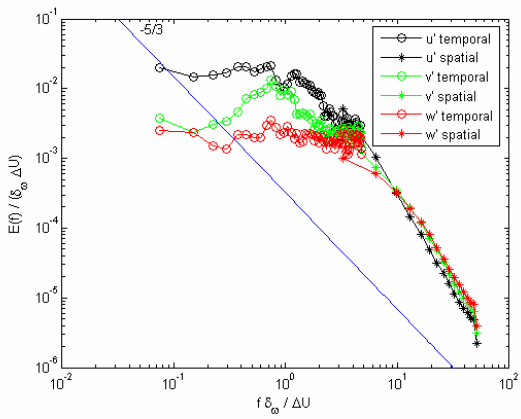

(d): $z / \delta_\omega = -0.062$

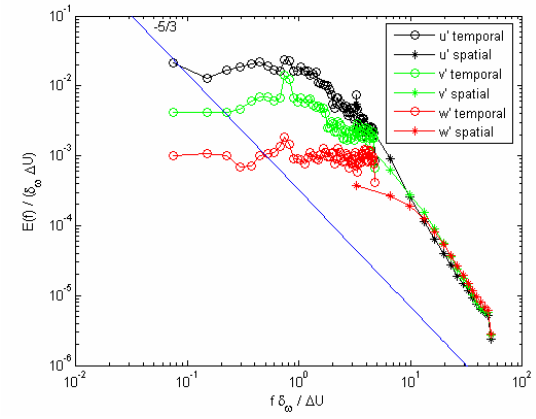

(e): $z / \delta_\omega = -0.031$

Figure 4.17: Normalized one-component power spectra, temporal and spatial, $x/\theta_i = 210$, $y/\delta_\omega = 0$

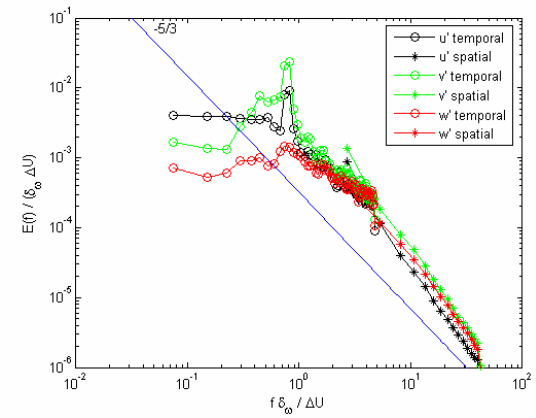

(a): $z / \delta_\omega = -2.0$

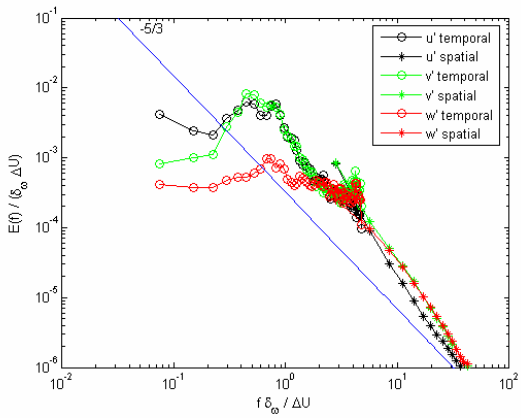

(b): $z / \delta_\omega = -0.25$

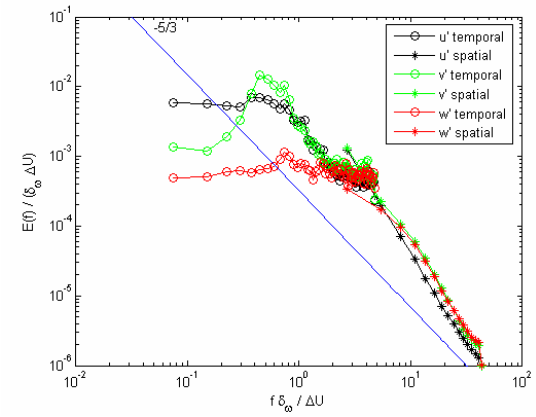

(c): $z / \delta_\omega = -0.12$

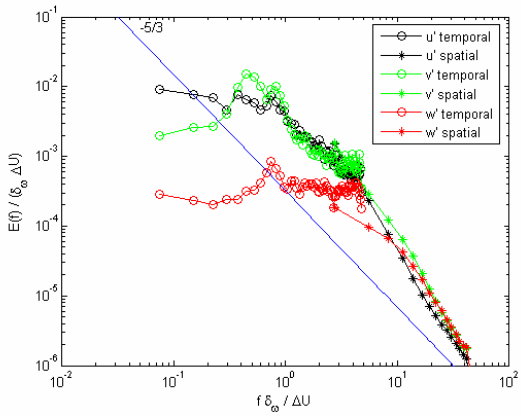

(d): $z / \delta_\omega = -0.062$

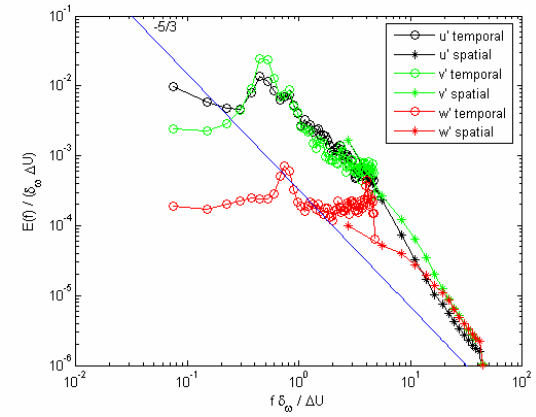

(e): $z / \delta_\omega = -0.031$

Figure 4.18: Normalized one-component power spectra, temporal and spatial, $x/\theta_i = 210$, $y/\delta_\omega = 0.75$

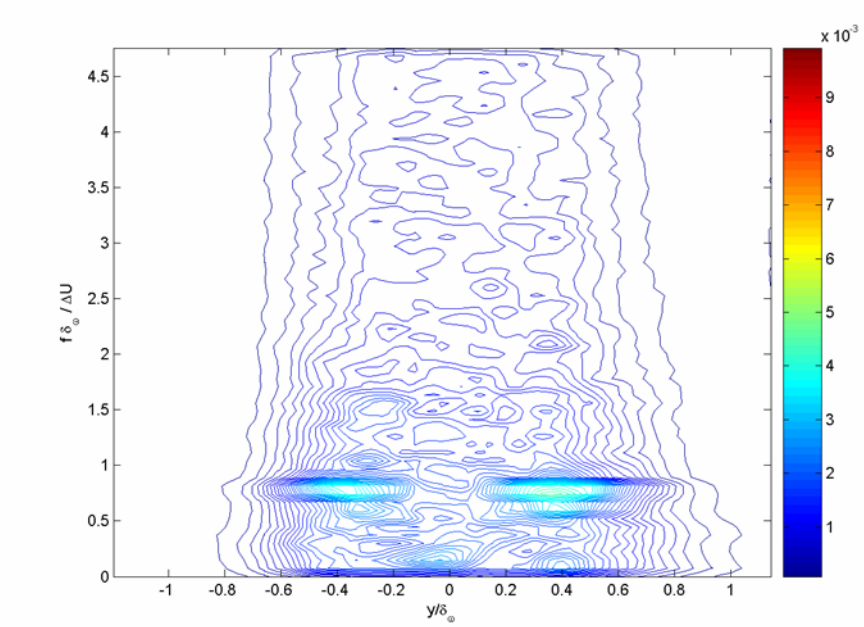

4.19(a): Energy spectrum $E_{tot}(f)/(\delta_\omega \cdot \Delta U)$, $z/\delta_\omega = -2.0$

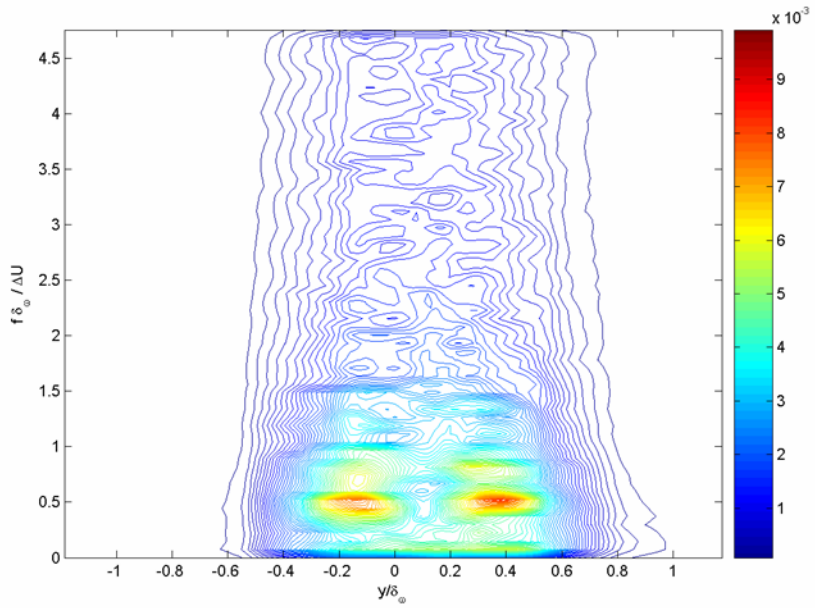

4.19(b): Energy spectrum $E_{tot}(f)/(\delta_\omega \cdot \Delta U)$, $z/\delta_\omega = -0.25$

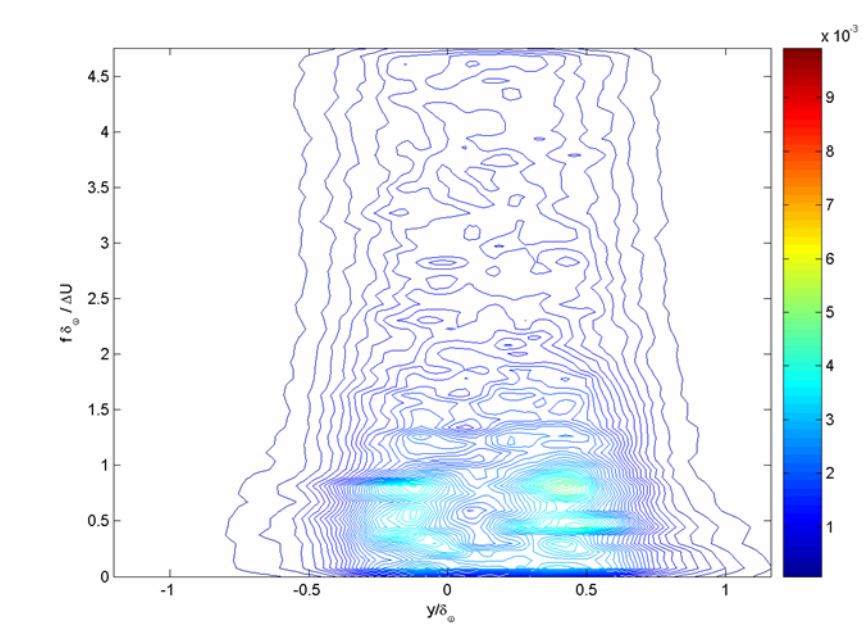

4.19(c): Energy spectrum $E_{tot}(f)/(\delta_\omega \cdot \Delta U)$, $z/\delta_\omega = -0.12$

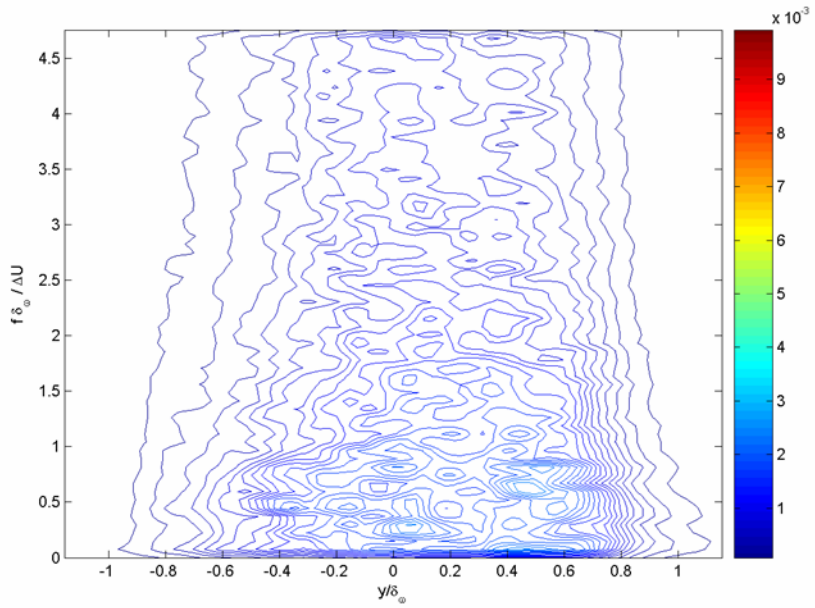

4.19(d): Energy spectrum $E_{tot}(f)/(\delta_\omega \cdot \Delta U)$, $z/\delta_\omega = -0.062$

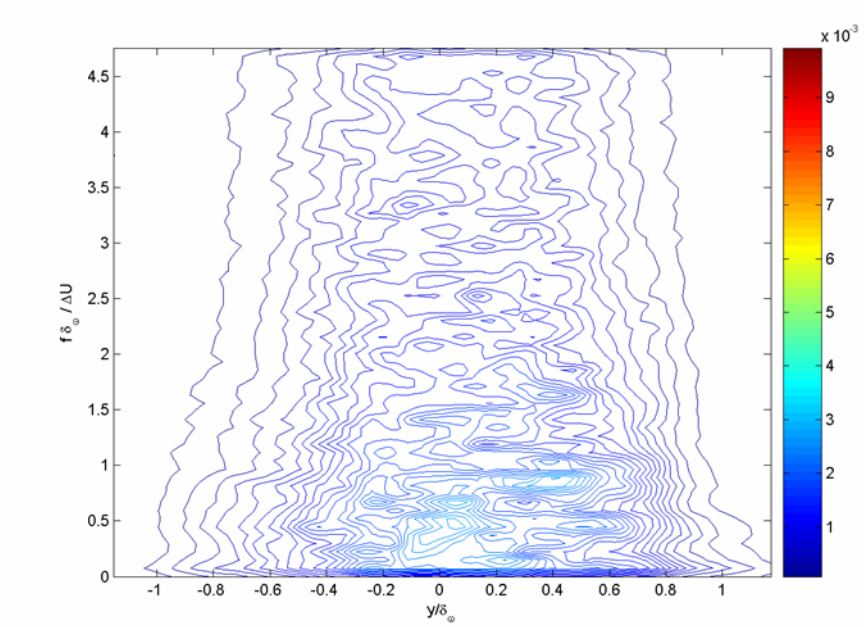

4.19(e): Energy spectrum $E_{tot}(f)/(\delta_\omega \cdot \Delta U)$, $z/\delta_\omega = -0.031$

Figure 4.19: Normalized three-component energy spectra, $x/\theta_i = 210$

Chapter 5 Conclusions

The dynamics of free surface turbulence at low Froude numbers has been investigated through experiments involving a turbulent mixing layer downstream of a free-surface-piercing splitter plate. It had been shown previously by Maheo that the vertical extent of the facility was sufficient to produce a very nearly two-dimensional mixing layer some distance from the free surface. Measurements were performed at this greater depth ("bulk flow") as a basis for comparison to the near-surface regions.

The width of the mixing layer, defined as the *local* vorticity thickness at a given depth, was found to decrease from its deep value by at least 25% as the free surface is approached, before reaching a minimum and then increasing beyond its deep value in the very immediate vicinity of the surface (depths of less than 10% of the bulk vorticity thickness). The depth at which the minimum width occurs, 25% of the bulk vorticity thickness ($z/\delta_\omega = -0.25$), corresponds approximately to that at which Maheo observed the cores of two streamwise counter-rotating vortices in the same flow.

The intensity of vertical velocity fluctuations was seen to monotonically decrease as the free surface is approached from below, while the transverse velocity fluctuations were seen to vary only slightly with depth. The profile across the mixing layer of the streamwise velocity fluctuations was shown to vary strongly with depth, having a maximum peak value at $z/\delta_\omega = -0.25$. As the surface is approached from this point, the peak value of this quantity was seen to decrease, yet still remain above the bulk level. Overall turbulence kinetic energy (all three components) was observed to behave in a very similar manner.

Spectral analysis of the velocity data obtained in the experiments described herein allowed more detailed understanding beyond that gained from Reynolds decomposition, as the large-scale oscillations could be separated from the upper reaches of the inertial range. Specifically, a significant deviation from the isotropic turbulence observed in the bulk is seen as the free surface is approached, as the vertical component suffers considerable attenuation. Near-surface anisotropy as evidenced by the cospectra of the various velocity components is considerably less pronounced.

The lower frequencies of velocity fluctuation, corresponding to the large scale turbulent structures rather than dissipation, were also available for analysis. A dominant frequency corresponding to the instability of a planar mixing layer was observed in varying intensities at all depths. However, very intense streamwise fluctuations at a lower, unrelated frequency, were observed at $z/\delta_\omega = -0.25$ in a narrow spanwise region near the center of the mixing layer. Unseen in the bulk flow at all, this fluctuations at this frequency appear in all components throughout the near surface region. They also appear in a very similar fashion in the presented cospectra, particularly in the cospectrum of the streamwise and spanwise velocity components. These spectral peaks and the manner in which they relate to one another are argued to be consistent with a long-wavelength lateral oscillation in the mean flow pattern, which takes place only near the free surface and in fact varies in amplitude quite strongly with depth in the surface layer.

It is observed that two long parallel vortices have been shown to be unstable at certain wavelengths depending on their diameters and separation distance. While a simple analysis based on the vortices identified by Maheo yields a most unstable wavelength of some three times the length of that which is observed in the present data, it

is pointed out that the distance between the vortices as the mixing layer develops in the streamwise direction in not constant, and that the wavelength predicted by the analysis is some 65 percent of the total downstream distance.

Strong parallels are seen with towed model boat wakes, specifically approximate agreement in the wavelength of the oscillation. However, important differences are noted regarding depth of maximum oscillation amplitude. In particular, the oscillating behavior of the flow examined in this thesis displays a maximum amplitude at the depth of the mean streamwise vortical structures, and in fact attenuates significantly as the surface is approached from below.

This intriguing aspect of the plane mixing layer interacting with a free surface certainly merits further examination, and the most promising starting point would be a spectral analysis along the entire length of the mixing layer through its development.

Appendix A – Data Convergence

Having obtained 3,000 instantaneous velocity fields at all locations examined with SDPIV, it is possible to investigate the rapidity with which the various Reynolds decomposition quantities converge to their stationary values. In this chapter the convergence histories of mean and fluctuating quantities will be presented.

As one application of such information is in determining how many SDPIV fields are required to obtain satisfactory convergence in similar studies. As a practical matter, such knowledge allows an investigator to estimate how many images must be recorded – and to address consequential issues such as data storage space, laboratory time, and processing time.

Convergence histories of mean quantities are quite straightforward. Fluctuating quantities, on the other hand, require some care in definition. We may consider for the sake of this discussion the single velocity component $u(t)$ at some arbitrary location $\mathbf{x}$. As described previously we will consider the Reynolds decomposition $u(t) = U + u'(t)$. It is assumed (as is the case for a spatially developing mixing layer) that the flow is stationary, and that the mean value *U* does not change with time.

If one has available a continuous signal $u(t)$ for $0 \le t \le T$ then the definitions of the two components of the Reynolds decomposition are clearly:

$$U = \frac{1}{T}\int_0^T u(t)dt;$$
$$u'(t) = u(t) - U.$$

If *u* is indeed stationary, then for sufficiently large *T* the mean value *U* will converge to a constant value. However, some variation is expected for smaller values of

T: $U = U(T)$. It can be seen then that the fluctuating value is also a function of the record length: $u' = u'(t,T)$. Statistical quantities based on the history of this fluctuation (*e.g.*, RMS values of the fluctuation intensity) will in turn be dependent on T – although this dependence will vanish for sufficiently large T.

As the usual definition for RMS fluctuation is:

$$u_{RMS}(T) = \sqrt{\overline{u'^2}} = \sqrt{\frac{1}{T}\int_0^T \left[u(t) - U(T)\right]^2 dt}\ .$$

The item of note in the above relation is that, when evaluating $u_{RMS}(T)$ it is necessary to use the mean value corresponding to that same value of T.

As the primary purpose of calculating such quantities as these for arbitrary record lengths is confirmation of adequate statistical convergence of experimental data, it would not be at all proper to use instead a "long-time" value of U. Doing such would be making use of information which would not be available had a record of duration T been all that was available. In all cases presented below, care has been taken to avoid this potential pitfall.

In actuality, rather than having at our disposal a continuous time history we have discrete uniformly sampled instantaneous values of u. Presented in this section are representative examples of the data convergence as the number of image pairs processed increases. All data displayed is was taken at a depth of $z = -164$ mm, a downstream distance of $x = 1000$ mm, and along the tunnel centerline.

Figures A.1(a-b) present, in real coordinates, the convergence history of all three mean velocity components. It is clear in these instances that oscillation of the figure has essentially halted by the time 1,500 image pairs have been considered.

Figure A.2 displays the convergence histories of all three velocity fluctuations ($\sqrt{\overline{u'^2}}$, $\sqrt{\overline{v'^2}}$, and $\sqrt{\overline{w'^2}}$). We can clearly observe that noticeable oscillations in these figures have stopped by 2,000 pairs.

Figures A.3(a-b) show the three cross-terms of the Reynolds stress tensor ($\overline{u'v'}$, $\overline{v'w'}$, and $\overline{u'w'}$). There is considerably more variation in all three of these quantities than is seen in either of the others presented, but the wildest of the fluctuations have ceased by 3,000 image pairs. Due to the dramatically different magnitudes of the final values, the percentage fluctuation varies. However, by the end of the available data records the values have all converged to within a range of +/- 5 mm^2/s^2.

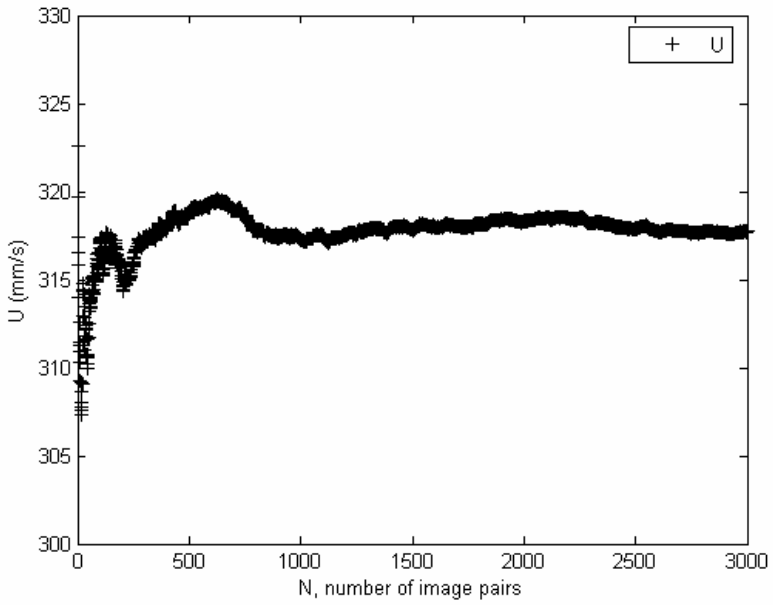

(a): Streamwise component

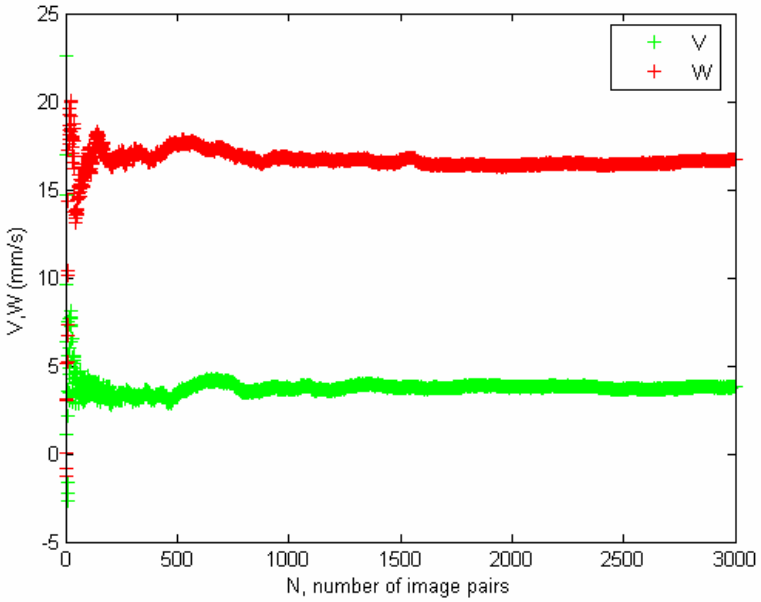

(b): Spanwise and vertical components

Figure A.1: Convergence histories of mean velocity components at z = -164 mm, x = 1000 mm

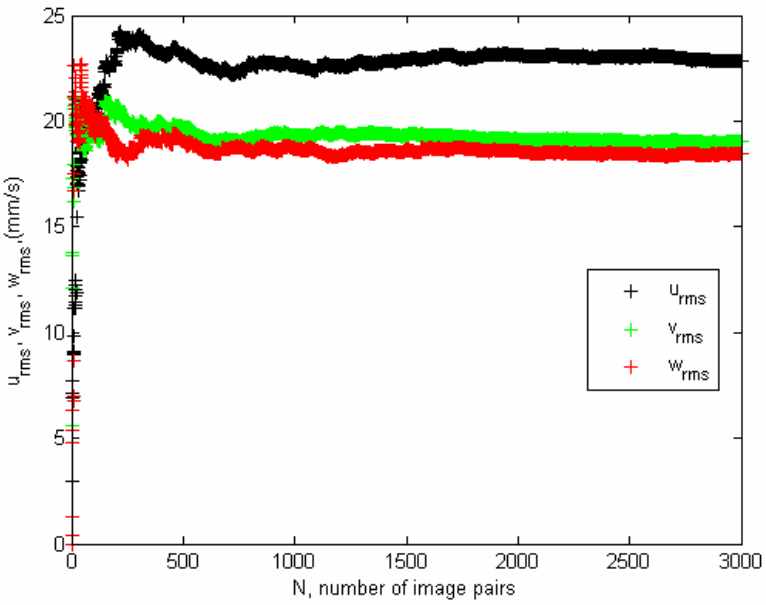

Figure A.2: Convergence histories of fluctuating velocity components at z = -164 mm, x = 1000 mm

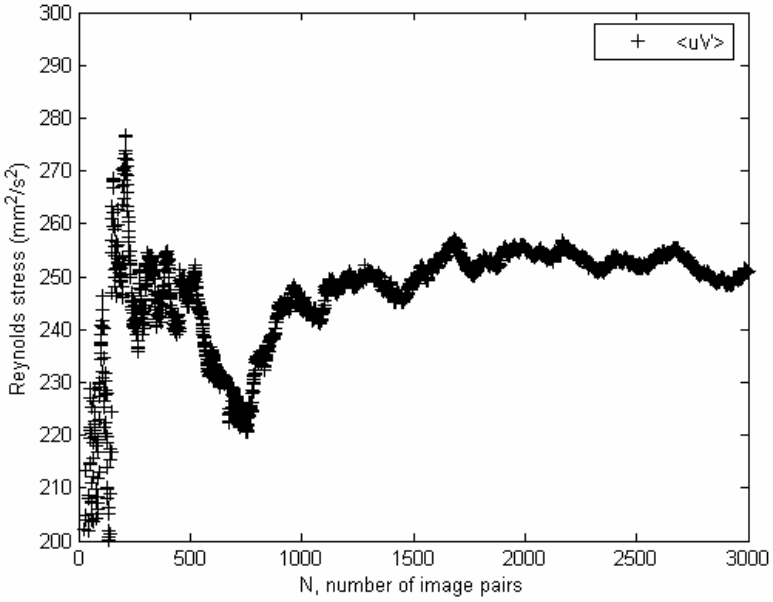

(a)

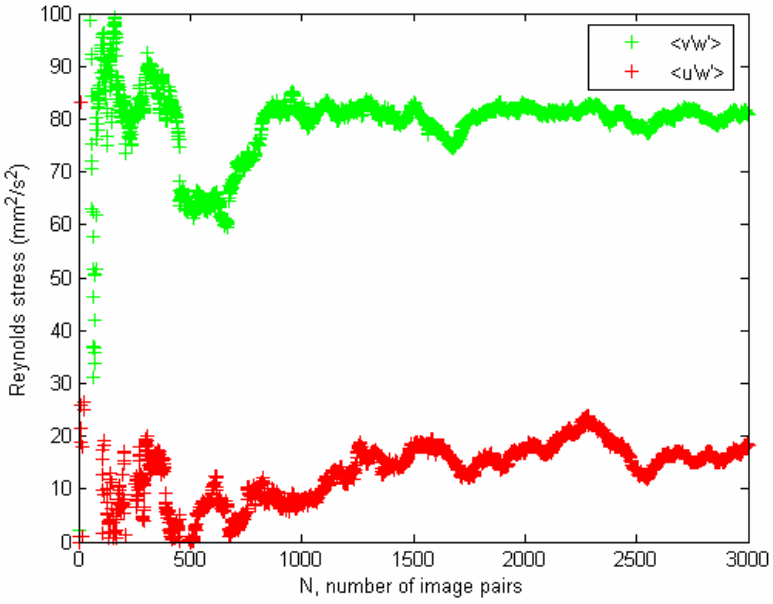

(b)

Figure A.3: Convergence histories of cross terms of Reynolds stress tensor, z = -164 mm, x = 1000 mm

Appendix B – Surface Waves

In the course of the data analysis the presence of what appears to be a standing wave very near the surface on the high speed side of the tunnel became known. Too small to have been observed visually, the effect on the mean vertical velocity component was quite obvious. The chief manifestation of this apparent wave is a strong *streamwise* variation in several properties over a given measurement domain; the fact that the measurement planes were parallel to the free surface proved quite convenient for the purposes of this observation. These streamwise variations were only visible at the two measurement depths closest to the surface – in real coordinates, 2.5 mm and 5.0 mm beneath the free surface.

The most strongly affected quantity was the vertical mean velocity *W*, which near the surface on the high-speed side of the tunnel exhibited strong streamwise variation. Figures B.1(a-c) show surface plots of the three mean velocity components over the entire SDPIV domain for a particular run taken at a depth of 2.5 mm beneath the surface. The colorbar ranges are identical to those on the corresponding plots in Chapter 3. The strongest variation is seen in *W*, but some is also observed in *U* and *V*. This particular location was among the most affected, and the cause is supposed to be a standing wave of relatively low amplitude on the surface of the water.

The various components for each case displayed in Chapter 3 were each examined on a run-by-run basis, and those components which showed strong streamwise variations were removed from the presented data. Such removals were confined to the high-speed side of the tunnel, and at the two most shallow interrogation depths. In most cases, the

fluctuating values and the surface-normal vorticity values exhibited no such trouble, and thus were included in the presented data.

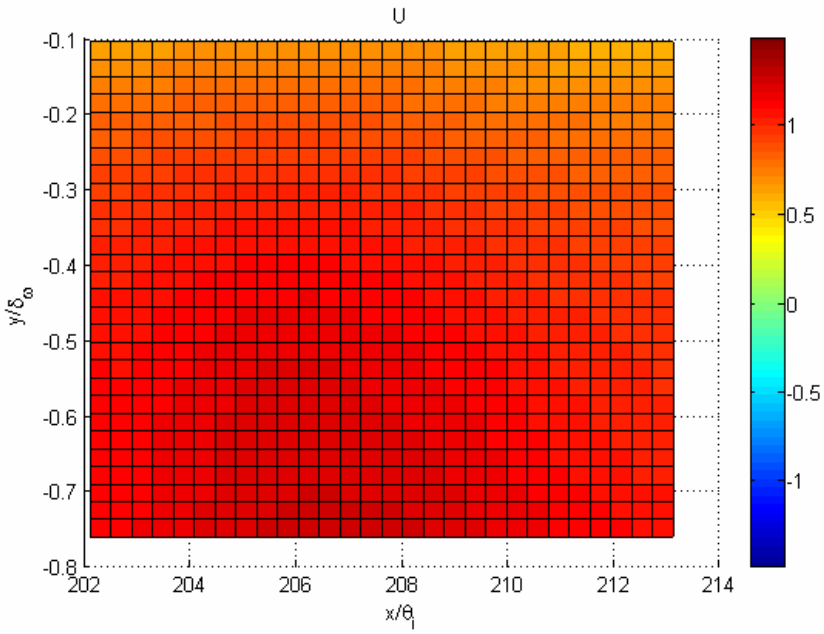

Figure B.1(a): Mean streamwise velocity field

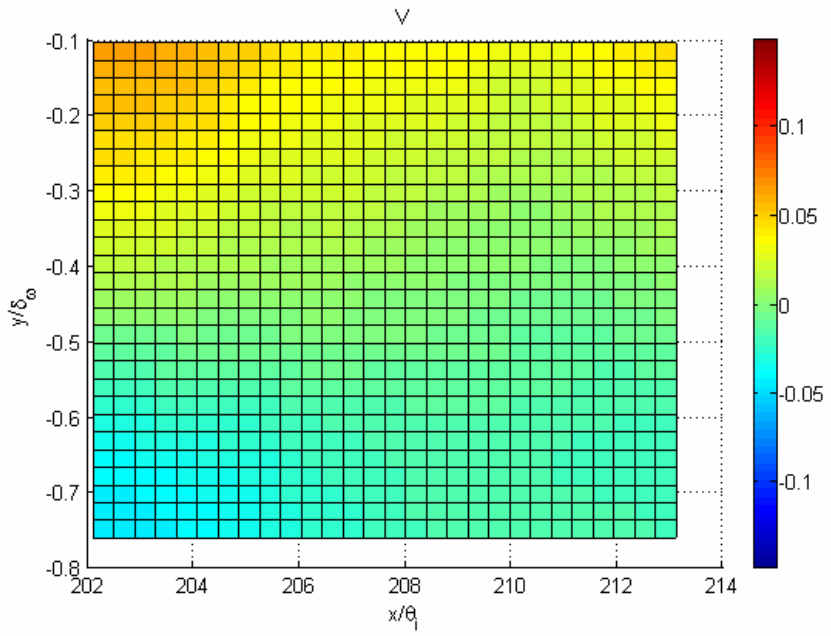

(b): Mean spanwise velocity field

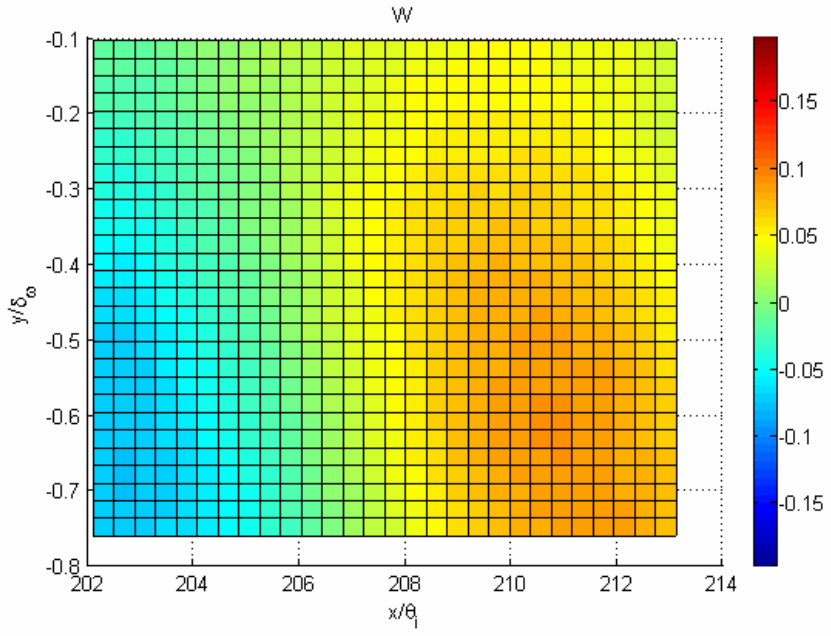

(c): Mean vertical wise velocity field

Figure B.1: Mean velocity component fields at z/δ_ω = -0.031, highlighting surface wave features

Appendix C – Spectral Math

Given the importance placed on the spectral results presented in this thesis, it is important that the precise steps taken to achieve them be made clear. In the literature there are a number of different methods, for example, of normalizing discrete Fourier transforms and power spectra. It is also critical that the exact steps in calculating the presented cospectra be detailed exactly.

At each location interrogated by SDPIV, a time history of all three velocity components was obtained. The sampling rate of this time history is $\Delta t = 1/15\,\mathrm{s}$; the record length is $N = 3000$ data points for a total recording time of 200 seconds. At any given spatial coordinate $\mathbf{x} = (x, y, z)$ we thus have velocity data $\mathbf{u}(\mathbf{x}, t) = (u, v, w)$. Each of those three components is itself a function of both position and time. At any fixed spatial coordinate, the sampled record of each component at our disposal (the streamwise component, *u*, for example) may be expressed as:

$$u_k(\mathbf{x}) = u(\mathbf{x}, t_k);$$
$$t_k = k \cdot \Delta t \text{ for } k = 0, \ldots, N-1.$$

We thus perform our temporal spectral analyses locally using the three data records $u_k(\mathbf{x})$, $v_k(\mathbf{x})$, and $w_k(\mathbf{x})$.

The power spectral densities of individual components (*e.g.*, *u*) are estimated using Welch's averaged periodogram method as implemented by the MATLAB programming environment in its native routine *pwelch*. The 3,000 element long time history (with the local mean velocity subtracted out) was broken into segments 128 elements in length; consecutive segments overlapped by 64 elements (50%). Each segment was treated using a Hamming window of width equal to the segment length

before the power spectral density calculation was made. After this was done for each segment, the results were averaged to produce a final result.

To express this more mathematically, let *M* be the length of each segment in the Welch periodogram estimation (*M* = 128 for these cases, as indicated above). The resulting one-sided power spectral density (for, for example, *u*) would be noted as $S_{uu,q}(f_q)$ for $q = 0,...,M/2$, and $f_q = q/(M \cdot \Delta t)$.

There are a number of popular choices for normalization of power spectral density results, and for many purposes the distinction is unimportant because a scaling factor will not change the features being studied. In the results presented herein, the normalization chosen was such that the discrete integral of the power spectral density function is equal to the mean power of the signal:

$$\sum_{q=0}^{M/2} S_{uu,q} \cdot \Delta f = \frac{1}{M} \sum_{k=0}^{M-1} u_k u_k .$$

The cospectra presented are achieved in a similar manner, using another native MATLAB routine – *cpsd*. This routine computes the one-sided cross spectral density function between two arbitrary velocity signals, which in general is complex. The real part of this function, referred to as the cospectrum, is presented within this work.

The normalization of the cospectrum results is done in the same spirit as that for the power spectra. Let $C_{uv,q}(f_q) = \mathrm{Re}\left[S_{uv,q}(f_q)\right]$ for $q = 0,...,M/2$, and $f_q = q/(M \cdot \Delta t)$. Then the normalization of the signal is such that:

$$\sum_{q=0}^{M/2} C_{uv,q} \cdot \Delta f = \frac{1}{M} \sum_{k=0}^{M-1} u_k v_k .$$

The combined temporal and spectral data presented in Chapter 4 was obtained through the application of the Taylor hypothesis to effectively convert high-resolution spatially-varying velocity data into temporally-varying data. At each of the measurement stations interrogated during this experiment, 3,000 instantaneous three-component velocity fields were obtained; in all cases the velocity field data lies in a plane parallel to the free surface. The grid upon which this velocity field is defined is uniform, and is aligned with the *x* and *y* axes within the tunnel test section. The data for any one measurement station is all at a common depth z_0, and we may identify one y value within the field y_0. Consider any single field to have been obtained at arbitrary time t_0. We may then isolate a single line of data in the streamwise direction, containing *K* elements (depending on the details of the apparatus and processing parameters):

$$\begin{aligned} u_k &= u(x_k, y_0, z_0, t_0); \\ v_k &= v(x_k, y_0, z_0, t_0); \\ w_k &= w(x_k, y_0, z_0, t_0); \\ x_k &= k \cdot \Delta x \text{ for } k = 0, \ldots, K-1 \end{aligned}$$

The value of Δx varies slightly between measurement locations, and is a function of details of of the processing.

Already available, and presented in this thesis, are the known mean velocity component values for this location. (The total range of x_k is quite small, and all may be considered to be approximately at x_0 = 1000 mm.) We thus have at our disposal the mean velocity values

$$\begin{aligned} U &= U(x_0, y_0, z_0); \\ V &= V(x_0, y_0, z_0); \\ W &= W(x_0, y_0, z_0); \end{aligned}$$

We have also previously established that at all locations examined the streamwise component of the mean velocity is much larger than either of the remaining two: $U >> V; U >> W$.

We may thus make the assumption that the flow field will advect only the in x direction; this greatly simplifies our application of the Taylor hypothesis. Specifically, we perform the following operation on the u_k values (for example; other components are similar):

$$u_k = u(x_0, y_0, z_0, t_k);$$
$$t_k = -k \cdot \frac{\Delta x}{U(x_0, y_0, z_0)}.$$

We now have what we shall take to be a (short) time history of each component at a point within the flow field. Power spectra of u_k may be calculated in a manner very similar to that described above for the temporal velocity data. This short collection of u_k data is too short (~28 elements) to satisfactorily attempt a Welch-style approach as described previously, so no segmenting is performed. The collection of data from each velocity field is zero-padded to 32 elements in length and windowed with a Hamming window prior to a single periodogram estimation being obtained. This is done for all 3,000 velocity fields in a given measurement location, and these 3,000 periodograms are averaged to obtain the final estimate of the power spectral density.

The normalization of the PSD is exactly the same as that done for the temporal data as described above. This enables the two separately-computed power spectra (temporal and spatial) to be plotted next to one another and compared. No “correction factor” is necessary in an attempt to make the two plots agree in the region of overlap.

References

Adrian, R.J. 1991 Particle-imaging techniques for experimental fluid mechanics. *Ann Rev. Fluid Mech.* **23**, 261-304.

Anthony, D.G. & Willmarth, W.W. 1992 Interaction of a submerged jet with a free surface. *J. Fluid Mech.* **243**, 699-720.

Banerjee, S. 1994 Upwellings, downdrafts, and whirlpools: Dominant structures in free surface turbulence. *Appl. Mech. Rev.* **47**(6-2), 166-172.

Bernal, L.P. & Kwon, J.T. 1989 Vortex ring dynamics at a free surface. *Phys. Fluids A* **1**, 449-451.

Brown, G.L. & Roshko, A. 1974 On density effects and large structure in turbulent mixing layers. *J. Fluid Mech.* **64**(4), 775-816.

Brumley, B. & Jirka, H. 1987 Near-surface turbulence in a grid stirred tank. *J. Fluid Mech.* **183**, 235-263.

Dabiri, D. 2003 On the interaction of a vertical shear layer with a free surface. *J. Fluid Mech.* **480**, 217-232.

Dimotakis, P.E. 2000 The mixing transition in turbulent flows. *J. Fluid Mech.* **409**, 69-98.

Dimotakis, P.E. & Brown, G.L. 1976 The mixing layer at high Reynolds number: large-structure dynamics and entrainment. *J. Fluid Mech.* **78**(3), 535-560.

Dommermuth, D.G. 1992 The formation of U-shaped vortices on vortex tubes impinging on a wall with applications to free surfaces. *Phys. Fluids A* **4**, 757-769.

Elghobashi, S. 1994 On predicting particle-laden turbulent flows. *Appl. Sci. Res.* **52**, 309-329.

Hoekstra, M. 1991 Macro wake features of a range of ships. MARIN Rep. 410461-1-P. Maritime Research Institute Netherlands.

Hunt, J. & Graham, J. 1978 Free-stream turbulence near plate boundaries. *J. Fluid Mech.* **84**, 178-209.

Jeon, D. 2000 On cylinders undergoing one- and two- degree of freedom forced vibrations in a steady flow. *PhD Thesis*, California Institute of Technology.

Liepmann, D. 1990 The near-field dynamics and entrainment field of submerged and near-surface jets. *PhD Thesis*, University of California, San Diego.

Logory, L.M., Hirsa, A. & Anthony, D.G. 1996 Interaction of wake turbulence with a free surface. *Phys. Fluids* **8**(3), 805-815.

Maheo, P.M. 1998 Free-surface turbulent shear flows. *PhD Thesis*, California Institute of Technology.

Mangiavacci, N., Gundlapalli, R. & Akhavan, R. 1994 Dynamics of a turbulent jet interacting with a free surface. Free-surface turbulence ASME 1994, FED-**181**, 69-82.

Milgram, J.H. 1988 Theory of radar backscatter from short waves generated by ships, with application to radar (SAR) imagery. *J. Ship Res.* **32**, 54-69.

Munk, W.H., Scully-Power, P. & Zachariasen, F. 1987 Ships from space. *Proc R. Soc. Lond. A* **412**, 231-254.

Ochadlick, A.R. Jr., Cho, P. & Evans-Morgis, J. 1992 Synthetic aperture radar observations of currents collocated with slicks. *J. Geophys. Res.* **97**, 5325-5330.

Ohring, S. & Lugt, H.J. 1995 Interaction of a viscous vortex pair with a free surface. *J. Fluid Mech.* **227**, 47-70.

Ol, M.V. 2001 The passage toward stall of nonslender delta wings at low Reynolds number. *PhD Thesis*, California Institute of Technology.

Pan, Y. & Bannerjee, S. 1995 A numerical study of free-surface turbulence in channel flow. *Phys. Fluids* **7**(7), 1649-1664.

Park, H.G. 1998 A study of heat transport processes in the wake of a stationary and oscillating circular cylinder using digital particle image velocimetry/thermometry. *PhD Thesis*, California Institute of Technology.

Peltzer, R.D., Griffin, O.M., Barger, W.R. & Kaiser, J.A.C. 1992 High-resolution measurement of surface-active film redistribution in ship wakes. *J. Geophys. Res. C* **104**, 245-258.

Raffel, M., Willert, C.E. & Kompenhans, J. 1998 *Particle image velocimetry: a practical guide.* Springer, Berlin.

Reed, A.M., Beck, R.F., Griffin, O.M. & Peltzer, R.D. 1990 Hydrodynamics of remotely sensed surface-ship wakes. *Trans. Soc. Naval Archit. Mech. Engrs.* **98**, 319-363.

Sarpkaya, T. & Henderson, D.O. 1985 Free surface scars and striations due to trailing vortices generated by a submerged lifting surface. AIAA Paper 85-0445.

Sarpkaya, T. & Suthon, P. 1991 Interaction of a vortex couple with a free surface. *Exp. Fluids* **11**(4), 205-217.

Scully-Power, P. 1986 Navy oceanographer shuttle observations, Mission report, Rep. STSS 41-G, NUSC Tech. Doc. 7611, Nav. Underwater Syst. Cent., Newport, Rhode Island, 3-26-86.

Shemdin, O.H. 1987 SAR imaging of ship wakes in the Gulf of Alaska. Final Rep. N00014-84-WRM-2212, Office of Naval Research, Arlington, Virginia.

Shen, L., Zhang, X. & Yue, D.K.P. 2002 Free-surface turbulent wake behind towed ship models: experimental measurements, stability analyses and direct numerical simulations. *J. Fluid Mech.* **469**, 89-120.

Shen, L., Zhang, X., Yue, D.K.P. & Triantafyllou, G.S. 1999 The surface layer for free-surface turbulent flows. *J. Fluid Mech.* **386**, 167-212.

Saddoughi, S.G. & Veeravalli, S.V. 1994 Local isotropy in turbulent boundary-layers at high Reynolds-number. *J. Fluid Mech.* **268**, 333-372.

Swean, T.F. Jr., Ramberg, S.E. & Miner, E.W. 1991 Anisotropy in a turbulent jet near a free surface. *J. Fluid Eng.* **113**, 430-438.

Uijttewaal, W.S.J. & Booij, R. 2000 Effects of shallowness on the development of free-surface mixing layers. *Phys. Fluids* **12**(2), 392-402.

Uijttewaal, W.S.J. & Tukker, J. 1998 Development of quasi two-dimensional structures in a shallow free-surface mixing layer. *Exp. Fluids* **24**, 192-200.

Vesecky, J.F. & Stewart, R.H. 1982 The observation of ocean surface phenomena using imagery from the Seasat synthetic aperture radar: an assessment. *J. Geophys. Res.* **87**(C5), 3397-3430.

Walker, D.T. 1997 On the origin of the 'surface currents' in turbulent free-surface flows. *J. Fluid Mech.* **339**, 275-285.

Walker, D.T. & Johnson, V.G. 1991 Observations of turbulence near the free surface in the wake of a model ship. In *Dynamics of bubbles and vortices near a free surface* (ed. I. Sahin & G. Tryggvason), ASME AMD-**119**.

Walker, D.T., Leighton, R.I., & Garza-Rios, L.O. 1996 Shear-free turbulence near a flat free surface. *J. Fluid Mech.* **320**, 19-51.

Weigand, A. & Gharib, M. 1996 Experimental studies of vortex disconnection and connection at a free surface. *J. Fluid Mech.* **321**, 59-86.

Westerweel, J., Dabiri, D. & Gharib, M. 1997 The effect of a discrete window offset on the accuracy of cross-correlation analysis of digital PIV recordings. *Exp. Fluids* **23**, 20-28.

Westerweel, J., Flör, J.B. & Nieuwstadt. F.T.M. 1991 Measurement of dynamics of coherent flow structures using particle image velocimetry. *Appl. Laser Tech. Fluid Mech.* (eds. Adrian, R.J. *et al.*), Springer, Berlin, 476-499.

Widnall, S.E. 1975 Structure and dynamics of vortex filaments. *Ann. Rev. Fluid Mech.* **7**, 141-165.

Willert, C.E. 1992 The interaction of modulated vortex pairs with a free surface. *PhD Thesis*, University of California, San Diego.

Willert, C.E. & Gharib, M. 1991 Digital particle image velocimetry. *Exp. Fluids* **10**, 181-193.

Winant, C.D. & Browand, F.K. 1974 Vortex pairing: the mechanism of turbulent mixing-layer growth at moderate Reynolds number. *J. Fluid Mech.* **63**(2), 237-255.

Wyngaard, J.C. & Coté, O.R. 1972 Cospectral similarity in atmospheric surface-layer. *Quart. J. R. Met. Soc.* **98**, 590-603.

Zuhal, L.R. 2001 Formation and near-field dynamics in a wing tip vortex. *PhD Thesis*, California Institute of Technology.